DOI: 10.14750/ME.2021.051

UNIVERSITY OF MISKOLC
FACULTY OF MECHANICAL ENGINEERING AND INFORMATICS

HIGH ENERGY BEAM WELDING OF ADVANCED HIGH STRENGTH STEELS

PHD THESES

Submitted by

Raghawendra Pratap Singh Sisodia
Industrial & Production Engineering (BE),
Mechanical Engineering (Production) (ME),
Mechanical Engineering (CAD/CAM) (MSc)
International Welding Engineer/European Welding Engineer (IWE/EWE)

ISTVÁN SÁLYI DOCTORAL SCHOOL OF MECHANICAL ENGINEERING SCIENCES
TOPIC FIELD: ENGINEERING MATERIALS SCIENCE, PRODUCTION SYSTEMS AND PROCESSES
TOPIC GROUP: MATERIALS ENGINEERING AND MECHANICAL TECHNOLOGY

Head of the Doctoral School

Prof. Dr. Gabriella Bognár Vadászné
DSc, Full Professor

Head of Topic Group

Prof. Dr. Miklós Tisza
DSc, Professor Emeritus

Scientific Supervisor

Dr. Marcell Gáspár
PhD, Associate Professor

Miskolc, Hungary
2021

DOI: 10.14750/ME.2021.051

CONTENTS

DOI: 10.14750/ME.2021.051

DOI: 10.14750/ME.2021.051

SUPERVISOR RECOMMENDATIONS

Raghawendra Pratap Singh Sisodia was born in 1983 in Patna, Bihar, India. He graduated as a Master's in Engineering (Production Engineering) at the Delhi College of Engineering, University of Delhi with 70.95% in 2009. Then he worked for one year as a management trainee (production) in a reputed firm in India and undergone two months' work assignment for training on Installation, Development in production process, Operation, Testing, Dismantling & Packaging of Geogrid Plant at (Jiaozhou, Qingdao) China. In 2010, he started to work as an assistant professor in the Department of Mechanical and Automation Engineering at Amity University, Noida, U.P, India. He taught subjects for BSc and MSc students in numerous fields (Material Science & Metallurgy, Theory of Metal Forming, Management of Manufacturing Systems etc.). Between 2013 and 2015 he worked in a same position at the Galgotia's College of Engineering and Technology, Greater Noida, U.P, India and he continued his teaching activity in the field of Manufacturing Science & Technology, Project Management, Fluid Mechanics and Elements of Mechanical Engineering. During his carrier in India, he prepared two international journal papers and one conference publication related to field of gas metal arc welding.

In 2015 he moved to Hungary and started the Mechanical Engineering MSc of the University of Miskolc in CAD/CAM specialization within the Stipendium Hungaricum Scholarship Programme. During his master studies he showed high interest to the field of welding and physical simulation, therefore he was involved in the ongoing research activity of the Institute of Material Science and Technology about the welding of high strength steels. In February 2016 he started the laboratory work with our Gleeble physical simulator which is capable for the creation of the heat-affected zone (HAZ) of the welded joints. He investigated the HAZ softening of quenched and tempered high strength steel with the equipment. He graduated with excellent grades and got the Silver Medallion of Merit in recognition of his outstanding academic achievement. The applicant contacted me in autumn 2016 that he has plans for the PhD training in the University of Miskolc. Considering his professional calling, excellent academic results, and research experience, I have decided to be his supervisor.

From September 2017 till now he is a full-time PhD student in the framework of Stipendium Hungaricum Scholarship Programme at István Sályi Doctoral School of Mechanical Engineering Sciences; his affiliated organisation is Institute of Material Science and Technology. His selected research topic is experimental-based analysis of the beam welding processes on high strength steels. Although beam welding technologies have not been available yet at the Institute, he started the research work with the physical and numerical simulation of these innovative technologies, before organizing an experimental work at the industry. In 2019, he successfully performed the complex exam with 100% for the theoretical part and 93% for the dissertation part. On the 5th of March 2021 he got the Pre-Degree Certificate from the Doctoral School with 371.12 credits. In parallel with his PhD studies, between 2019 and 2020, he did the

DOI: 10.14750/ME.2021.051

International/European Welding Engineer (IWE/EWE) postgraduate programme at the University of Miskolc with excellent results (4.6/5).

Since 2018 he has been working as a part-time assistant research fellow at the Institute of Material Science and Technology, participating in European funded (2016–1–RO01–KA202–024450 "Implementation of International Guidelines for Risk Management in Welding Fabrication") and co-funded (GINOP-2.2.1-15-2017-00035 "Development of the production technology for aluminium packing device"; EFOP-3.6.1-16-2016-00011 "Younger and Renewing University – Innovative Knowledge City – institutional development of the University of Miskolc aiming at intelligent specialization) projects, furthermore industrial initiated (e.g. FGSZ Co.) R&D activities.

Besides his research activity he could use his previous teaching experience in the education of mechanical engineering MSc students (Advanced Materials Processing, Materials Behaviour Subjected to Welding) and he was a consultant of 5 Hungarian and 6 international students during their degree thesis.

He is the member of the Hungarian Welding Association (MAHEG), and an official delegate from Hungary in Commission IV "Power Beam Processes" of the International Institute of Welding (IIW). He inquiringly and actively participates in the welding seminars and workshops organized by the Institute and the MAHEG, which shows his commitment to the selected scientific field.

We have planned his experimental research work collectively, which strongly built on the results of the last 5-year welding-related PhD dissertations of the Institute. Due to his high-level motivation, it was managed to perform an extensive research work with the involvement of Hungarian and foreign industrial partners and by the utilization of the advanced materials testing methods of the University of Miskolc. The results of the research work have presented in doctoral seminars, doctoral forums, and international conferences including the IIW assemblies; scientific papers have prepared for journals and conference proceedings. During his doctoral programme he did an outstanding publication activity including 6 international journal papers with impact factor (cumulative impact factor is 10.748). He is a co-author in 13 journal papers and 11 conference papers.

During his PhD studies his knowledge, his affinity to research work, and his ability for holding of presentations have further improved. He has acquired new knowledge and competences, which can be utilised in his future scientific life. I am sure that his Stipendium Hungaricum Scholarship period has initiated the first steps of a promising academic carrier for Raghawendra Pratap Singh Sisodia, and the gained research and publication experience will be valuable and essential to the future research activity of the Institute.

Miskolc, 02nd July 2021

Dr. Marcell Gáspár
Supervisor

DOI: 10.14750/ME.2021.051

LIST OF SYMBOLS AND ABBREVIATIONS

GREEK LETTERS

α	Ferrite	N/A
γ	Austenite	N/A
$\alpha+\gamma$	Ferrite+Austenite	N/A
η	Thermal efficiency	–
σ	(Normal) stress	MPa
λ	Thermal conductivity	W/ (mmK)
$\Delta\sigma$	(Normal) stress range	MPa
$\Delta\sigma_D$	(Constant amplitude) fatigue limit	MPa
ΔF	Load range	N
ΔK	Stress intensity factor range	MPa $m^{1/2}$
ΔK_{fc}	Fatigue fracture toughness	MPa $m^{1/2}$
ΔK_{th}	Threshold stress intensity factor range	MPa $m^{1/2}$

LATIN LETTERS

a	Crack size or crack length	mm
a_0	Initial crack length (FCG specimens)	mm
AcC	Accelerated cooling	N/A
AHSS	Advanced high strength steel	N/A
B	Specimen thickness (FCG specimens)	mm
B_U	Upper bainite	N/A
BM	Base material	N/A
BWJ	Butt welded joint	N/A
C	Constant of Paris-Erdogan equation	–
CE	Carbon equivalent according to IIW	%
CCS	Cold cracking sensitivity	N/A
CCT	Continuous Cooling Transformation	N/A
CGHAZ	Coarse-grained heat-affected zone	N/A
CVN	Charpy impact energy (V-notched specimen)	J
d	Beam spot size	mm×mm
da/dN	Fatigue crack propagation rate	mm/cycle

DOI: 10.14750/ME.2021.051

DLBW	Diode Laser Beam Welding	N/A
DP	Dual phase steel	N/A
EBW	Electron Beam Welding	N/A
e	Expansion	mm
α-B	Ferritic-Bainitic	N/A
FGHAZ	Fine-grained heat-affected zone	N/A
FL	Fusion line	N/A
FZ	Fusion zone	N/A
FCG	Fatigue crack growth	N/A
FM	Filler metal	N/A
F_2	Joint type factor	–
f	Wire feed rate	mm/s
G	Gas flow rate	l/min
GB	Granular bainite	N/A
GMAW	Gas Metal Arc Welding	N/A
HAZ	Heat affected zone	N/A
HPDL	High power diode laser	N/A
HSS	High strength steel	N/A
HSSS	High strength structural steel	N/A
HSWS	High strength weldable steel	N/A
HTT	High temperature tempering	N/A
HV	Vickers hardness	–
I_b	Beam current	mA
IIW	International Institute of Welding	N/A
ICITs	Instrumented Charpy V-notch impact tests	N/A
ICHAZ	Intercritical heat-affected zone	N/A
k_m	Material constant	N/A
K	Stress intensity factor	MPa $m^{1/2}$
LBW	Laser Beam Welding	N/A
LEFM	Linear elastic fracture mechanics	N/A
L-S, L-T	Specimen orientations (FCG specimens)	N/A
m	Material constant of Basquin equation	–
M-A	Martensite - Austenite (island)	N/A
MAG	Metal Active Gas	N/A
M	Martensite	N/A
M	Matching	N/A
MVC	Micro voids coalescence	N/A
n	Exponent of Paris-Erdogan equation	–
N	Number of cycles (FCG)	cycle
OM	Overmatching	N/A

DOI: 10.14750/ME.2021.051

P	Power	watt
PWHT	Post weld heat treatment	N/A
Q	Linear heat input	J/mm
Q+T	Quenched and tempered	N/A
RA	Retained austenite	N/A
RS	Residual stress	MPa
RD	Rolling direction	N/A
s	Welding speed	mm/s
SC	Stress concentration	N/A
SCC	Stress corrosion cracking	N/A
SCHAZ	Subcritical heat-affected zone	N/A
t	Plate or specimen thickness	mm
$t_{8/5.}$	Cooling time from 800 °C to 500 °C	s
$T_{liq.}$	Liquidus temperature	°C
TIG	Tungsten Inert Gas Welding	N/A
TM	Tempered martensite	N/A
TMCP	Thermomechanical control process	N/A
TNr	No recrystallization temperature	°C
TPB	Three point bending test specimen	N/A
TRIP	Transformation Induced Plasticity	N/A
TRS	Tensile residual stress	MPa
T-L, T-S	Specimen orientations (FCG specimens)	N/A
TWIP	Twinning Induced Plasticity	N/A
UHSS	Ultra-high strength steel	N/A
UM	Undermatching	N/A
V_a	Accelerating voltage	kV
VHT	Specimen incised in heat-affected zone	N/A
VWT	Specimen incised in fusion zone	N/A
W	Specimen width (FCG specimens)	mm
WM	Weld metal	N/A
XRD	X-ray diffraction	N/A
1W, 21W 3W, 23W	Notch and crack path orientations (FCG specimens cut from welded joints)	N/A

DOI: 10.14750/ME.2021.051

1. INTRODUCTION, GLOBAL AIMS OF THE RESEARCH WORK

The development of high strength weldable steels (HSWS) has diversified the field of application, range of design alternatives subjected to more severe operation conditions than previous time. Several steel manufacturers have increased their interest in high strength steels (HSSs) or advanced high strength steels (AHSS)/ ultra-high strength steels (UHSS) [1]. Todays, categorisation of HSSs based on the tensile strength level whether it is HSSs or UHSS is cumbersome. So, using tensile strength as threshold for whether a steel qualifies as HSSs or UHSS is quite difficult. However, in general, above 600 MPa yield strength steels can considered as HSSs and probably above 960 MPa they can be considered as UHSS. Due to global environment, climate change and fuel crisis, the demand for lightweight structures from HSSs with the combination of higher tensile strength and toughness has increased over the last few decades [2][3][4]. As a result of it, there were several categories of HSSs developed according to their intended applications area (e.g. frames, cranes, bridges [5], automotive industry [6] etc). HSSs provide high strength to weight ratios, improved toughness and sufficient deformation capacity, acceptable weldability especially with undermatching (UM) and matching (M) filler materials (FM), while the overmatched welds can result increased cold cracking sensitivity (CCS) due to the higher carbon equivalent. Financial benefits can also be realized through reduced transportation and lifting costs (reduced weight), material savings (smaller/lighter cross-sections) and reduced weld volumes (thinner plates). Nowadays, HSSs application, in particular thicker plates for heavy steel structures getting more and more attention. HSSs with good structural safety in particular against the brittle fracture and acceptable fabrication properties (welding) are already in widespread application and in huge demands. However, main points to be consider while designing structure with HSSs should be fatigue analysis. Considering application areas, fatigue properties improvement, more strength and thicknesses etc., several production processes for HSSs were evolved which influences the final intended application and properties of the steels. So, it is important to understand how the microstructural and mechanical behaviour of these HSSs produced by the different methods influenced by the application of power beam processes. It has wide application in the vehicle industry but HSSs are also applied in the structural elements of skyscrapers (sustainable steel building) and bridges. HSSs decreases the dead weight of the structures from which the substructure and erection helped. It helps in the reduction of cross section of the welded joints which ultimately reduces the fabrication and inspections costs [5][7].

With the development of various new HSSs and their difficulty in weldabilities arises, leads to the requirements of the applicability's of new technologies of other promising innovative welding technological processes like Electron Beam Welding (EBW), Laser Beam Welding (LBW) etc. that can be applied for HSSs [8]. The application of these high energy density welding processes not only provides the quality joints to fulfil its intended function, but it also reduces the area influenced by the heat i.e., heat-affected zone (HAZ) to achieve mechanical

DOI: 10.14750/ME.2021.051

properties similar to the base material (BM). The use of innovative welding technologies like EBW, LBW etc. growing importance in the field of HSSs because of its excellence in providing quality of the welds, high welding speed, high power density, low heat input, ability to make exceedingly narrow HAZ, deep penetrated weld, low heat distortions. This stands in remarkable contrast to the fusion pattern in arc welds and is attributable to the unique penetration mechanism of the beam welding processes [9]. Regarding the economic advantages, the high productivity and the less FM costs should be emphasised. Due to the narrow and deep penetrated weld structure (keyhole technique) lower amount of FM is needed in EBW and in high power density (5×10^4 to 10^7 W/cm^2) [10] LBW processes. It can be also beneficial to the mechanical properties of the whole welded joints since in HSSs the weld can be similarly critical as the HAZ.

The weldability tests are the basis for the qualification of new welding technologies. However, the important parameter determining the weldability of the steels is the carbon content and the carbon equivalent (CE) [11]. A very high carbon equivalent value indicates poor weldability, and these steels are not suitable for structural applications, where welding is very important to assure structural safety [12]. The most important advantages of TMCP steels compared to other conventional steel grades of the same thickness is their outstanding suitability for welding, firstly, it reduced or completely eliminated the preheating of thicker plates before welding which significantly reduces the time and cost and secondly, its exhibit's higher toughness value and low hardening values in HAZ after welding [7][13]. However, good toughness value in the HAZ is a prerequisite for the application of welding processes with the high heat input. In case of quenched condition, strength is considerably higher than the required, but the material is too brittle for the structural applications. So, a suitable tempering of martensite microstructure required in order to get good combination of tensile strength and toughness properties. The alloying compositions of the quenched+tempered (Q+T) steels increases with the plate thickness in order to ensures sufficient hardening of the plate in the core region [7]. Therefore, the CE of a Q+T steels increases with the plate thickness.

The temperature-time cycles during welding have a significant effect on the mechanical properties of a welded joint. The cooling time from 800 °C to 500 °C ($t_{8/5}$) to characterize the cooling conditions of an individual weld pass for the weld metal and the corresponding heat affected zone for higher strength steel. The behaviour of the cooling curve in the temperature interval (A_3 to 500 °C, simplified to 800-500 °C) is decisive for the final microstructure and mechanical properties in the steels. Increasing heat input and interpass temperature leads to slower cooling and hence the longer cooling time $t_{8/5}$. To obtain satisfactory weld and HAZ properties, the welding parameters optimum and limited with increasing strength. The acceptable properties, especially toughness of the HSSs joints generally obtained in short cooling time. Although for lower cooling time, the hardness of the HAZ may exceed the limiting values and leads to the cold cracking in steels with high CE. On the other hand, longer cooling times results in the poor strength and toughness values [7][14]. So, the EBW and the LBW are the opportunity for the minimization of HAZ and fusion zone (FZ) where the material is brittle. Therefore, in the dissertation I tried to explore the details of $t_{8/5}$ related to the investigated beam technology. The comparative evaluation of various methods for determination of cooling times from 800-500 °C ($t_{8/5}$) in diode laser beam welding (DLBW) process of dual phase (DP) steel is presented. The thermal cycles and therefore cooling time were measured and compared using different measurement techniques (thermocouple measurement method and analytical method).

DOI: 10.14750/ME.2021.051

The weldability of HSSs consists of more challenges compared to mild steels (MS): hardening of the HAZ and higher CCS; reduction of strength and/or toughness of HAZ; selection of FM (mismatch) [15]. Therefore, new welding conceptions and special welding technology should be developed for these steels. Also, a deeper understanding of phenomena occurring during welding that influence the microstructure, and thus mechanical properties of welded joints, becomes an important issue in the broader application of these steels [16]. So far, the studies on EBW on high strength Q+T and TMCP with different yield strength (YS) have not been carried out extensively. HSSs and LBW are like two side of a coin, without each other they are incomplete and these combinations becoming so popular nowadays especially in automotive applications with using the latest technology in the field of LBW.

In real welded joints, HAZ properties can be limitedly analyzed by conventional material tests. The thermal cycles experienced by the workpiece during the welding can be easily reproduced and enlarged the volume of HAZ in small size specimen by using thermomechanical physical simulator called Gleeble. Therefore, physical simulator was used for the examination of microstructure and different properties in the HAZ areas of different grades of DP steels for different cooling time and heat inputs (Q). In case of the investigated Q+T and TMCP steels preliminarily HAZ simulations, performed at the Institute of Material Science and Technology were used for the analysis. The equipment provides the opportunity for very short time cycles e.g., beam welding processes since the specimen can be heated rapidly by resistance heating system with the maximum rate as high as 10,000 °C/s and cooled intensively due to the water cooled grips and external cooling if necessary. Another motivation for the application of physical simulators is the time- and material-saving, as compared to real welding experiments.

DP steel within the group of HSSs has become an important material of choice for automotive industry as it helps to improve energy absorption during impact, provides higher strength, and ensures a lightweight design and cost-efficient methods to produce automotive parts [17][18][19][20]. The laser welding of DP steels may result in a large amount of martensitic (M) structure in the FZ due to the rapid cooling during welding, leading to a considerable increase in the hardness. However, previous studies [21][22][23][24][25] showed also a significant softening in the HAZ of laser welded joint due to the tempering of the pre-existing martensite in the DP steels. In presented dissertation the effect of autogenous DLBW and the influence of post weld heat treatment (PWHT) on microstructural changes and mechanical properties of different grades of DP HSS butt welded joint (BWJ) are investigated. The high-power diode laser (HPDL) technology ensures high quality welded joints in HSSs, facilitate the welding and PWHT by same process and equipment. An advanced characteristic of HPDL, vital in the welding process and PWHT, is the rectangular or square shape of their laser beams [26]. PWHT reduces residual stress (RS) levels and tempers the hard regions, particularly in the HAZ. It is performed to temper the weld metal and HAZ with the aim of decreasing hardness and improving toughness, and decreasing the RS associated with welding. Furthermore, besides autogenous LBW, DP1000 HSS with a matching filler wire (MFW) is also welded with the aim to improve the mechanical properties of the weld.

The stresses developed by the thermal contraction of the cooling weld which must be compensated by the strain in the weld metal. The presence of hydrogen appears to lower the stress level at which cracking will occur. In rigid structures the natural contraction stresses are intensified because of the restraint imposed on the weld by the different parts of the joint. These RS can be more troublesome because it generates the stress concentration (SC) at joints, weld

DOI: 10.14750/ME.2021.051

toe, root of the weld and the possible chances of deleterious microstructures in the HAZ [27][28][29]. The higher degrees of strain which result produce higher risks of cracking for a given microstructure. Hydrogen embrittlement is strain-rate dependent and the risk of cracking is greatest at slow strain rates. As the straining rate is, or course, low during the final stages of cooling in the weld, the susceptibility to crack formation is high at this time [30]. The calculation and evaluation of the RS is highly difficult task in the welded specimen specially in the high energy beam welded samples due to its narrow weld and HAZ. The RS develop in the welded specimen is a complex combination of various factors like geometrical features of the weld, welding parameters, stiffness of the structure, manufacturing process, environment and volumetric changes due to phase transformations in the weld zone etc. [31][32][33][34]. The effects of the tensile residual stress (TRS) may lead to the structural failure, so the proper analysis of these stresses is important. TRS in the welded joints can cause higher mean combined applied stresses (MCAS) which negatively affect the fatigue life of the joint. The compressive residual stresses (CRS) considered beneficial as it reduces the mean compressive residual stresses (MCRS) which significantly improve the fatigue life of the welded joint, reduces the stress corrosion cracking (SCC) and brittle fracture.

One of the important issues that limits the applications of HSSs is fatigue. The fatigue resistance of the welded structures limits the use of higher strength steels in dynamically loaded structures. The fatigue of the welded material affects a wide range of application areas, e.g. cars, cranes, bridges, trucks, crankshafts. However, the rapid development of several fracture mechanical approaches for assessing the fatigue damage of welded joints have been developed. The HSSs welded joints affected by welding heat input and mechanical loads that increases the possible chances of deleterious microstructures in the HAZ, which causes inhomogeneous microstructure and mechanical properties. The inhomogeneity of the welded joints, material discontinuities and locations for stress concentration influences the behaviour of welded joints and cyclic loading condition which ultimately leads to the fracture of welded joints. Since the structures often have fatigue loading and these HSSs material have high crack sensitivity, therefore it is very important to know the resistance level to the fatigue crack propagation. On the other hand, the fatigue resistance of the HSSs can be improved by which reducing the notch effect of the weld, post weld treatments of the weld i.e., tungsten inert gas (TIG) dressing or grinding etc. (it helps in the reduction of notch effects). Therefore, these improvement in the fatigue behaviour can increases significantly the efficiency of HSSs in the structural applications [7]. FCG tests on EB welded HSSs (S960QL and S960M) joints are limitedly found in the literature. Therefore, it is aimed in this dissertation to compare the fatigue crack growth (FCG) characteristics of EBW HSSs joints with conventional gas metal arc welding (GMAW) since the EBW welds are prepared with narrow FZ and HAZ, without the application of filler material.

DOI: 10.14750/ME.2021.051

2. HIGH STRENGTH STEELS AND THEIR WELDABILITY

2.1.Classification and trends of development

In recent years, more stringent quality requirements and cost effectiveness have not only led to the various rationalization measures being adopted in European steel industry in the past but also to the significant technological advances. This is particularly apparent in the significant improvements in the HSSs with the combination of good strength and toughness properties but also in energy and materials efficiency that have been achieved [35]. HSSs have special types in plates (Q+T, TMCP) and other types in sheets (DP, TWIP etc.) for automotive industry.

Separating thin and thick plates is not an easy task. Welding science separates thin sheets from thick ones using heat transfer theories (Rosenthal, Rykalin, Goldak) [36]. In the first approximation, the heat dissipation of thin plates, the surface heat transfer is not negligible and the heat conduction is of secondary importance (2D model). In the case of thick plates, however, in addition to heat conduction, the heat transfer on the surface is negligible (3D model). However, the plates are are classified as thin plates (sheets) up to 3 mm, medium thick between 3 mm to 15 mm and above 15 mm it is considered as thick. The boundary between the models is not only based on the physical properties of the materials (ρ, λ, c_p etc.), but also depends on the welding technology (E_v, I, V_{arc}, v, T_p) [37].

Among the available HSS sheets, several types of HSSs were developed which primarily focused on the automotive industry based on the principle of light-weight design, innovative forming processes and new tooling concepts, as well. The main HSSs family used today in the automotive industry include steels with a Complex phase (CP steels), Transformation induced plasticity (TRIP), Ferritic-Bainitic (FB), Martensitic (MS) steels, DP steels, Hot-Formed (HF) and Twinning Induced Plasticity (TWIP) [38][39][40][41]. However, the most common HSS is in growing demand for wide application in the automotive industry is the group of DP steels owing to their good combination of high strength, ductility and formability. This approach enhanced the development of high strength DP steels, which contain a ferrite matrix and martensite island. This composition has a significant contribution in providing excellent ductility of DP steels and a strain hardening rate effect, which sustains higher stresses at higher strain rates. The above advantage of DP steels made them lucrative for intensive application in the field of vehicle industry. Nowadays, there are several grades of DP steels are available with different tensile strengths like DP600, DP800, DP1000, DP1200 and DP1400.

HSSs like S960QL, S960M grades find extensive uses in wider application areas like structures, cranes etc. due to its extraordinary material properties and acceptable weldability. Q+T steel grades with yield strength grades up to 960 MPa are standardized in EN 10025-6 “Technical delivery conditions for flat products of high yield strength structural steels in the quenched and tempered condition” and TMCP steel grades are standardized in EN 10025-4, “Thermomechanically rolled weldable fine grain structural steels” but constructional steel work

DOI: 10.14750/ME.2021.051

in Europe is still limited to steel grades with minimum yield strength of 690 MPa. Higher steel grades are still the main choice of the construction equipment industry but still not classified by the standard [42]. However, over the last three decades several development took place and many higher strength grade steels were developed above the 960 MPa yield point which found extensive application in production of high-loaded elements of travelling cranes, car lift and special bridge sructures [16].

Some types application field of HSSs are shown in Fig. 2.1.

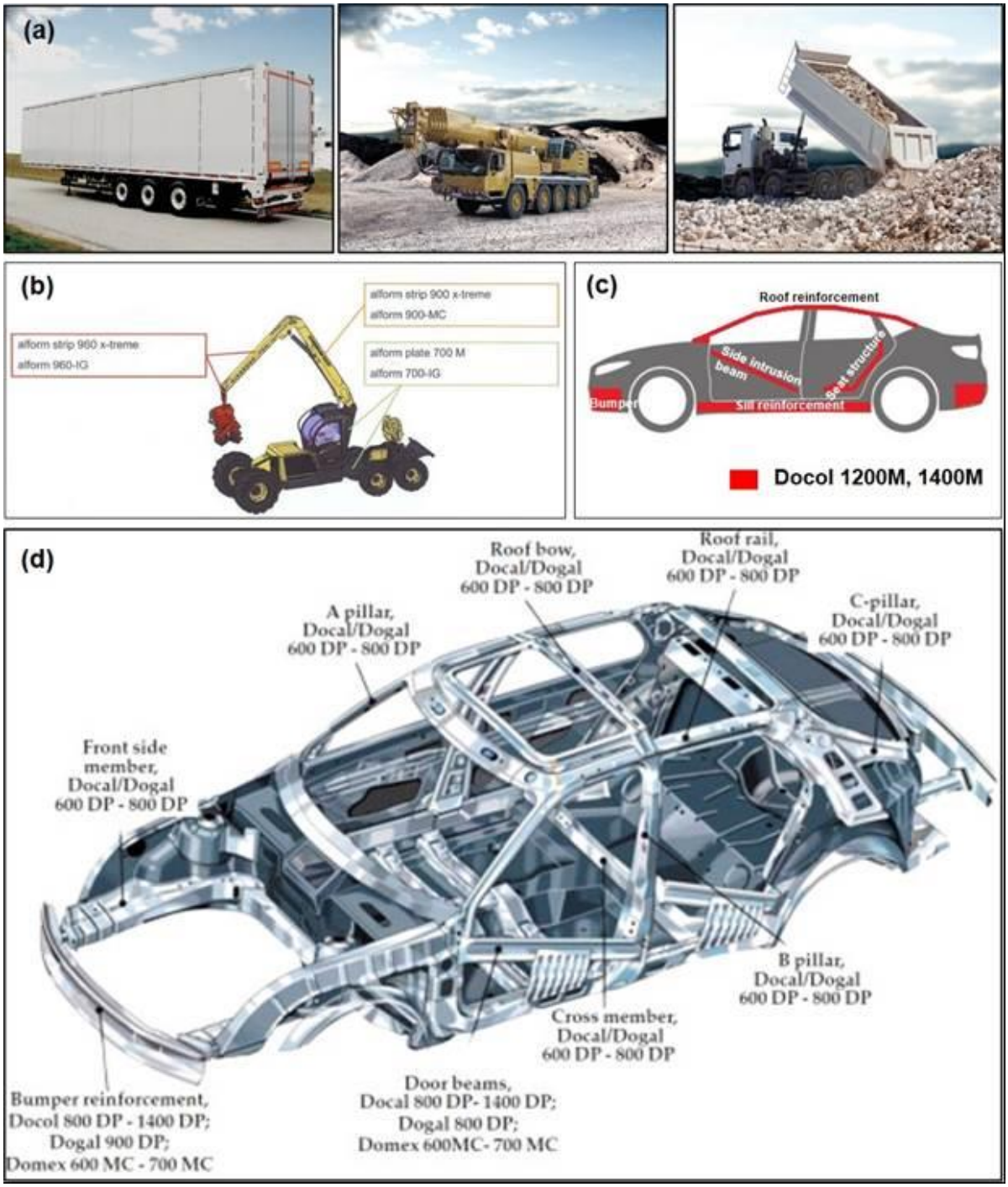

Fig. 2.1.(a) and (b) High strength structural steels (HSSS) [43][44][45]*;(c) and (d) High strength automotive steels* [46][47]

DOI: 10.14750/ME.2021.051

Among the large number of modern developing steels, different HSSs (Q+T, TMCP, DP steel grades) continue to play a leading role in their respective field of applications areas like in the case of engineering structures, automotive industries, S960Q; (industrial truck, dumptruck, lorries, trailer, bulldozers, excavators, cranes, bridges, lifting equipment, forestry machines etc.), S960M; cranes and lifting processes industry (base frame, crane jibs and crane columns), concrete pump cars, penstock, vehicles and steel contruction industry and architecture, trailer, agricultural and forestry machinery, earth moving equipments etc [43][48].

The current trends in HSSs development are to a great extent motivated by new environment of the end users, as carmakers are facing drastic changes in regulations that dictate new rules for both safety and fuel consumption which required special combinations of strength and formability parameters. Fig. 2.2. shows the grouping of traditional and advanced high strength steels which typically falls into the category of thin plates. The diagram represents the tensile strength and percent elongation of different steels grade. The figure illustrates well that the individual categories cannot be separated from each other strictly, only with overlaps. It can also be observed that each group is located along three characteristic curves, their characteristic values k_m is called the material constant.

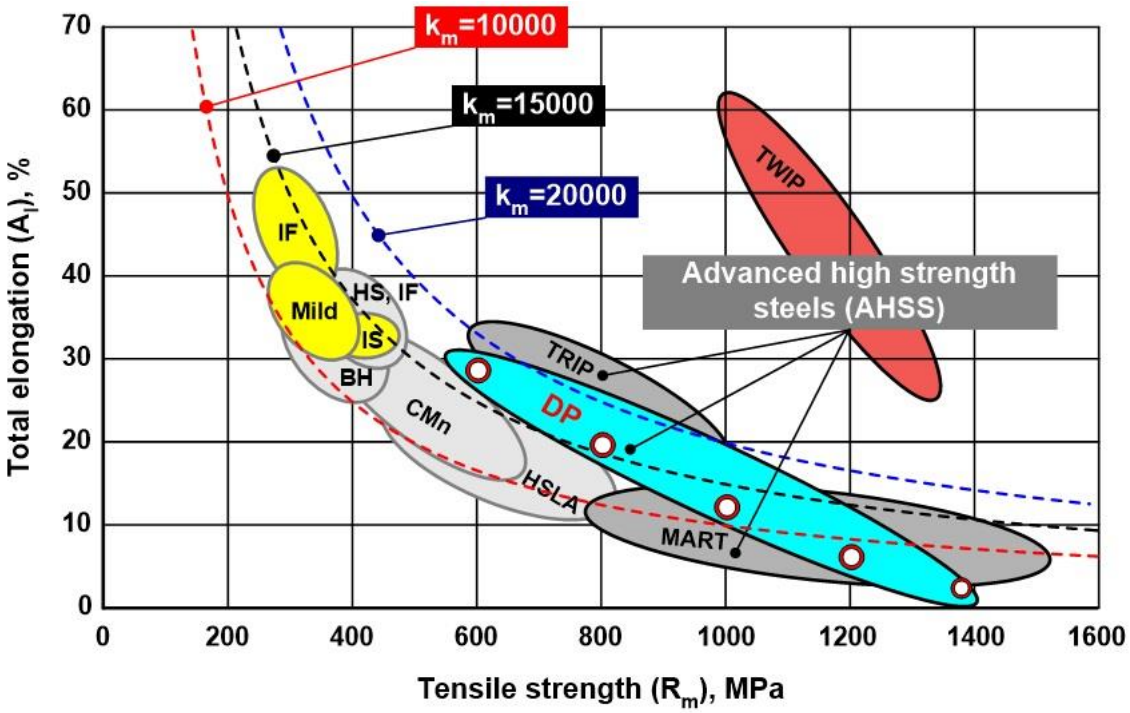

Fig. 2.2.Chronology of Automotive AHSS developments [38][39][41]

Related to medium and thick plates a series of developments took place in the production methods of HSSs (firstly Q+T steel, secondly TMCP and thirdly direct quenching) with the aim of improving the YS and good ductility [2][49]. Due to the technological advancement and growing demand of HSSs since the seventies, when Q+T group appeared, combination of varying alloying components along with the Q+T heat treatment process, now the maximum yield strength has been reached to the 1300 MPa. However, it should not be ignored that FM are currently available in the market are up to 1100 MPa of yield strength so for this extreme strength HSSs only undermatching (UM) (approximately 15-20%) is available if it is allowed.

DOI: 10.14750/ME.2021.051

However, the application of UM during the selection of the FM may have some additional positive effects (lower residual stress, higher fatigue resistance etc.). Due to the abovementioned reasons, instead of S1100Q and S1300Q, the S960Q is more widespread, which can be welded by MFW as well [50].

The development of the metallurgical process obtained by decreasing both production cost and unfavourable impurities in structural steel to protect it from lamellar tearing or hot cracking [16]. Generally, the ultra-high strength categories of structural steels are produced by Q+T process with a final microstructure of martensite [51][52]. Since martensite can only offer a high strength, improving its impact toughness has become a major concern [53]. It is well known that toughness can be improved by grain refinement without loss in strength [54]. Due to their outstanding mechanical (especially strength) properties, significant weight reduction can be achieved by their application. Besides their high yield strength, they have also good toughness properties because of the fine-grained tempered martensitic (TM) and partially bainitic (B) microstructure [16]. The strengthening mechanisms in these steels are: solid solution, phase transformation, grain and subgrain boundary, and precipitation strengthening [55]. By the improvement of the thermomechanical treatment (TM), combined with several heat treatment technologies (e.g. precipitation hardening), the yield strength of thermomechanically treated HSSs can approach the level of Q+T steels [56]. TM rolled steels require significantly less alloying elements, especially less carbon than normalised steels (NS) or Q+T steels. Due to the good weldability of TM steels, preheating during welding can be significantly reduced or avoided. The chronology of structural steel development trends with increasing strength of steels are summarised in Fig. 2.3.

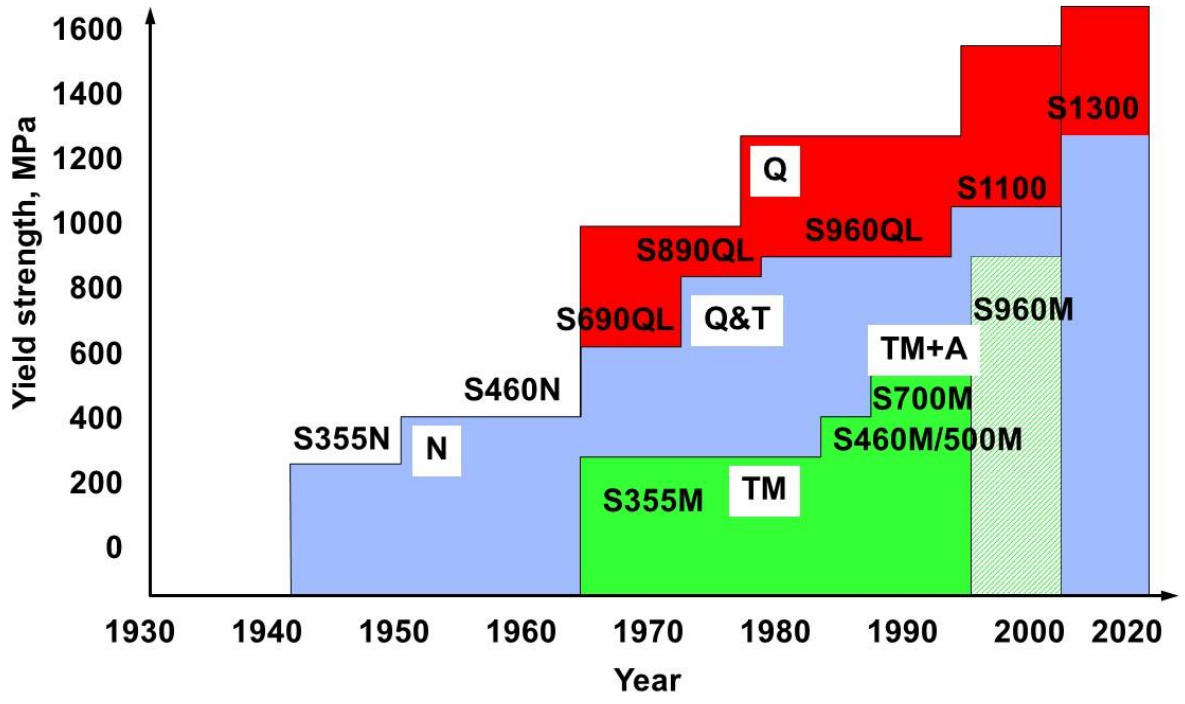

Fig. 2.3. Development trend of structural steels [8][13][14].

DOI: 10.14750/ME.2021.051

After the exhaustion the potential of normalised production technology, HSSs produced by quenched and tempering and thermomechanical treatment with refined grains structure. From Fig. 2.3, it can be seen with the development two technology viz. Q+T and TMCP, steels of higher strength can be produced. First, a steel with given strength category was produced with manufacturing technology typically consisting of quenching and high temperature tempering but with delay of 10-20 years strengthening of HSS was also achieved with a TM. It is also clear that the maximum strength achievable with steels produced by thermomechanical treatment is always lower than that of Q+T steels. A further disadvantage is that the plate thickness that can be produced is also smaller.

According to steel manufacturing companies data, the minimum yield strengths of (extra) HSS plates stated for Q+T steels 1300 MPa [57][58] and for TM steels 1100 MPa [59]. These mean that the highest available grades of Q+T and TMCP in Fig. 2.3 are nowadays available for users and development trends have shifted for higher strengths.

The relation between the cooling rate and the resulting phase can be predicted using the continuous cooling transformation (CCT) diagram. Fig. 2.4a and Fig. 2.4b. shows the CCT diagram S690QL [60][61] and S700MC [43] high strength steels respectively.

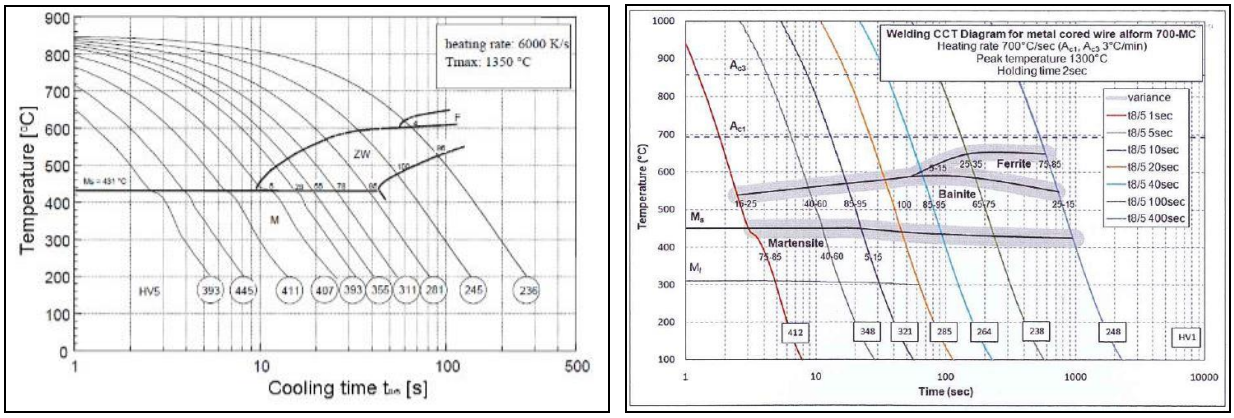

Fig. 2.4. CCT-W diagram (a) S690QL; [60][61] *(b) S700MC* [43]

The comparison between conventional toughening process and new technologies of production of structural steel belong Q+T type occur by apply heat treatment and conditions of rolling and kept the same chemical composition. For example, yield point increased 130 MPa, carbon equivalent decrease by 0.05%, and better weldability obtained by applying new production technology than conventional one [16]. The range of structural steel thicknesses will grow along with the development of metallurgical processes. In the case of these steels, one of the most important features of the successfulness of the weldability is the heat input (Q) which can be described with the linear energy (heat input per unit length). If the value of this is too low, the cooling rate of the welded joint may be too fast, and then cold cracks can be developed. In the opposite case (high heat input), strong coarse grain microstructure can be evolved in the HAZ, which can be caused by the decreasing of the strength and toughness features. The advantages of using steels with high mechanical properties are regards to the costs of transport, metal forming, cutting, and welding [11].

There are several possible ways to increase the strength of steels (e. g. grain size reduction; formation of a complex phases, like DP, TP and TWIP; precipitation hardening of the maraging

DOI: 10.14750/ME.2021.051

steels). In case of the examined heavy plate thickness range, the higher strength can be effectively reached by grain refinement and the change of the second phase quality, size and distribution [27][34][35].

During Q+T process, after a hot rolling above A_3 temperature, the slow cooling rate is generated until the plate cools down to room temperature. Then, the hot rolled plate is reheated above A_3 temperature, and held there for a short period, while the microstructure in the whole cross section transforms to austenite. After that, a quenching process takes place, when an extremely high cooling rate is applied, which can be achieved by water quenching [37]. In order to realize the quenched condition in the whole cross section, alloying components (Cr, Mo) are added to the steel, which moves the CCT curves to the right. Microalloying elements (Ti, Nb, V) are also used in order to ensure and preserve the fine grain microstructure. Then, in the tempering cycle (HTT: high temperature tempering) of the heat treatment process, the plate is heated under A_1 temperature, which is followed by a slow cooling process [62].

There are different elements effects on chemical composition during the metallurgical process of HSSs (Q+T, TMCP etc.) steels [37][62][63][64] as follows:

- Cr and Mo: decrease the critical cooling rate and increase hardenability; Mo increases tempering resistance and it is used as ferrite- and carbide-forming alloy of refined high-strength steels.
- Nb: fine grains of austenite during rolling and thus very tiny lamellas of supersaturated ferrite (martensite) after cooling. Tempering 600 ºC, precipitation hardening of NbC or V_4C_3 develop strength and impact resistance i.e. obtained a fine-grained structure with dispersive carbides.
- Ni: improve strength and toughness.
- B: a common microalloy below 0.005% in refined HSSs, improve hardenability. It improves the toughness in the form of fine carbide precipitates [37].
- Ti: Adequate amount of Ti needed to bind nitride in TiN and to avoid worsening the ductility of steel.
- V: addition of V gives a strengthening to the steels, tensile and yield strengths increase. It increases the strength in the form of precipitate hardening as well as by its grain refining effect. The maximum permissible vanadium content in the hardened high-strength steels is 0.12% [65].

2.2. Production processes and their influences on welding

With the increasing strength of steels by the addition of higher amounts of alloying elements and a tendency to result in higher hardenability. This may lead to a higher risk for brittle fracture and when used in welded structures it causes cold cracking (CC), in particular if the optimal processing parameters for welding are not applied. While the TMCP steel produced with accelerated cooling (AcC) a yield strength of 500 MPa in plates up to 100 mm thickness is obtainable with the use of very few alloying elements which provides excellent toughness values in the BM and in the HAZ of a welded joint [66].

The various production methods i.e. as rolled (AR), normalised (N), dual phase (DP), quenched and tempered (Q+T) and thermomechanically controlled steel (TMCP) steel are discussed below in brief.

DOI: 10.14750/ME.2021.051

2.2.1. Dual phase (DP) steel

The dual-phase steels are low-alloy steels which satisfy these requirements by exploiting microstructure in which there are two major phases, one of which is soft and the other significantly harder. The most common method of producing DP steels is by cold rolling of low alloy steels followed by intercritical annealing treatment in a continuous annealing line in which the steel is heated into the A_{c1}-A_{c3} ($\alpha+\gamma$) region and held, typically at 790 °C for several minutes (in the case of continuously annealed cold-rolled and hot-dip coated products) to allow small regions of austenite to form in the ferrite. The austenite phase will transform to martensite when quenching, provided the proper hardenability of the steel and a sufficient cooling rate. The result is a structure with a soft continuous phase of ferrite (α) with imbedded hard particles of martensite [67][68]. The strength of DP steels is determined by the ratio of the two phases.

2.2.2. Quenched and tempered (Q+T) steel

Fig. 2.5 shows that the initial step is in each case a hot rolling in the homogeneous austenitic field. For NS, this is followed by a normalizing heat treatment (A + B curve), while for quenched and tempered (Q+T) steels, a hardening and a high temperature tempering (curves A and C) are used. For steels produced by thermomechanical treatment (D-G curves), a much more complex manufacturing process can be observed.

Firstly, heating at temperatures of about 1100 °C, then rolling of the slab takes place in the austenitic state, a stable crystal structure is formed at high temperatures. After that the plate cools in open air and the "AR" condition is achieved (Process A in Fig. 2.5).

Further, to get a more homogenous microstructure an additional heat treatment can be performed. The plate should be reheated just above the ferrite-austenite ($\alpha+\gamma$) transformation temperature (about 800 – 900 °C, depending on the carbon content).

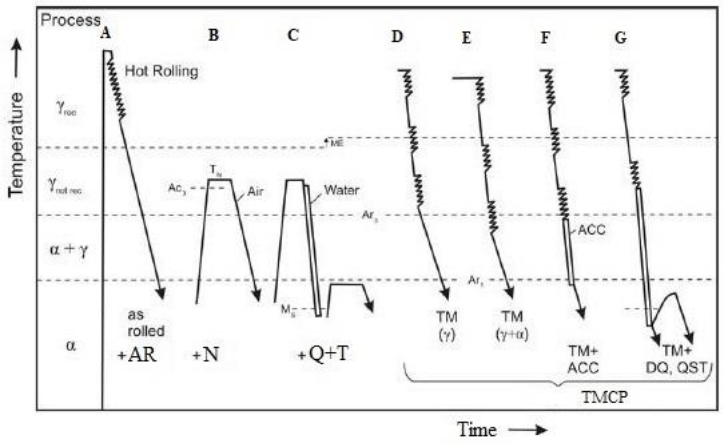

Fig. 2.5. Schematic illustration about the production of structural steels [66]

2.2.3. Thermomechanically controlled steel (TMCP)

The technology of controlled rolling and controlled cooling, TMCP contributes to the development of fine grained steels. It is one of the main production methods of high strength and high toughness structural steel materials [69]. The TMCP steels were originally developed to

DOI: 10.14750/ME.2021.051

fulfill the needs of the oil and gas industry. Their excellent field weldability and their good formability enable variable applications in different branches of industry (automotive, truck and crane industry, construction engineering) [70][71]. Later on, welding technology was applied to manufacturing of steel structures. It is then required that carbon content and CE in the steel should be lowered. In order to maintain strength level while carbon content is lowered, European countries starting with UK applied rolling technology based on low temperature rolling. The essential of this practice was the microstructural refinement of austenite leading to grain refinement strengthening contributing to strength increment in addition of solid strengthening by alloy elements and precipitation strengthening.

During thermomechanical treatment, the final rolling temperature is reduced from 1100-1200 ºC to 850-900 ºC, which significantly increases the pressure required for rolling. At this value, austenite is stable even at lower temperatures. When the material leaving the rollers, the austenite is significantly supercooled, so crystallization begins in an extremely large number of grains and thus the extra fine microstructure can be achieved. The aim of the subsequent controlled cooling is to maintain a small grain size and to ensure high toughness even at low temperatures. This process is described in curves of D-G in Fig. 2.5.

The diverse manufacturing technology is due to the different techniques of different steelmakers, not forgetting that thermomechanical treatment is more costly to manufacture than refining. Higher pressure requires higher load bearing rows, which means higher investment costs. Rolling time is usually longer, so productivity is lower; moreover, for larger plate thicknesses, the effect of both air cooling and water cooling is reduced, i.e. the resulting microstructure will not meet the expectations. Based on these, it is worth briefly addressing each variant [72].

As can be seen from Fig. 2.5, each variant from D-G start with a temperature above A_{r3} at a temperature higher than the no recrystallization temperature (T_{Nr}). This is followed in each case by a primary rolling, also above the T_{Nr}. As a result, the initial large austenite grains are transformed into a myriad of smaller size grains. The second rolling takes place already below the T_{Nr}, but still above the A_{r3} temperature, in each variant the in the austenitic state, the rolling time is different. As a result of second rolling many small-sized grains have an elongated, anisotropic structure. At this stage, the average austenite grain size is 20 μm [73].

In the case of the first variant (D), this is followed only by a controlled cooling phase, during which the elongated grains undergo further recrystallization, resulting in an extremely fine-grained microstructure overall. The elongated grains obtained during the primary rolling can be observed throughout the microstructure.

In the variant (E) when a third rolling was introduced between A_{r3} and the A_{r1}. The result observed that the elongated austenite grains will undergo even more intense recrystallization, i.e. the end result will be an even finer granular microstructure. In the variant (F), using AcC, which is usually achieved by water spraying the steel plate exiting the rollers, a similar microstructure can be obtained as in the case of variant (E), however, the grain size shows less variation. In the variant (G), during intensive cooling (DIC, according to other literature direct quenching DQ-T [74]), water cooling is also used, but a high temperature tempering (+Q+T) also takes place for a much longer period of time or immediately thereafter. In this case, it must be taken into account that by increasing the tempering temperature, the tensile strength decreases intensively, while the yield point does not change significantly, so the R_y/R_m ratio will approach to 1.0 by increasing the tempering temperature, which is mechanically unfavorable. According to various

DOI: 10.14750/ME.2021.051

experiments, the most favorable microstructure can be achieved in this case, however, the rate of intensive cooling is difficult to adjust precisely, and reproducibility is also questionable. At the same time, AcC and DIC technologies make it possible to produce the appropriate microstructure even for larger plate thicknesses. At the very end of the process, the average grain size obtained is 5–10 μm [73].

Combination of controlled rolling and controlled cooling lead to the formation of complete TMCP technology. Fig. 2.6 shows schematically the models of microstructure evolution of austenite and ferrite during controlled rolling and controlled cooling (rolling temperature down going to the right direction, on the upper level there is austenite microstructure evolution; while on the lower level, austenite microstructure models at the beginning of phase transformation), especially ferrite nuclei formation sites.

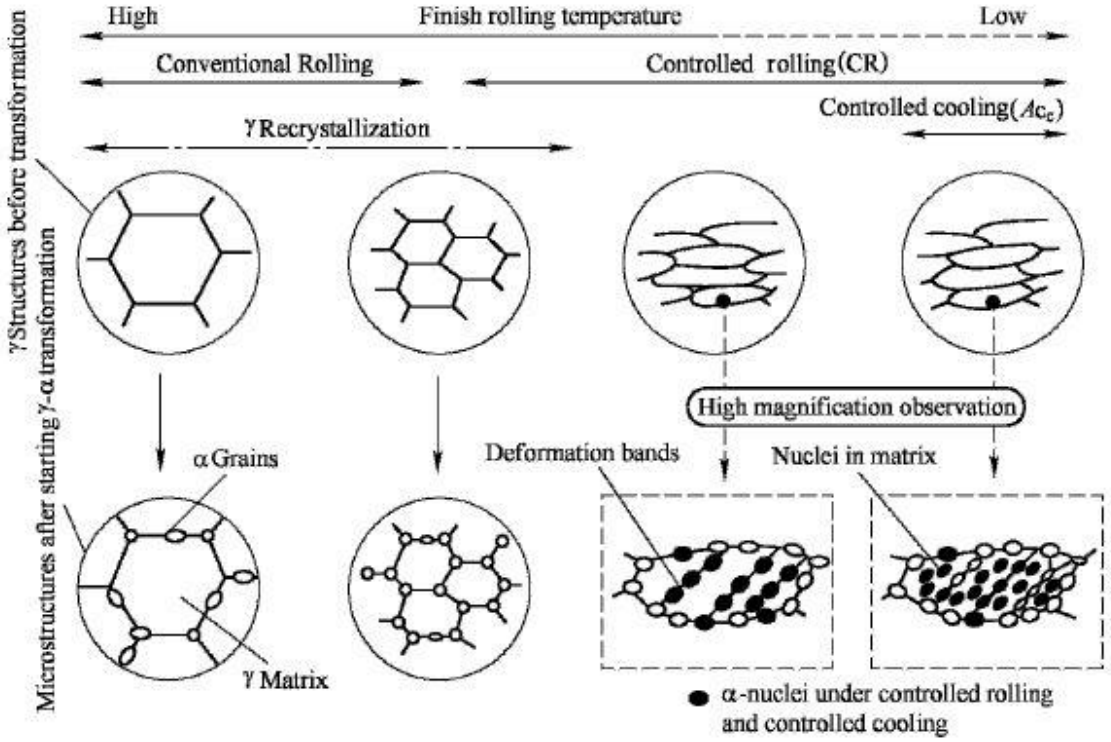

Fig. 2.6. Models of microstructure evolution during TMCP [69].

Application of TMCP technology for grain refinement and clean steel-making technology, together with the application of physical-metallurgical principles of solid solution strengthening, precipitation strengthening, and grain refinement strengthening lead to the formation of main stream of strengthening and toughening of structural steels, i.e. the processing routes used in steel plants for production of hot rolled high strength and high toughness steel products. Of course, there still are cold rolling, coating and other down-stream processes in steel plants. Dislocation strengthening due to cold rolling and other strengthening mechanisms are involved in later processing stages. Some steel plants also provide semi-parts and semi-components for machinery industry. After heat treatment and finish machining, these parts and components will have their final properties guaranteed. Nevertheless, fine grained HSS toughness steels produced by using TMCP has been recognized as one of the greatest progresses in the last decades in the field of steelmaking.

DOI: 10.14750/ME.2021.051

2.3. Weldability questions, mismatching, cracking phenomena

The major impetus in the development of various HSSs with with overall “property package” of very attractive mechanical properties brought a widespread adoption and prompting much interest from various industries. However, the practical application is only realized if it can be welded by means of arc welding or beam welding processes [75][76]. The wider applications of these steels would require changes and most importantly improvements in welding technology. That’s why, the weldability study is of primary importance and being a very important technological features of structural steels which depends on the processing, carbon concentration and alloying element composition [1][77]. Weldabilty is defined as “the capacity of a metal to be welded under the fabrication conditions imposed into a specific suitably designed structure and to perform satisfactorily in service” (American Welding Society, AWS). The difficulties arise in the welding of HSS due to its inhomogenous grain structures resulting from the alloys added to the steel and refining method used in the production of the steels. As a result, the HAZ of the welded joint has an extremely inhomogeneous microstructure and different mechanical properties compared to the BM. It is a difficulty that brittle parts formed locally in the HAZ as a result of the thermal cycle, especially in combination with a sufficient diffusible hydrogen content, can be sites of crack formation. Furthermore, the additional internal stresses due to welding and the low ductility of HSSs together increase the tendency to form cracks. The choice of FM is also much more complex for HSSs, as the manufacturing technology used in the production of the BM cannot be reproduced during welding, so it is difficult to choose a FM that guarantees sufficient weld strength and ductility to avoid cracking. In case of HSSs, the reduction of toughness properties usually occurred due to the effect of the welding heat input. The major problem that encountered during welding of HSSs are HAZ phenomena, cold cracking phenomena and mismatch phenomena.

2.3.1. HAZ phenomena

The HAZ is of major concern in a weldment since it can contains different subzones with variety of microstructure, joint geometries, stresses and thereby have different properties depending on the location in the HAZ. The time-temperature cycle during the weld process, in combination with the chemical composition in the base materials and its thickness governs the HAZ properties. When analysing the weldability of a steel it is of great importance to consider the peak temperature reached in the HAZ which has a major influence on;

- the dissolution of microalloying precipitates in the grain-coarsened HAZ,
- the austenite grain growth,

When welding a structural steel, heat input should be considered appropriately in order to avoid too much martensite in the HAZ and also limiting the softening [78].

The HAZ of HSSs causes problem primarily due to the reduced toughness and secondarily due to softening and hardening in some cases. In a welded joint made of HSSs, the brittle fracture may occur in the HAZ in addition to the weld, where the welding thermal cycles create a new, (predominantly) unfavorable microstructure. The HAZ of a single weld pass of a hot-rolled structural steel is generally composed of the following subzones [37][79][80][81] :

- Coarse grained heat affected zone (CGHAZ)
- Fine grained heat affected zone (FGHAZ)

DOI: 10.14750/ME.2021.051

- Intercritical heat affected zone (ICHAZ)
- Subcritical heat affected zone (SCHAZ)

Fig. 2.7 illustrates the structure of HAZ formed in the case of single welded pass.

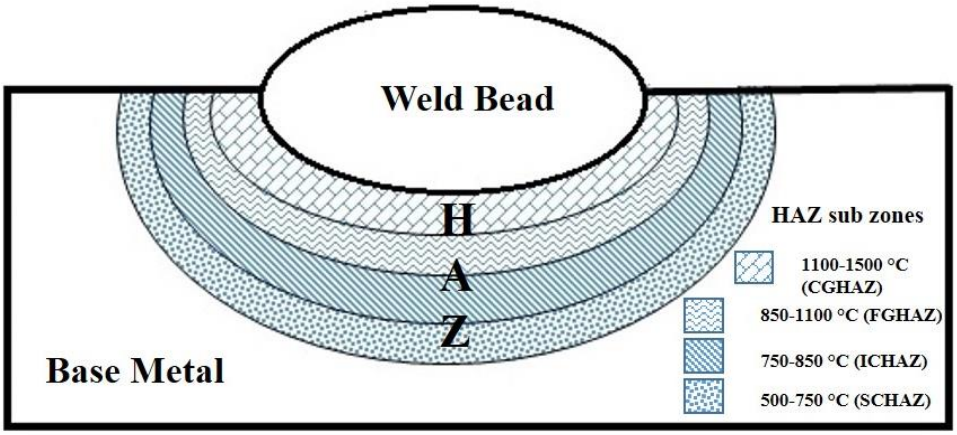

Fig. 2.7. Schematic diagram of HAZ, single pass weld [76].

In the case of the CGHAZ, the peak temperature immediate adjacent to the fusion line is well above the A_{c3} temperature, as a result of which the austenite grains (above 1100 °C) start to grow at an exponential rate as a function of the alloying content [68]. Thus the increasing effective grain size has an adverse effect on the critical stress level required for micro fracture, resulting in a higher transition temperature compared to its BM [55]. With the help of microalloys (Al, Ti, Nb, V) added to the steel, the dispersed precipitates at the grain boundary effectively prevent the grain coarsening, thus the expansion of the coarse-grained (CG) subzone [37][82][83]. This subzone can also be considered critical in case that the hydrogen diffusion in the seam that can cause cold cracks when entering the CG subzone [84]. Martensite-austenitic (M-A) islands, which result in relatively brittle parts, can also be formed as a result of a relatively long thermal cycle, which can further reduce toughness [83]. In the case of structural steels, the highest hardness can usually be measured in the CG subzone, since the high austenitic temperature in this zone also favors the martensitic transformation. As a result, this subzone of the HAZ is the most dangerous in terms of cold cracking.

HAZ with fine grain structure is heated to temperature above A_3 (900 °C ≤ T_{max} ≤ 1100 °C). The toughness of FGHAZ can be as high as the BM, however in some HSSs hardness peaks are observed in this subzone.

In general, the CG zone is remembered for the decrease in toughness in the HAZ of structural steels, but when welding HSSs, the study of the intercritical zone can also be interesting. Moving away from the normalized zone next to the coarse grain towards the BM between A_{c1} and A_{c3}, the austenitic transformation takes place only partially, so a rather heterogeneous microstructure is formed here. In favorable cases (e.g. with a low alloy content), the resulting microstructure has good mechanical properties, so in the case of some HSS, intercritical annealing is used to improve the strength properties [85]. Due to the characteristic carbon content of hardened HSSs, sometimes approaching the 0.20% limit, and alloys that help the tendency to harden, a decrease in toughness relative to the BM may occur in this zone. The γ-α transformed parts formed at the boundary of the original grains typically have a higher carbon content because austenite has a

DOI: 10.14750/ME.2021.051

higher carbon solubility in this temperature range. If high linear heat input is used and this zone remains in the intercritical range for a long time, the carbon concentration of the austenitized parts is further increased by diffusion. Subsequently, in the cooling stage, these carbon-enriched, austenite-like parts are transformed into microstructure that are more brittle than the base metal and have martensite properties depending on their chemical composition and cooling rate. Meanwhile, parts that are not transformed during heating are relaxed as a result of the thermal cycle, and their carbon content also decreases, so in many cases they soften [68]. In addition to the resulting brittle martensite microstructure, retained austenite (RA) can be detected in many cases (M-γ islands). The brittle portions located between the transformed, relatively softened microstructure represent local brittle zones (LBZ) in the welded joint [68][83].

As the yield strength of structural steels increases, increased attention should be paid to the tendency of the HAZ to soften, which can occur primarily in the intercritical and subcritical zone. Subcritical HAZ heated to temperature below A_1 in the range (450 °C ≤ T_{max} ≤ 700 °C). Due to their tempering, Q+T HSSs are less prone to hardness or strength loss during the thermal cycle below the tempering temperature, so the subcritical zone will only tend to soften at higher linear heat input [55][86].

2.3.2. Cold cracking Phenomena

Cold cracking generally occurs during cooling of welded joints and is formed with the participation of microscopic stresses arising from martensitic transformation of austenite in the HAZ. One of the basic characteristics of HSSs is that as the strength increases, the ductility decreases, which indicates an increased tendency to brittleness. In such steels, the impurity is due to advanced still metallurgical processes content is minimal (according to EN ISO 10025-6 [65]: P ≤ 0.025%, S ≤ 0.015%, L category upto P ≤ 0.020%, S ≤ 0.010%), therefore there is no issue of the appearance of hot cracks (crystallization or liquidation cracks) during welding. This fact is supported by the limited nickel content of 2% in the BM, which would increase the susceptibility to hot cracking in larger quantities and in the presence of sulphur.

However, the risk of cold cracks, another large group of cracks in welded structures, is significant; as the strength increases, the CCS increases. The tendency to cold crack is basically influenced by the combined effect of three factors [37]:

- Dissolved hydrogen in BM and HAZ,
- Tensile stresses,
- Low ductility microstructure such as martensite.

Q+T steels possess higher hardenability than normalised or TMCP steels and therefore there is an adverse microstructural influence such as the greater likelihood of forming martensite and/or bainite [75]. The study of previous researchers confirms the HSS susceptibility to the cold cracking. Opiela [87] investgated that the welded joint HSS (up to the yield strength of 960 MPa) are susceptible to cold cracking in both HAZ and FZ. Laschowicz and Nosko [88] also revealed that the Weldox700 steels shows the tendency of HAZ hardening and cold cracking. Also the results of S890, S960, S1100 as well as S1300 steels have the same problem of cold cracking [76].

The degree of hardening in the HAZ is an important consideration determining the weldability of a carbon or low-alloy steel. Weldability and resistance to cold cracking generally decrease with increasing carbon or martensite in the weld metal or the HAZ, or both. Although carbon is the most significant alloying element affecting weldability, the effects of other elements can be

DOI: 10.14750/ME.2021.051

estimated by equating them to an equivalent amount of carbon. Therefore, the effect of total alloy content can be expressed in terms of a International Institute of Welding (IIW) carbon equivalent (CE) (Equation 2.1.).

$$CE = C + \frac{Mn}{6} + \frac{(Cr + Mo + V)}{5} + \frac{(Ni + Cu)}{15} \qquad 2.1$$

Steels with CE below about 0.45 are readily weldable with appropriate procedures but CE greater than 0.45 indicates a need for caution. Most structural carbon and low-alloy steels that may be susceptible to cold cracking transform from austenite during cooling through the temperature range of 800 to 500 °C. The length of time, steel spends in this temperature range during cooling will establish its microstructure and hence it's cracking sensitivity. This time segment is generally referred to as $t_{8/5}$ (in seconds) [86]. While considering the relation of cooling time ($t_{8/5}$) and toughness in case of HSS, it was observed that the cooling time of the welded joint influences the toughness of HAZ and thus the resistance to brittle fracture of joint. The transition temperature to brittle of HAZ increases with the increase in cooling time ($t_{8/5}$) [89]. Gáspár [14] observed in his study that the HAZ physical simulations (CGHAZ, ICHAZ) of S960QL HSS in the whole $t_{8/5}$ range whether the $t_{8/5}$ was short (2.5, 5 s) or long (10, 15, 22.5, 30 and 100 s), it was always brittle. Therefore, the application of EBW process can provided a unique possibility to reduce tendency to brittle fracture due to the narrow HAZ compared to arc welded joints. The main reason for the increase in brittleness at longer cooling time is the disappearance of the tempered martensite microstructure in the favour of a martensitic and upper-bainitic mixed microstructure [90]. Therefore, a proper selection of cooling time is very crucial because too short cooling time can cause hardening of HAZ (increase in cold cracking sensitivity) while too long cooling time limit the toughness of HAZ [76].

In addition to the microstructure, another factor that causes the appearance of cold cracks is hydrogen. Hydrogen can come from steelmaking or can be used in subsequent uses (welding, corrosion protection, presence of high pressure hydrogen gas etc.). During welding, the hydrogen molecules in the arc decompose into hydrogen atoms, which, due to their small size, are able to move by diffusion in the lattice gaps. The activation energy required for diffusion motion is available in the form of thermal energy at high temperatures, however, as the temperature decreases, the solubility of hydrogen decreases. In sufficient time, hydrogen, which has become insoluble during crystallization, is removed from the molten metal by diffusion. In the welding process, there is usually no time for the diffusion process to take place completely, so large amounts of hydrogen accumulate at locations with larger gaps (grain boundary, lattice defects, dislocation sites). Hydrogen is thus forced to precipitate again, preferably in molecular form, however, the diameter of the hydrogen molecule is much larger than the diameter of the hydrogen atom, so the molecular form is incapable of further diffusion. The diffusion of hydrogen molecules in such places brittles the material (prevents the movement of dislocations), and the pressure of hydrogen gas increases so much that the bond between the grains is broken locally, cracks are formed [79][84]. Depending on the boundary conditions, the resulting cracks can even reach a critical size leading to rapid brittle fracture [55]. The hydrogen content can be significantly reduced by choosing the right filler material, cleaning and keeping the surfaces to be welded and their surroundings clean, using the right quality shielding gas, and choosing the right welding parameters [76].

DOI: 10.14750/ME.2021.051

The tensile stress required for the propagation of cracks is present in all restrained welded joints due to thermal expansion, however, its magnitude can be reduced in almost all (realistic) structures by consciously choosing welding parameters and optimizing the welding sequence. In the case of HSSs, in addition to the factors described above, the reason for the increased tendency to crack due to hydrogen is also due to the higher residual stress on the three-axis tensile due to the increased yield strength.

As an alternative approach adopted from some countries is the Graville diagram as shown in Fig. 2.8. which separates structural steels into three zones rated by their ease of weldability, zone I easily weldable, zone II weldable with care, and zone III difficult to weld [56]. From this diagram it can be seen that with increasing carbon equivalent the weldability decreases but it also emphasizes the extremely important effect of carbon content on weldability. Reducing the carbon content of steel is the most effective way to improve its weldability [79][91].

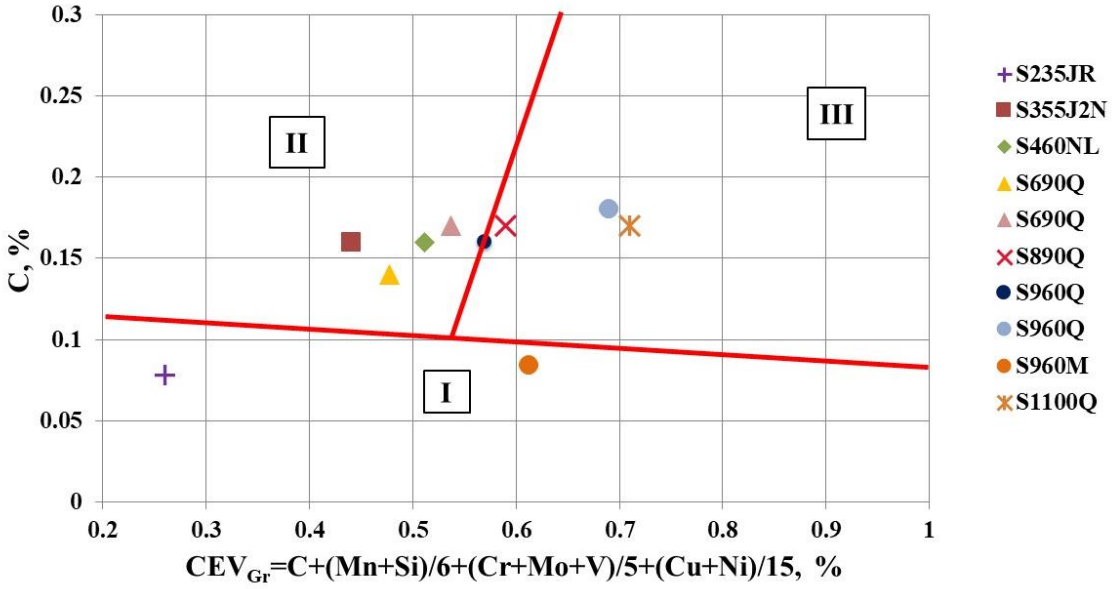

Fig. 2.8. The Graville diagram [79].

The CE or CEV is also utilized to assess preheat requirements for a welded joint or assembly, and to take into account the influence of hydrogen and joint restraint. According to the classification of the Graville diagram preheating and controlled linear heat input should be used for the welding of Q+T HSSs. As it can be seen Q+T steels mostly belong to the zone III (S890Q, S960Q, S1100Q), where steels have both high carbon and high hardenability, and all welding conditions will produce crack-sensitive microstructures. By considering these technological criteria the risk of cold cracking can be reduced, and the welded joint has better toughness and strength [15]. However, the investigated S960M thermomechanical steel is situated in the area I, so it has relatively low carbon and low hardenability and therefore it is less susceptible to cold cracking. The determination of preheating temperature and linear energy is the most important duty of engineers during planning the welding technology of HSSs.

The microstructure of the S960M steels produced by using TMCP processes is mainly composed of lath bainite packets, martensite and acicular ferrite (AF) [92]. There can be some degree of softening in the HAZ of TMCP steels after welding. Reduction in joint strength,

DOI: 10.14750/ME.2021.051

however, is unusual, in those that have not had accelerated cooling as part of the manufacturing process. TMCP steels that have been manufactured using an AcC method to achieve the desired properties are not generally resistant to high heat inputs, and a degradation of properties can occur on welding. This is because the cooling rate in the weld region may be slower than that of production. In these steels, it is important that the cooling rate is high, so that the grain size of the weld and HAZ can be maintained to give the desired properties. This is achieved by the use of moderate heat input levels, typically ≤ 2.5 kJ/mm for 15 mm plate in these steels or TMCP there is a need that the HAZ shall not be too wide and too soft, i.e. a maximum cooling time $\Delta t_{8/5}$ has to be limited. This differs with heat input, hydrogen content, plate thickness and carbon equivalent.

2.3.3. Mismatch Phenomena

Filler materials are most often selected on the basis of chemistry match. However, other considerations sometimes take precedence, such as ferrite control in the welding of stainless steels, distortion/residual stress control for high-strength steels, optimization of elevated-temperature properties for nickel-base superalloys etc. Filler metal also has quite a considerable effect on the welded structure of HSS depending on the yield strength of filler metal corresponding with the yield strength of base metal. One major drawback when developing filler materials for such grades is that, high amount of alloying elements are used which can result in severe cold cracking problems.

The filler metal can be classified as undermatched, matched or overmatched. The filler metal is undermatched when the yield strength of the filler metal is below the yield strength of the base metal. Matched filler metals have nearly the same yield strength as base metals, and overmatched filler metals have yield strength greater than the base metals. Generally, HSSs are welded by undermatched or matched filler metal, and overmatched filler metal is infrequently used as confirmed by Porter [93]. Undermatched welds have proven to be effective with HSSs, reducing the need for preheating. Undermatched welds lead to lower residual stresses than matched welds, which has the potential to reduce crack initiation. The properties of the weld metal are also a factor in the effectiveness of undermatched welds on HSSs. The results of restraint cracking tests indicated that the application of undermatched welds to HSSs leads to the reduction of minimum preheating temperatures and thus preventing cold cracking on the weld metal. It is necessary to consider not only the strength of weld metal, but also its ductility, fracture toughness, and hydrogen content when selecting weld metals for undermatching. Undermatched welds have similar fatigue characteristics to matched welds, where both undermatched and matched welds have similar crack propagation rates [94]. Another key parameter in welding of HSSs is correct selection of a filler material with respect to the base metal to obtain sufficient weld strength. Although, when welding HSSs with a yield point higher than 800 MPa, it is recommended to select a filler metal with a yield strength that is not lower than the yield point of the base metal [95][96]. Some other studies have shown that the required strength of welded joints made of Q+T HSS can be obtained when filler metal with a lower yield point are used (undermatching filler material). In such cases, in addition to lower costs, the propensity of joints for cold cracking can be reduced as well [86].

DOI: 10.14750/ME.2021.051

2.3.4. Case studies

- M. Gáspár and A. Balogh [62] studies of GMAW of 15 mm thickness S960QL plate presented optimal mechanical properties obtained at lower cooling time (5-6 s) with lower linear energy of 700 J/mm. Although, the hardness peak can be even above 400 HV in this case. Generally, the upper limit of linear energy, which gives acceptable mechanical properties, is 900-1000 J/mm. When larger linear energy is set, the tensile strength and impact energy reduces under the required minimum values;
- M. St. Węglowski and M. Zeman [77] investigated the cold cracking sensitivity in GMAW of Weldox 1300 steel with 10 mm thickness. The energy input was used are 1920 and 800 J/mm. the preheating temperature has a complex influence over the cracking process. The minimum temperature that allows to avoid cold cracking can be estimated as 100 °C regardless of heat input;
- F. Hochhauser et al. [97] studied the influence of softening in the HAZ and the constraint effect on the transverse tensile strength of a microalloyed, TMCP high-strength steel grade, C< 0.12%, Mn< 2.1%, Si<0.6%, Nb<0.09%, Ti<0.22%; tensile strength=750-950 MPa; yield strength ≥ 700 MPa. GMAW welding process was used with 6 mm plate thickness. Three different energy input are 420, 530 and 760 J/mm was used and their corresponding cooling time was 5.5, 8.5 and 18.5 s respectively. The results showed that the tensile strength was not significantly compromised by softening in the HAZ. The reason for this is the constraint effect of the base metal and the high strength of the weld metal. In conclusion low heat input welding processes keep the soft zone small and the strength high. Hardness drop in the HAZ of the welds could be attributed only to transformation softening effects. The width of soft zone increases linearly with the cooling time.

2.3.5. Recommendations to the aims

- Q+T, TMCP and DP steel base materials with different strength categories are in the focus of the researchers within the group of HSS, therefore they are worth to be investigated;
- The cooling time ($t_{8/5}$) should be analysed to understand the microstructural properties and its effect on the mechanical properties.
- Detailed HAZ characterization of the investigated HSSs grades are needed in order to identify hardened and brittle zones, softened zones;
- Beam welding processes should be applied to utilize its outstanding characteristics features (low heat input, narrow HAZ, fast welding speed etc.) and influence on the joint quality and HAZ should be analysed;
- Mismatch phenomenon should be investigated in terms of the autogeneous EBW and compared with GMAW matched welds.

2.4. Physical simulation of HAZ

The physical simulators available today are an inevitable opportunity in the development of increasingly HSSs and the corresponding welding technology associated with them. For a given steel, the physical simulator can be used to determine the welding parameter and to analyze the tendency of the steel to be tested for cracking phenomena. On the other hand, physical simulation provides an opportunity to consciously develop steels that take into account the

DOI: 10.14750/ME.2021.051

adverse effects of welding technology and compensate for it (e.g. by microalloying) [14]. Physical simulation of material technology processes means tests performed under laboratory conditions that accurately reproduce the thermal and mechanical processes that reach a given material during real operations. In another word, physical simulation is the realization of real technological processes in (nearly) real time and geometrical step [86][98]. Thermophysical simulation of welding importantly reduces the process of selecting optimal welding parameters and standardising the welding procedure and it also reduces total cost of the weldability tests. The data obtained by this weldability testing methods are repeatable and verifiable, so that can be used with sufficient reliability in selection of optimal welding parameters and standardisation of welding procedures [99]. Gleeble systems typically can run thermal tests 3 to 10 times faster than conventional furnace equipped machines [100]. The major problem of performing basic investigations on HAZ microstructures in actual welds is the presence of extremely narrow and inhomogenous subzones however the simulator facilitate to enlarge the volume of HAZ while considering the different welding processes e.g. LBW, EBW, GMAW, TIG etc. during simulation experiments [101]. The other advantage provides to simulate the combined HAZ zones formed in the case of multipass welding. It is one of the most accurate and reliable methods of HAZ characterization. This can be further used for metallographic examination as well as for different standarised mechanical testing procedures such as impact tests, tensile tests, fatigue tests etc. The test specimen can be heated at a speed of up to 10,000 °C/s by direct resistance heating (depending on the dimensions of the specimen). In order to achieve a steady state, the specimen can be kept at a constant temperature with high accuracy, in which a uniform temperature distribution can be achieved in the tested part. The specimens shall be placed in high thermal conductivity clamps to facilitate higher cooling speed. This can be as high as 10,000 °C/s, depending on the size of the specimen and the cooling conditions. Given the typical specimen dimensions and the heating-cooling technique used, the differences between the thermal cycle on the surface and inside the piece are usually negligible. To achieve the desired thermal cycle, the feedback is provided by thermocouples [98].

HAZ of welded joints is such a narrow in width, and consists of very fine subzones having different structures. When the toughness of the critical subzones of the HAZ can be tested in the traditional way only on the side of the fusion line of the “half-V” and “K” welds, which is considered to be quasi-straight (as shown in Chabelka test), however, there is still a high degree of uncertainty as to whether the impactor incision passes through the zone to be tested. In addition, the radius of incision of a standard impactor (R = 0.25 mm) usually exceeds the width of a critical HAZ subzone [102]. Thus, it is very difficult to analyse the effect of characteristic microstructure on toughness using true weldment. Using the physical simulator, the desired subzones of HAZ, depending on the distance between the jaws and the test parameters, up to 5-6 mm wide, homogeneous structure can be produced. Heat processes in different subzones of the HAZ are determined by known welding thermal cycle models (e.g. Hannerz, Rosenthal [103], Rykalin [104]) provided in the available QuickSim software with equipment can be used to describe different thickness of the materials to be simulated.

HAZ properties and microstructure depends on the accurate simulation of thermal cycles corresponding to the peak temperatures using suitable HAZ thermal simulator. However, several methods were developed to predict the thermal cycle in the various subzones of HAZ during welding. Some of them based on the thermal properties of the materials whereas others were measured based on the experimental method. So, there must be appropriate HAZ thermal

DOI: 10.14750/ME.2021.051

simulation program which can authentically replicate the actual thermal cycle experienced during welding within reasonable limits [105]. Therefore, the similarities and differences among the HAZ thermal cycles obtained by the different methods should be fully studied and understood and the same is presented in the dissertation.

2.4.1. Case studies of physical simulation

- J. Wang, L. Yang et al. [106]: presented the study of softening mechanism of DP1000 steel and Gleeble 3500 thermal simulator was used to simulate the welding thermal cycles of all the subzones of the HAZ of laser-welded specimens. Softening was observed in two subzones, firstly in the ICHAZ, when the ferrite transformed from the martensite and some of the ferrite in the original microstructure were transformed into austenite. Secondly, in the tempering zone i.e. SCHAZ because the martensite in the original microstructure precipitates carbides and then forms tempered martensite, the hardness of tempered martensite is lower than that of quenched martensite, which decreases the hardness.
- Q. F.Wang, C.J. Shang, R.D.Fu et al. [107]: studied the physical simulation and metallurgical evaluation of HAZ of ultrafine bainitic ferrite steel during laser welding. The thermal cycle was determined from actual laser welding. The rapid thermal cycle of laser welding imposed on the HAZ was physically simulated using a Gleeble simulator equipped with a special isothermal quenching device (ISO-Q™), and a relatively large volume of HAZ with a homogeneous microstructure was obtained. In real experimental laser welding process the major challenges are an abrupt change in microstructural phenomena and actual assessment of the mechanical properties due to very narrow HAZ and partly to high mechanical properties gradient. The hardness measurements revealed that the rapid thermal cycle of laser welding increased the hardness of base steel and resulted in an abrupt hardness distribution in the HAZ, whereas, the relatively slow thermal cycles for the post-weld laser tempering created a relatively soft microstructure that transformed at a lower cooling rate.
- C. Lundin and G. Zhou [101]: showed a comparison of six thermal cycles in ferritic steels by different methods namely HAZ calculator, the F(S, d) program, Hannerz, Ryaklin-2D, Rykalin-3D and Rosenthal methods. The main aims to present the comparison results is to show the similarity and differences among the HAZ thermal simulation calculation methodologies to predict the actual HAZ thermal conditions. The thermal simulation is the key approach to define the unique microstructure and the properties of the weld HAZ which specially relies on the accurate simulation of the thermal cycles corresponding to the different peak temperatures and it is also influenced by the combined effect of the various input parameters such as heat input, preheat temperature, plate thickness and welding process.
- M. Lomozik [105]: presents differences in the characteristic of structural steels in thermal cycle in welding conditions compared with the cycle of a traditional heat treatment. CCT-Welding diagrams constitute a source of essential information about the impact of welding thermal cycles on the structure and properties of steel being welded and thus highly facilitate the development of welding technologies.
- R. Laitinen, D.A. Porter, L.P. Karjalainen et al. [108]: evaluated the HAZ toughness of an offshore and an UHSS by physical simulation and used the most critical subzones of the HAZ. HSS (offshore steel, 500 TM1, thickness = 40 mm & 500 TM2, thickness = 35 mm), $t_{8/5}$ = 5 s and 30 s, CGHAZ, ICHAZ and intercritically reheated coarse-grained heat-affected

DOI: 10.14750/ME.2021.051

zone (ICCGHAZ) zones were simulated. For HSS (S960QC, thickness = 6 mm). CGHAZ and ICCGHAZ zones were simulated using $t_{8/5}$ = 5, 10, 15 and 20 s and the ICHAZ zone using $t_{8/5}$ = 5 s and 10 s. The hardness corresponding to the 1350 °C peak temperature decreases with decreasing cooling rate (increasing $t_{8/5}$) from 310 to 255 HV10 at $t_{8/5}$= 5 s and 20 s, respectively. Furthermore, the softened zone exists outside the peak temperature zone in the IC/SCHAZ, having the minimum hardness of 255-270 HV, i.e. about the same as the hardness of the CGHAZ at $t_{8/5}$ =15 s and 20 s.

- M. Gáspár [109]: studied the effect of welding heat input on simulated HAZ of 15 mm S960QL steel. CGHAZ, ICHAZ and ICCGHAZ zones were simulated for $t_{8/5}$ = 2.5, 5, 10, 15, 22.5, 30, 100 s. Significant toughness reduction was observed in the investigated subzones in the whole cooling time range of the most common arc welding processes $t_{8/5}$ = 2.5–30 s. In CGHAZ generally hardening was observed, except in case of $t_{8/5}$ = 100 s where softening was identified in CGHAZ.
- M. Mičian, J. Winczek, D. Harmaniak et al. [110]: analysed the physical simulation of HAZ in 2 mm thick steel S960MC. Samples were simulated at different peak temperature i.e. 550 (SCHAZ), 600 (SCHAZ), 650 (SCHAZ), 800 (ICHAZ), 1000 (FGHAZ), 1200 (CGHAZ), 1350 °C (CGHAZ) and the corresponding microhardness are 320, 285, 287, 251, 292, 260, 248 HV1 respectively. The BM hardness was 361 HV1. The $t_{8/5}$ cooling time are 15.8, 19.1, 25.8 and 26.5 for 800, 1000, 1200, 1350 °C respectively. It was observed that microhardness decreased with increasing maximum temperature of the thermal cycle, largest decrease was observed at a temperature of 800 °C (251 HV1) while at 1000 °C, the microhardness increased again and reached a value of approx. 292 HV1. This is due to the favourable fine-grained structure of the FGHAZ zone. The lowest values of microhardness were obtained in at 1350 °C and 800 °C, where only 69% of the base metal hardness was recorded. This decrease in hardness corresponds to the changes in strength. Decrease of strength-related properties is a typical behaviour for all high-strength steels (i.e., quenched+tempered and TMCP steels), when they are heated in the range of 450 °C to A_{c1} temperature, due to martensite tempering.

2.4.2. Recommendation to the aims

- Physical simulation provides the facility for the generation of large volume material with uniform microstructure and properties which represent the one particular point within the HAZ;
- Hardening and softening behaviour of the HSSs in the HAZ depends on the grade, the value of $t_{8/5}$ cooling time and the peak temperature;
- To analyse the microstructural behaviour of HSSs, in the 5-30 s cooling time interval;
- The HAZ simulation of beam technologies in plates and sheets are also possible by Gleeble.

2.5. Residual stress

Residual stress (RS) occurs in almost every component obtained by different manufacturing processes like welding, forming etc. It is sometimes overlooked and ignored as felt that it has no significance effect without any external loading. But this negligence leads to the compromise with the quality and further it has profound influence on the material strength, fatigue life and dimensional stability. The different mechanism involved in the creation of the RSs such as non-

DOI: 10.14750/ME.2021.051

uniform plastic deformation, surface modification and material phase or density changes due to presence of large thermal gradients [111]. RSs in any components or body are those which occurs due to inequilibrium between the body and its environment. It is categorised by cause like thermal or elastic inequilibrium, according to method by which it is measured, or by the scale over which it self-equilibrate. According to the basis of the length scale over which it self-equilibrate, it is divided into three types; firstly, Type I which are macro "residual stresses" that appears in manufactured components. Secondly, Type II which are micro stresses that extend over the distances in the micron ranges e.g., between grains in metals. Finally, Type III are residual stresses that occurs at the atomic scale dislocations and crystal interfaces [28][111].

In welds, solidification and differential shrinkage causes large tensile and compressive residual stresses. The weld bead is stress-free while it is molten but residual stresses only creates after solidification. The hot weld seam and HAZ cool over a larger temperature range than the surrounding material and therefore shrinks more. In order to maintain dimensional continuity through compatible longitudinal strains, large longitudinal tensile residual stresses (TRS) are created in the weld metal and HAZ balanced by compressive stresses in the surrounding material [111]. The typical patterns of residual stress distributions in a butt-welded joint with longitudinal residual stress σ_x and transverse stress σ_y along the weld line and in the transverse section, respectively, shown in Fig. 2.9. The maximum magnitude of longitudinal stress is approximately equal to the yield stress.

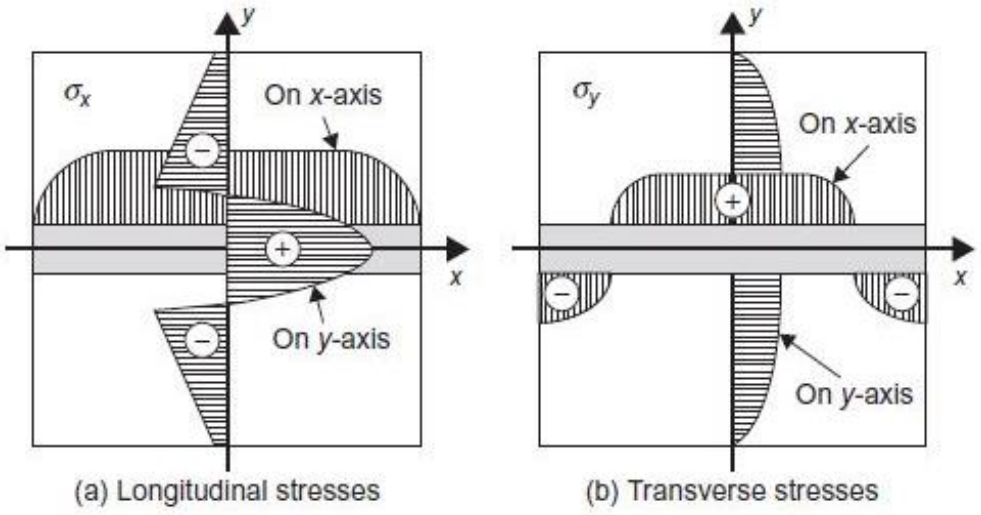

Fig. 2.9.Patterns of residual stress distributions in a butt-welded joint [112].

There are various techniques are available to quantify residual stresses in the specimens and the components. They are categorised into two parts, on is destructive methods and another non-destructive methods. Non-destructive methods include neutron and X-ray diffraction (XRD), where the atomic spacing of the material is used as a strain gauge. Destructive techniques include hole drilling, slitting and the contour method. In such methods RSs are inferred from distortions or relaxed strains caused by stress redistribution following cutting of the sample. However, each methods has its own significance, applications areas and limitation such as number of stress components that can be evaluated varies between the technique, limitation of the size of the samples, spatial resolution of the measurement of the area for each method etc.

DOI: 10.14750/ME.2021.051

[113]. However, the various residual stress measurement methods are so well developed and technologically sound that the accuracy gap between them is often not so large.

In this dissertation, one of the non-destructive method i.e. XRD technique was used for residual stress measurement. In this method, the XRD only penetrates a few microns. This methods use the ability of electromagnetic radiation to measure the distance between atomic planes in crystalline or polycrystalline, materials. This methods effectively measure a crystal inter-planar dimension that can be related to the magnitude and direction of the stress state existing within the material. These measurements are independent of whether that stress is residual or applied. Also, the measured lattice strains are “absolute” quantities, that is, relative to a zero-strain datum. This is a significant feature of diffraction methods because it allows residual stresses to be measured as well as applied stresses [111].

The risk of cracking during welding of HSS is higher compared to MS due to the high RS and the more sensitivity to hardening. GMAW is most commonly used method for welding process of these HSSs, but the arc welding severely affects the RS because of high linear heat input which in turn gives wider weld and HAZ. But the EBW is a high energy density fusion beam welding process that can be more advantageous due to smaller linear heat input in the weld, the RS reduces substantially, also providing the narrow weld and HAZ without significantly affecting strength properties of the weld [114][115]. RS can be more troublesome because it generates the stress concentration at joints and the possible chances of deleterious microstructures in the HAZ [27]. The calculation and evaluation of the RS is highly difficult task in the welded specimen specially in the high energy beam welded samples due to its narrow weld and HAZ. During welding localised heating and cooling occurs which set up large stresses in the vicinity of welded joints [28][29]. The RS develop in the welded specimen is a complex combination of various factors like geometrical features of the weld, welding parameters, stiffness of the structure, manufacturing process, environment and volumetric changes due to phase transformations in the weld zone etc. [31][32][33][34]. The effects of the RS may lead to the structural failure, so the proper analysis of these stresses is detrimental. TRS in the welded joints can cause higher mean combined applied stresses which negatively affect the fatigue life of the joint. The compressive residual stresses (CRS) considered beneficial as it reduces the mean compressive residual stresses (mCRS) which significantly improve the fatigue life of the welded joint, reduces the stress corrosion cracking (SCC) and brittle fracture. These beneficial effects of the compressive stresses are highly recognizable in the industry [115][116][117][118]. Furthermore, the one of the important critical zones in the welded joint area which draw most significant attention is the weld toe where typically highest tensile stresses are located caused by the higher stress concentration and hardness. The basic assumption is often made that the magnitude of the maximum tensile residual stress in a weld in the as welded condition is equal to the yield strength of the weld or BM [116].

Various researchers in past had studied material characterization and mechanical properties of Q+T and TMCP steels with conventional GMAW process while the effect of EBW on the residual stress distribution of HSS is rarely available. Thus, it is worth to examine and compare for induced residual stresses in these HSSs during the application of beam process welding technology [27][119].

DOI: 10.14750/ME.2021.051

2.5.1. Case studies of residual stresses

- L. Suominen, M. Khurshid, J. Parantainen [34] studied residual stresses in welded components of different high strength steels (S960QL, S690QL, S700MC, S420MC) and their modifications for improving the fatigue strength. Since, in HSS, welded structure looses the original strength and the weld toe is more critical area as it increases the notch effect and high tensile stresses. For S960QL and S690QL, thickness= 10 mm, XRD method used, Collimator size was 2 mm. S960QL, residual stress (at weld toe)= 100 MPa; S690QL, residual stress (at weld toe)= 150 MPa.
- T. Slęzak, L. Śnieżek [120] observed that in the steel with high yield strength, their fatigue strength was influenced due to their stress concentration, local changes of stress or microstructural changes in HAZ. So, to improve the fatigue behavior of HSS steels they used high energy joining technology i.e. LBW, since it gives relatively narrow welds and reduced HAZ which minimised the residual stresses and distortions. S960QL material with 6 mm thickness was investigated with XRD method. In HAZ, with the increase of welding speed residual stresses increases in the direction perpendicular to the weld axis and the maximum tensile stress was 350 MPa.
- T. Schaupp, D. Schroepfer, A. Kromm and T. Kannengiesser [121][122] studied the residual stress distribution of Q+T and TMCP high strength steel TIG welded joints. Materials used are S960QL and S960MC, thickness = 8 mm. XRD method was used for residual stress measurement and the collimator size was 2 mm. With the increase of heat input, transverse residual stress for TMCP is higher in the weld than Q+T whereas for the Q+T steel the tensile stresses in the HAZ increase with increasing heat input.
- D. Schroepfer, A. Kromm, T. Schaupp & T. Kannengiesser [123] analysed the cooling conditions and resulting microstructure for varied heat control parameters on multi-layered GMAW welded high strength steel joint. The welding stresses may be detrimental for the safety and performance of high-strength steel component welds during fabrication and service, especially due to the high yield strength/ultimate tensile strength ratio. So, they analysed the local stresses in the weld while welding and cooling under component relevant shrinkage restraints. Material used S960QL, plate thickness = 8 mm to 20 mm, GMAW welding process, matching filler materials. If the desired cooling time ($t_{8/5}$ = 6 to 8 s) was applied then a high heat input and low interpass temperature causes significantly lower tensile residual stresses in the critical HAZ compared to low heat input and high interpass temperature.
- J. Hensel, T. Nitschke-Pagel & K. Dilger [124] presented the results from experimental investigation on welding residual stress generation with single and multi-layered fillet weld. Material used S355N, S690Q, S960Q, plate thickness = 10 mm, robot-mounted GMAW. XRD method was used for RS measurement. With setup of longitudinal stiffeners with single-layer fillet welds, higher strength steels (S690Q and S960Q) showed lower residual stresses with magnitudes of approximately 40% of the nominal yield strength. Residual stresses at the weld toe were smaller than the maxima determined and varied between -80 MPa (compression) and 200 MPa (tension). While with multilayer fillet welds setup, the residual stress profile from the investigated S960QL varied from the results of the single-layer welds. RS was nearly 0 MPa at the weld toe and decreased slightly with increasing distance to the weld toe (−100 MPa).

DOI: 10.14750/ME.2021.051

– T. Nitschke-Pagel [125] studied the measurement of RS in welded joints using XRD method. S460N material, thickness= 6 mm, collimator= Ø1.0 mm, TIG (E= 1092 J/mm) and GMA-welded with filler material X90 (E= 762 J/mm) butt joint. Author presented the influence of the local resolution on the quality of the measurement results using collimator size Ø0.5, Ø0.8, Ø1.0, Ø1.5, Ø2.2 & Ø3.0 mm. The final results are independent from the collimator size except for the Ø0.5 & Ø0.8. With experiences of practical application of XRD revealed that collimator size lower than Ø1 mm leads to higher scattering and large extensions of the required exposure times. In practical, local resolution of 1 to 2 mm are most commonly used especially for standard arc welds, however in very narrow beam welds lower local resolution can be used.

2.5.2. Recommendation to the aims

– Residual stress measurement for high strength structural steels (e.g. S960QL, S960M etc.) and automotive steels (e.g. DP1000 etc.) should be examined;
– RS measurement results by means of X-ray diffraction method can be expected more reliable.
– With application of modern material joining process like EBW, LBW process has outstanding significance in the reduction of residual stresses compared to GMAW and thus the fatigue behaviour of the high strength structural steels.
– With EB welded joint lower angular deformation can be realised compared to the GMA welded joint.
– In literature, Ø2.0 collimator size was frequently used for XRD measurements of arc welded joints, however for narrow beam welds lower collimator size should be used (Ø1.2 mm or Ø1 mm if possible).

2.6. Fatigue behaviour of HSS and their welded joints

In this chapter, keeping in mind the objectives of the dissertation, I have provided a brief insight into the (primarily) the main features of fatigue crack grow (FCG) and the behaviour of HSS welded joints under cycle conditions.

2.6.1. Fatigue crack growth (FCG) and characteristics

In the case of cyclic stress structures, especially welded structures, the frequency of fatigue fracture exceeds the static fracture, however, classical measuring approach and inspection methods based on the Wöhler curve do not seek to follow the damage, failure process, but allow for allowable stresses. These tensions belong to some kind of fracture (survival) probability, so they reflect some kind of risk taking. However, they are not suitable for taking into account deviations/defects in the structure due to production or operation. For a wide variety of structures, this has justified the onset of the fracture mechanics approach [126].

In the case of fatigue design, it is assumed that, for a certain service life the structure as a whole or some of its components are free from defects and, even if they contain defect(s), no cracking will occur at the applied stress level. In contrast, damage-proof design is based on the presence of cracks in each structure, and these cracks increase. According to this principle, the structure must bear the load until the fault is discovered, more precisely until the fate of the fault is decided [127]. The prominence of defect-proof design philosophy is justified by the fact that

DOI: 10.14750/ME.2021.051

the concept of design for a certain lifetime has often proved insufficient, as evidenced by the unfortunate damage that has occurred in practice, moreover, the production of welded structures without gaps in continuity can in practice only be guaranteed in principle [128]. As an economic disagreement, it can be argued that a significant unused service life can be lost if a structural component is replaced when the maximum design life is reached [129].

One of the cornerstones of the lifetime estimation system [130] is the range of fracture mechanical measures representing the material. For welded structures, especially those made of high-strength materials, the theory of linear elastic fracture mechanics (LEFM) can be used to assess the hazard of cracks, where the stress intensity range (ΔK) in the vicinity of the crack peak is used to describe the stress state. Accordingly, the required material measures can be derived from the fatigue crack propagation kinetic diagram, which can be determined from the results of fatigue crack propagation rate studies.

Several models are known to describe fatigue crack propagation. The general form of the most commonly used relationship based on the range of the stress intensity factor is as follows:

$$\frac{da}{dN} = C_n f\left(\Delta K\right)^n \qquad 2.2$$

Plotting the relationship (2.6) - in the case of constant load asymmetry factor (R) and constant temperature (T) - in a double logarithmic system, we obtain the characteristic curve, the kinetic diagram of fatigue crack propagation as shown in Fig. 2.10,

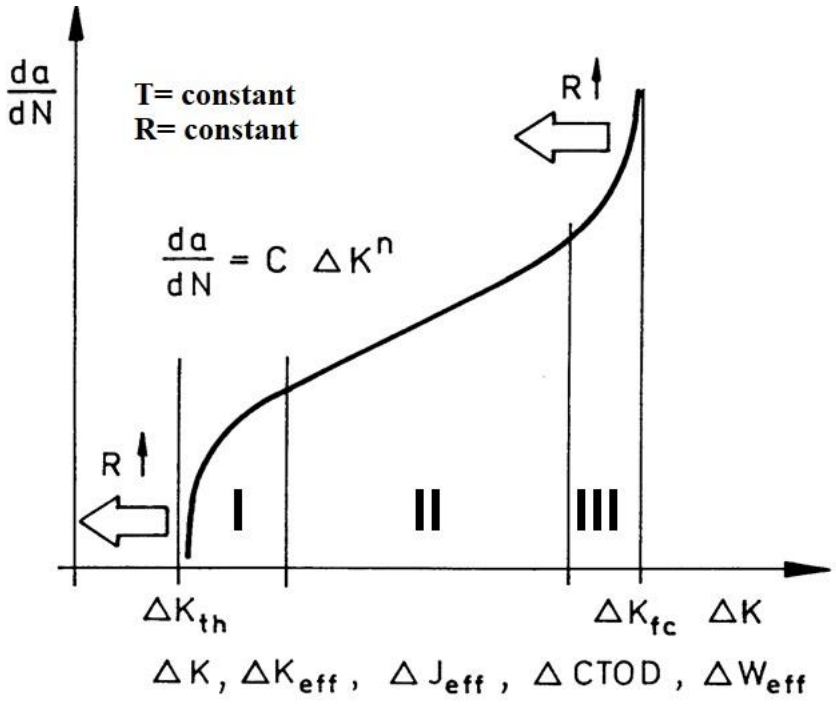

Fig. 2.10. Kinetic diagram of fatigue crack growth (FCG) [126][131][132].

According to LEFM and stress intensity factor (K) theory, the regions of the diagram can be described on different ways. Region I, is a phase of slow propagation of the crack. Its left tangent is the threshold of the stress intensity factor range (ΔK_{th}), during which the crack is not yet

DOI: 10.14750/ME.2021.051

spreadable. Region II, is range of stable crack growth, and the region III is the rapidly accelerating range of crack propagation. The right-hand tangent of the latter is the critical value in the range of the stress intensity factor or the cyclic fracture toughness (ΔK_{fc}) [133]. These equations are as follows, respectively.

In the first two regions (I and II) the Klesnil-Lukas equation [134], can be used reliably in range. It is the most widely known and used equation.

$$\frac{da}{dN} = C_m \left(\Delta K^m - \Delta K_{th}{}^m \right) \qquad 2.3$$

in the middle part the Paris-Erdogan law [135] is valid,

$$\frac{da}{dN} = C \left(\Delta K \right)^n \qquad 2.4$$

and finally, in the second and third regions the Forman's function [136] are the most common used formula

$$\frac{da}{dN} = \frac{C_p \Delta K^p}{\left(1-R\right) K_c - \Delta K}. \qquad 2.5$$

In fatigue crack growth tests, the propagating crack size (a) shall be measured, the number of stress cycles (N) shall be counted, and then the fatigue crack propagation rate (da/ dN) shall be calculated. Having this, the kinetic diagram of the fatigue crack propagation or usually a part of it (da/dN -ΔK) can be given with the help of the stress intensity factor range (ΔK), and then the material measurements can be calculated.
Correlation for calculating the range of the stress intensity factor

$$\Delta K = \frac{\Delta F}{B\sqrt{W}} Y \left(\frac{a}{W} \right) \qquad 2.6$$

shape, in which the Y (a/W) functions depend on the type of specimen, can be found in manuals, standards, and test control software descriptions.

Beside these formulae further and more complicate possibilities are found in different sources [137][138]. From an engineering point of view, the Paris-Erdogan law and its modified versions are the most common used equations.

2.6.2. Case studies

– J. Lukács & Á. Dobosy [139] studied the influence of the mismatch effect on high-strength steels and to determine fatigue crack propagation design curves. Material used S690QL, S960QL & S960M, thickness 15 & 30 mm. GMAW, matching, overmatching (OM) and undermatching filler materials. Shielding gas: 82% Ar + 18% CO_2. The average values of the Paris-Erdogan exponents (n) of the matching (M), overmatching (OM) and undermatching

DOI: 10.14750/ME.2021.051

(UM) conditions of the investigated welded joints were statistically higher than the exponents of the concerning base materials.

- M. Gáspár [14] studied the FCG for the S960QL, thickness= 20 mm, GMAW, filler material-X96, matching type, pre-heating temperature= 200 °C, interpass temperature= 150 °C, shielding gas: 82% Ar + 18% CO_2, crack propagation monitored optically, stress ratio, R= 0.1, sinusoidal loading wave form. The specimens were machined from the welded joint in the two directions studied (21W and 23W), the difference did not prove to be significant, similar to the base material. The kinetic diagrams show that in the case of specimens incised in the weld, the propagation of cracks started at a relatively high rate. When these cracks reach a size of a few millimeters, the initial differences are evened out. This can be explained by the fact that due to the multi-layered weld joint, the inner layers of the weld undergo tempering. Based on the results of the tests, the resistance of the weld and the heat-affected zone to fatigue crack propagation lagged behind that of the base material.
- H.F.H.Mobark [50] studied the FCG for the Weldox 700E & Alform 960M, thickness= 15 mm, GMAW, R= 0.1, sinusoidal loading wave form, crack propagation monitored optically, loading frequency was f = 20 Hz for two-thirds of the growing crack's length, approximately, and it was f = 5 Hz for the last third. The average values of the Paris-Erdogan exponents (n) of Weldox 700E and Alform 960M base materials in the T-L directions and of the Weldox 960Q base material in the T-S directions are significantly not different, which means equal fatigue crack growth resistance in these orientations. The average value of the Paris-Erdogan exponent (n) of the matching (M) welded joint of Alform 960M is lower than exponent of the undermatching (UM) condition. The fatigue crack growth resistance in matching (M) condition is lower than undermatching (UM) condition.
- H.T.Li & X.D.Song [140] studied the fatigue crack propagation rate of high strength steels welded joints. Material: HG785D (Q+T), thickness= 20 mm, MAG, shielding gas: 80% Ar + 20% CO_2, matching, no preheating, R= 0.2, f= 8 Hz. The a-N curve and fatigue crack growth rate da/dN-ΔK curve were plotted. The linear correlation coefficient of experimental data for HAZ was higher than the weld. The fatigue crack propagation rate of the weld and the HAZ of the butt welded joint is different at the same stress ratio, fatigue crack propagation rate in HAZ is higher than in the weld.

2.6.3. Recommendations to the aims

- Selection of adequate number of specimen should be strictly planned for investigation;
- Statistical analysis technique should be used to evaluate and draw accurate inference of the tested results;
- The testing circumstances should be properly presented and observed while considering various influencing factors;
- High energy beam welded joint of HSS without filler material should be investigated by fatigue crack growth tests and compared with similar strength grade of HSS with arc welding process for different mismatch phenomena;
- The resistance to fatigue crack propagation of electron beam welded joint should be studied carefully, may be in future it has high industrial applicability ranging from structural components to automotive applications.

DOI: 10.14750/ME.2021.051

3. APPLICATION OF BEAM WELDING TECHNOLOGIES ON HSS

3.1. Laser beam welding

With the development of HSS, role of welding technology growing significantly to improve the weldability of these materials to perform intended function at the highest level [141]. In the industry there is a very rapid increase in the application of LBW process for HSS welding which radically different from the conventional welding processes [142]. HSSs and LBW are like two side of a coin, without each other they are incomplete and these combinations becoming so popular nowadays in all industrial application with using all newer laser processes or technology in the field of welding technology.

3.1.1. Diode laser

The laser was first invented in 1960 and then used extensively in materials processing. Laser welding constitutes a large area of laser materials processing market i.e. about 40% [143]. A HeNe laser or a laser diode, both low-power lasers that radiate in the visible spectrum, are switched into the beam path when equipping a laser machine. However, the laser beams used in materials processing radiate in the infrared and ultraviolet ranges, so that they are not visible [144]. The spectral ranges of light and different lasers are shown in Fig. 3.1.

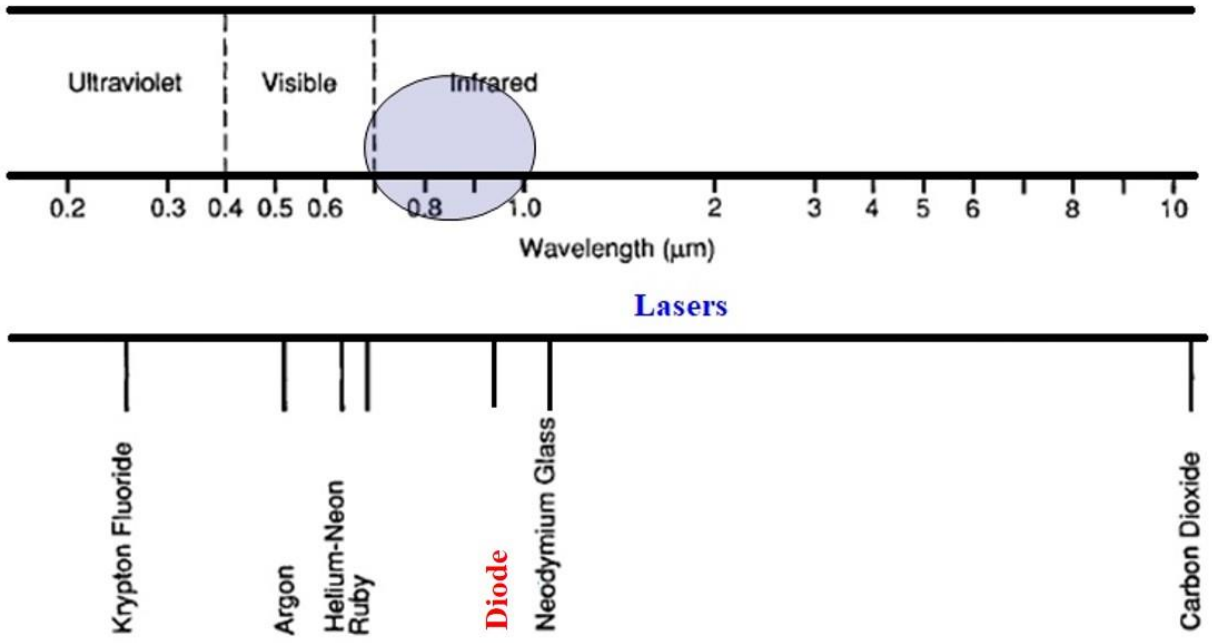

Fig. 3.1. The spectral ranges of light and different lasers [144]

DOI: 10.14750/ME.2021.051

The power density in laser welding process is on the order of up to 10^8 W/cm^2, which is about 4 times higher magnitude than in conventional arc welding methods [145]. Therefore, the influence of LBW on the base metal in the vicinity of the weld (HAZ) is considerably lower and the microstructure degradation is minimal [145]. There are different types of laser developed over the time and it is widely used in material processing and welding technology like carbon dioxide (CO_2) laser, neodymium-doped yttrium aluminum garnet (Nd YAG) laser, diode laser, disk laser, fiber laser etc.

HPDL welding is considered as boon and state-of-the-art technology in modern automotive industrial application. The advanced feature of HPDL, crucial in the welding process is the inherent beam stability, adjustable square or rectangular shape of the laser beam spot with a top hat profile in one direction and a Gaussian like in the other leads to uniform heating of the surface over a relatively large area [146][147], high energy conversion efficiency of 30-50% and relatively high radiation absorption rate on the surface of most metals due to its shorter wavelength lies near infrared range from 0.808 to 0.960 μm [26][148][149][150]. The HPDL with its application does not only provide an ideal beam geometry and intensity distribution but is also an efficient way for heat treatment processes, including PWHT [151]. The most important process parameters in the heat treatment of material by diode laser welding are laser power and traverse speed [21][152]. By PWHT the fatigue life, the lifetime of the joints, the crack resistance and other mechanical properties (e.g. toughness) may get improved significantly. So, it is very crucial to evaluate the laser weldability of HSS, including microstructural changes in weld and HAZ and to analyse the applicability of laser PWHT [5][153][154][155]. The increased beam quality, lifetime and further reduced investment cost as compared to other laser, this laser look into a bright future with a vast increase of market share [156][157][158][159]. Diode lasers achieve particularly excellent smooth seams with low spatter specially at high welding speeds in conduction mode welding of thinner sheets but also in deep penetration/key-hole welding. Due to the short wavelengths near the absorption maximum of aluminium, this method is widely used in the automotive industry where high-power diode laser systems are used for body-in-white applications [160].

The significant advantage of the actual HPDLs themselves is their considerably low price (200–400,000 euros), and the very high radiation absorption rate which for metals from an iron matrix is 20–40%, at a laser beam wavelength of 940 nm. The laser light beam absorption rate also depends on the temperature of the treated metal and increases to approximately 90% after exceeding the melting point, while after exceeding evaporation temperature, almost all laser radiation energy is absorbed. Laser radiation absorption also depends on the beam's power density. At the point of exceeding the beam's power density threshold, which for carbon, alloy and highly alloy steel is approximately 1.5 x 10^3 W/mm^2, the absorption ratio is approximately 90%, regardless of the laser radiation wavelength [26].

LBW has some other distinctive qualities which make it especially suitable to the requirements of the automotive industries. These characterestics are as follows [161][162][163][164]:

- High welding speed: a high production rate is a main requirement in the automotive industry. LBW may reach higher welding speeds of several meters per minute, allowing a large number of welds in a short time.

DOI: 10.14750/ME.2021.051

- High quality of the welded parts: because of the highly concentrated energy of the laser beam, very limited distortions of the final parts occur. The welded components do not need to be reworked after welding and are “ready to use.”
- Versatility in terms of weld geometry and accessibility: laser welding easily perform from a single side (tube, profile etc.), and many different weld shapes (C, S- shape etc.) can be made.
- Adaptation to mass production: laser welding is highly repeatable and with proper automation result will be highly effective and productive.
- Highly accurate and efficient process.
- Narrow HAZ and FZ.
- Low linear energy (heat input).
- Minimal welding deformations and stresses.
- Cost reduction.
- Higher improved productivity.

3.1.2. Post weld heat treatment

The main benefit of diode laser is to use same machine for welding and post weld heat treatment simultaneously. Also, diode laser beam welding process is considered as best method for post weld heat treatment as its cover larger surface due to large focus size which may be rectangular or square shape. In order to minimise the differences in microstructure and properties between weld bead and base metal, a PWHT is sometimes applied to the welds. This post treatment provokes a hardness decrease in the bead, associated with coarsening and it can also enhance precipitation hardening [165]. PWHT reduces residual stress levels and tempers, i.e. softens the hardened regions, particularly in the HAZ. It is performed to temper the weld metal and HAZ with the aim of decreasing hardness and improving toughness, and reducing the residual stresses associated with welding.

The typical cooling conditions in the HAZ correspond to the heating rates of several thousands and to the cooling rates of several hundreds of °C per second, which correlates with a typical characteristic $t_{8/5}$ cooling time of less than one second. This results in most cases in brittle martensitic weld metal and HAZ microstructures of steels, even for those which are typically considered to have good weldability properties. Even for steels with a reasonable amount of carbon at 0.18 wt%, this would result in hardness profile peaks of above 400 HV. This is the reason why preheating or post-weld heat treatment might be necessary to reduce the HAZ hardness values for some steel grades [166].

After PWHT, a weldment should be tougher and also should resist such service hazards as SCC and in-service cold cracking more readily than in the as-welded condition. The selection of PWHT temperatures is often aided or limited by the appropriate application standard, and is usually within the temperature range 550–750 °C. It should be remembered that PWHT at a lower temperature will not undo any excessive softening which may have resulted from the use of too high temperature. However, if a weldment has been undertempered by PWHT, a further heat treatment at a higher temperature is always possible [150].

Heat treatment with diode lasers does not only allow hardening but also the exact opposite, namely, the tempering of steels. Diode laser is the better tool compared to other methods like induction, gas flames or infrared rays. On the one hand, material processing is highly flexible and precise, even with hardening; on the other hand, the created transition zone between the

DOI: 10.14750/ME.2021.051

processed and unprocessed base material is smaller than that created with other technologies. But in particular, diode lasers have a very homogeneous intensity distribution even at big spots, which makes the softening results specifically even [167]. Laser heat treatment is also used to prepare high-strength materials for subsequent forming by reducing the hardness in well-defined areas [160].

3.2. Electron beam welding

EBW was invented as innovative welding technological process with significant breakthrough in the development of electron beam is a unique as a processing heat source by virtue of it focusing ability, intensity and high vacuum operation which in turn provides the greater penetration depth and narrow FZ is of particular importance [168][169]. These combined characteristics of the EBW processes completely distinguishes it from other conventional arc, resistance welding processes [170]. It is fusion welding process in which high energy density beam (10^7 W/cm^2) [8][171] is impinging on materials surface to be welded and vaporises metals (kinetic energy of high velocity of electron used to produce heat energy) [60][172]. Firstly, it was intended to use in nuclear and aerospace industries but with the subsequent development in the technology (process and equipment) broaden the dimension of application area of EBW [171][173]. Nowadays, it is widely used in welding and material processing like in construction area, ship building, petrochemistry, medical equipment etc. [174]. The outstanding combination of EBW process and HSS Q+T and TMCP with a ground-breaking result pioneering in the field of different industrial sectors like automotive and vehicle industry (crane, truck etc.) [175].

During the conventional arc welding of HSSs the outstanding toughness of the base material is drastically reduced in the HAZ and occasionally in the weld due to the welding heat input [109], therefore EBW can mean an ultimate way for the reduction of the areas of the brittle HAZ subzones.

Some advantages of the electron beam welding process are presented below which has significant importance in the application of materials with strategic applications [8][170][171][176][177][178]:

- Its gaining the attention for the application to HSSs since in these steels complete elimination of hydrogen is the prime requirement for successful welds.
- It is one of the safest welding process against the weld contamination (e.g. oxygen, nitrogen etc.).
- EBW process getting more serious attention for many critical joining applications (bridges, aircraft parts, medical equipments, oil and gas industry, nuclear industry etc.) in which the refining and high intensity inherent to the process that can offer any advantages.
- Wider range of material thicknesses can be weld without filler materials and shielding gas.
- High depth-to-width weld ratio can be produced. This chacterestics allows for the single pass welding of the thicker section joints.
- Higher power beam density and lower linear heat input resulting in the reduction of HAZ and FZ width while keeping the welded joint strength and toughness intact.
- Faster welding speed possible due to higher melting rates.
- Various types of joints (e.g. butt, lap, edges, T-joints) can be easily welded by EBW process.
- High precision process.

DOI: 10.14750/ME.2021.051

3.3. Case studies on beam technology application to the HSS

LBW:

- P.H.O.M Alves et al.[21] studied microstructural characterisation and mechanical behaviour of the laser welded DP1000 HSS with combination of various laser power and welding speed combination. Plate thickness = 1.8 mm, Yb-fiber laser system, argon gas flow rate was 6.6 l/min. They observed that the retained austenite and tempering of prior martensite are responsible for the softening experienced between intercritical and subcritical HAZs. Size and volume fraction of retained austenite increase from the FZ towards the HAZ.
- K. Bandyopadhyay et al. [22][23] studied the optimization of the welding parameters to minimize localized softening in the HAZ of DP980 steel. Laser power of 1.8 kW and welding speed 1 m/min was used. Transverse tensile testing of DP980 laser welded blank (LWBs) showed fracture at the outer HAZ and hence, severe reduction in strength and ductility was observed. Microhardness profile showed reduction in hardness at outer HAZ compared to that of base metal.
- E. Biro et al. [24] examined the chemistry and microstructure of DP600 and DP780 steel grades affect martensite tempering kinetics during laser welding. They used 4-kW diode laser and 8-kW CO_2 laser in case of DP600 and 1-kW Yb fiber laser in case of DP780. For all experimental welds, the minimum weld hardness was found to be significantly less than the base material hardness. The analysis of the softened HAZ revealed that the martensite within the base material structure decomposed to cementite and ferrite (tempering).
- J. Wang et al. [25] studied the effect of energy input on the microstructure and properties of laser welded DP1000 butt welded joint with thickness of 1.5 mm. Nd:YAG laser with power of 1.3 kW, welding speed from 4 mm/s to 14 mm/s, gas flow rate = 20 l/min, pure argon gas was used. Softening existed in the SCHAZ and ICHAZs. The average hardness of the softening zone was only 75% of that of the base metal. The hardness of the hardening zone of the HAZ was 125% of that of the basemetal. The most serious softening zone was near Ac_1; the hardness in the softening zone increased as the distance from Ac_1 towards base metal increased until the hardness of the base metal was reached. Tempering martensite was found in the SC zone in the HAZ of the DP1000 steel laser welding. In the ICHAZ, a part of the austenite was transformed into ferrite/bainite and M–A instead of martensite during the welding process; thus, there was less martensite in this zone than in the base metal. As a result, the hardness of this zone decreased considerably, leading to the formation of a softening zone.
- L. Prém et al. [179] studied the effect of resistance spot-welding technology made of DP steel. Material used-DP1000, thickness=1 mm. The traditional continuous energy input and the symmetric double pulse as the non-continuous energy input was compared during the experiments. They observed critical hardening in weld and HAZ during resistance spot welding. The micro indentation hardness profiles (measured and simulated) of welded DP1000 steel joints showed significantly higher hardness values, approximately 1.5 times higher than that in the base metal were observed in FZ zone. The profile was relatively flat across the fusion zone with an average FZ hardness of 490HV. In the ICHAZ of joints near the fusion boundary also exhibited high hardness.
- Z.Wan et al. [180] studied the hardness evolution and high temperature mechanical properties of laser welded DP980 steel joints with thickness 1.2 mm. Fiber laser with a peak power of 6

DOI: 10.14750/ME.2021.051

kW was used for butt joint. No shielding gas, P= 4 kW, s= 16 m/min, beam size=0.6 mm was used. Microhardness evolution analysis (HV0.3) across the joint showed different subzones hardness and BM. BM= 320, FZ= 379, CGHAZ= 394, FGHAZ= 428, ICHAZ= 321, SCHAZ= 289. The above results shows the hardness of the FZ was higher to the BM which resulted from high cooling rate during LBW. The hardness in the HAZ varies significantly and hardening was observed in the CGHAZ and FGHAZ. FGHAZ attributed to the highest hardness and CGHAZ second highest. There was sharp drop in the hardness from FGHAZ to the SCHAZ because the HAZ experiencing a temperature between A_{c1} and A_{c3}, causing incomplete quenching.

EBW:

- S.Błacha et al. [1] in his study related to the EB welded joint of S960QL for thickness 11 mm, observed that the tensile strength of the welded joint are at same level of the BM with parameters (accelerating voltage = 120 kV, beam current = 29, 30, 31, 32 & 33 mA, welding speed = 800 mm/min). The cooling rate of HAZ is less than 2 s (time $t_{8/5}$). The maximum macro hardness was found in the HAZ. The microstructure of the HAZ depends on the distance from the fusion line and consists of martensite near the fusion line and bainite in the vicinity of the base material. The different sub zones could be distinguished clearly due to differences in morphology and level of hardness. The welding of HSS S960QL can be performed satisfactorily using the EB-welding process without compromising the mechanical properties of the weld.
- S.Błacha et al. [60] showed in his study the results of metallographic examination and mechanical properties of electron beam welded joint of quenched and tempered steel grade S690QL and compared with MAG welded joint of same material. Plate thickness = 10 mm, accelerating voltage = 150 kV, beam current = 3, 5, 10, 12 16, 18 & 20 mA, welding speed = 500 mm/min. The linear energy of 280 J/mm was selected as the most appropriate for the welding. For the comparison purposes the traditional metal active gas (MAG) welding of the same steel (S690QL) pieces was also performed. The welding parameters in this case were: welding speed 350 mm/min and the linear energy 1020 J/mm. It was shown that, for MAG welds, the best mechanical properties were achieved when cooling time was in the range 6-10 s for at the lowest possible linear energy (500-700 J/mm). The base material as a delivered condition (quenched and tempered) had a bainitic-martensitic microstructure at hardness about 290 HV0.5. After welding, the HAZ microstructure is composed mainly of martensite (in the vicinity of the fusion line) of hardness 420 HV0.5. The weld made by EBW is 6 times narrower than the joint produced by MAG; the HAZ width is also narrower. Also, the hardness values were lower than 450 HV10 – the permissible hardness level for qualifying welding technology according to the ISO 15614-11 specifications.
- G. Zhang et al [181] studies of EB welded joint of 300M (a commercial low alloy HSS, a modified AISI 4340 steel with silicon, vanadium and slightly higher level of carbon and molybdenum content than AISI 4340) composed of ferrite, bainite and retained austenite, HAZ is composed of ferrite and cementite, whereas this steel found extensive application in aerospace industry such as landing gear, high strength bolts and air- frame parts.
- W. Maurer et al [177] studied the influence of soft zone on the static tensile strength of EBW of a TMCP steel. Material= S700 MC, thickness= 6 mm, energy input= 71 to 1200 J/cm. With the comparison between low heat input and high heat input, HAZ does not show any decrease

DOI: 10.14750/ME.2021.051

in hardness while the hardness rises in the FZ as a result of low heat input and the resulting reduced cooling time. While with higher heat input, softening appears in the HAZ and the FZ. EBSD analysis confirms that the HAZ with low heat input has smaller grain size than the higher energy input. In samples with low heat input (cooling time), fracture took place in the BM while with the higher heat input, it occurred in the weld metal due to softening of th HAZ and FZ.

- J. Górka et al. [182] in their study of EBW of TMCP steel S700 MC discussed the analysis of various mechanical testing of welded joint. Material= S700 MC, thickness= 10 mm, butt joint, A_v= 120 kV, I_b= 28.5 mA, s= 800 mm/min, E= 260 J/mm. The tensile strength of the welded joint (830 MPa) exceeded that of the BM (700 MPa) (fractured occurred in the BM). Bend test of the butt welded joint was characterised by good plastic properties (bend angle= 180°). BM structure typically constitutes fine-grained bainitic-ferritic structure. HAZ consists of bainitic structure whereas the weld constitutes mainly martensitic structure. The changes in the grain size in the HAZ were not significant which ascribed to the considerable heat input to the welded joint. In comparison to BM hardness (280 HV0.2), EBW process increased the hardness in the weld (331 HV0.2) and in HAZ (334 HV0.2). So, in weld and HAZ, hardness did not exceed the 350 HV, the limit value for the unalloyed steel containing microalloyed elements. The impact test revealed a decrease in toughness in the HAZ in comparison to the BM.

3.4. Recommendation to the aims

- LBW and EBW eliminates the use of special joint preparation, filler materials and reduces the thermal distortions;
- In LBW, hardening of DP steels are observed in supercritical HAZ i.e. CGHAZ and FGHAZ, while SCHAZ experiencing the softening, peak temperature below the A_{c1} line, martensite phase in the BM tempered, causing the decrease in hardness below the BM;
- Mismatch phenomenon should be investigated in terms of the autogeneous LBW and compared with LBW matched welds;
- LBW narrow welds dimension and properties of the neighbouring materials (BM), restricted the thinning of the hardened and softened areas, which ultimately reduces the detrimental effects in HAZ;
- PWHT leads to the mictrostructural change that justify the improvement in ductility and reduces the risk of brittle fracture and tensile residual stresses in the welded joint. Furthermore, PWHT can reduce the hardness peaks in HAZ subzones (CGHAZ, FGHAZ & ICHAZ) and thus the cold cracking sensitivity;
- EBW technology provides the deep penetration without filler in thicker plate thickness;
- Its outstanding features of minimal and localised heat input results in the narrow weld and HAZ resulting in lower residual stress and smaller distortion;
- EB technology eliminates the need of filler materials, especially in the higher strength categories;
- Beam technology provides the mechanical properties of the welded joint strength near base metal strength, although deeper investigation (instrumented impact testing, fatigue crack growth tests) and comparison of the properties with GMAW are rarely available in the literature.

DOI: 10.14750/ME.2021.051

4. SUMMARY, SPECIFIC AIMS OF THE RESEARCH WORK

The work presented in this dissertation focuses on the comprehensive and systematic study of the application of innovative welding processes (LBW and EBW) on the different grades of HSS and to analyse the microstructural changes and mechanical properties of the welded joints.

There is a growing tendency in the literature to the application of HSS and beam welding technologies. However, the different grades within the group of DP steels are presented in this dissertation have limited information for its behaviours (HAZ characterization, residual stresses, welding with matching filler metal) during LBW (especially diode laser beam welding) and PWHT. Based on the literature review it was observed that the HAZ of DP steel laser beam welded joint can significantly harden close to the fusion line, and tends to soften in ICHAZ/SCHAZ. Diode lasers are rarely used for the welding of high strength steels however its application growing nowadays, and it provide unique solution for the PWHT and welding by the same device. Before real experimental work it is recommended to investigate the HAZ characteristics of DP steels, although physical simulation-based HAZ characterization of these grades is rarely available in the literature. During LBW the analysis and the determination of thermal profiles and the $t_{8/5}$ cooling time are necessary to be explored by using various methods since beam technologies result significantly faster cooling of the weld and HAZ.

Regarding structural steels, very scarce literature is available dealing with the effect of EBW process on mechanical properties, residual stresses and fatigue resistance of the S960QL but almost no for S960M grade steel. However, in terms of the HAZ properties of high strength structural steels there is a widely available literature, including physical simulation experiments (partially at the Institute of Material Science and Technology) in a wide cooling time range. In this dissertation, the welding of HSS S960QL and S960M has been performed satisfactorily using the EB-welding process without compromising the mechanical properties of the weld. Based on real welding experiments and physical simulation analysis in the literature there is a significant reduction of toughness in the gas metal arc welded joints of high strength structural steels (S960M, and especially S960QL) in the whole $t_{8/5}$ cooling range [109]. In many cases the requirement for the impact energy (e.g. 27 J in -40 °C in case of S960QL) is fulfilled in the weld and the HAZ, although brittle behaviour is observed on the fracture surface [109][183]. However, the EBW can provide deep penetration weld with narrow HAZ, therefore the area of brittle subzones can be minimized. With the application of EBW, the joints can be prepared without the limitedly available filler materials, so it is a question whether an autogenous EB weld can be competitive with a matching alloyed weld of the conventional GMAW.

The specific aims of the research work are as follows:

- Determination and comparison of thermal cycle and $t_{8/5}$ cooling time during diode laser beam welding of dual phase steels using analytical method and thermocouple measurement.

DOI: 10.14750/ME.2021.051

- Analysis of hardening and softening behaviour in the relevant $t_{8/5}$ cooling time interval of the different HAZ subzones (CGHAZ, FGHAZ, ICHAZ, SCHAZ) of DP steels (4 different grades DP800, DP1000 DP1200 & DP1400) by thermophysical simulation using Gleeble 3500 simulator.
- Analysis of microstructural changes and mechanical properties of autogenous diode laser beam welded joints and the effect of post weld heat treatment on the different grades (DP800, DP1000, DP1200 & DP1400) of DP steels.
- To study the combined effect of diode laser beam welding process with matching filler material and PWHT on the microstructural characteristics, mechanical properties and residual stresses of DP1000 high strength steel welded joint.
- Comparative study of the microstructural and mechanical properties (especially toughness) of the electron beam and gas metal arc welded S960QL steels joint.
- Evaluation of microstructural and mechanical properties (especially toughness) of the electron beam welded S960M steels joint.
- Investigation of the residual stresses of EBW high strength steel welded joints (S960QL and S960M) with modern experimental non-destructive X-ray diffraction technique.
- Determination and analysis of the FCG characteristics of autogenous electron beam welded joints from S960QL and S960M, and comparison of the results with effect of the conventional GMAW technology.

DOI: 10.14750/ME.2021.051

5. PHYSICAL SIMULATION EXPERIMENTS ON DP STEELS

5.1. Experimental circumstances

5.1.1. Characteristics of the base materials

The chemical composition of different grades of dual phase (DP) steels, a product of SSAB used for physical simulation and LBW and the mechanical properties based on the materials certificates [CD, AA1] are provided in Table 5.1 and Table 5.2, respectively.

Table 5.1.The chemical composition of the base materials (weight%)

Material designation	**C**	**Si**	**Mn**	**P**	**S**	**Cr**	**Ni**	**Mo**
*DP 800	0.136	0.20	1.55	0.013	0.0030	0.03	0.04	0.00
*DP 1000	0.132	0.19	1.50	0.010	0.0030	0.03	0.03	0.00
*DP 1200	0.105	0.20	1.59	0.011	0.0030	0.03	0.03	0.00
**DP 1400	0.220	0.46	2.46	0.016	0.0030	0.03	0.12	0.00
Material designation	**V**	**Ti**	**Cu**	**Al**	**Nb**	**B**	**N**	**CE**
*DP 800	0.010	0.000	0.01	0.046	0.016	0.0003	0.003	0.41
*DP 1000	0.010	0.000	0.01	0.041	0.014	0.0002	0.004	0.39
*DP 1200	0.010	0.030	0.01	0.042	0.000	0.0022	0.005	0.38
**DP 1400	0.023	0.030	0.21	0.037	0.000	0.0000	0.000	0.69

*According to the material certificate [CD. AA1] provided by the supplier
**According to the tested results in the Chemical Institute of the University

Table 5.2. The mechanical properties of the examined base materials

Material designation	**$R_{p0.2}$ (MPa)**	**R_m (MPa)**	**A (%)**	**(HV10)**
*DP 800	585	871	15.5 (A_8)	270
*DP 1000	821	1074	9.5 (A_8)	329
*DP 1200	1108	1289	4.5 (A_8)	386
**DP 1400	1391	1496	4.5 (A_8)	470

*According to the material certificate [CD, AA1] provided by the supplier
**According to the tested results in the University laboratory

5.1.2. Physical simulation

In the present sub-chapter of the dissertation, a series of physical simulation experiments together with the related material tests were performed to explore in the details the HAZ properties of welded joints from DP steels, which information is limitedly available in the literature (mostly structural steels are investigated by Gleeble) The characteristics of the inhomogeneous HAZ was investigated in order to identify the critical subzones in terms of

DOI: 10.14750/ME.2021.051

hardness and microstructure and to see the tendencies based on the examined $t_{8/5}$ = 5-30 s cooling time interval (shorter cooling is not possible with acceptable reliability with sheet metal specimen configuration and air cooling). However, based on this range it can be estimated what happens during shorter cooling time of LBW in the different subzones.

When selecting the peak temperature of the HAZ to be tested, the aspect is guided by the production of the zone in the HAZ, based on which welding technology can be developed so that the entire HAZ meets its requirements at the local level. Based on literature examples [14][108][153][184] and preliminary experiments, I chose a value of 1350 °C for the physical simulation of the coarse-grained zone. Since, the nil-strength temperature, which is 1408 ºC for a low-alloyed carbon steel under test [12]. This is the temperature at which the material can no longer withstand any mechanical load, and consequently at this temperature the specimen would rupture in the test chamber due to the stress due to thermal expansion.

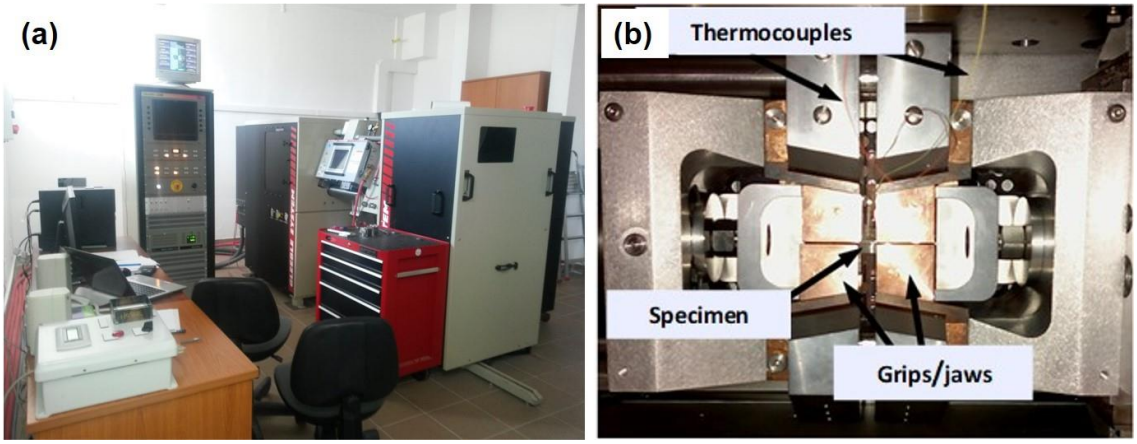

Fig. 5.1.Experimental setup of Gleeble 3500
(a) Gleeble 3500 physical simulator and (b) Specimen setup in the vacuum chamber

Based on the literatures [14][86][110][183] and the several preliminary experiments above Ac_3 temperature for FGHAZ, 950 °C was selected for physical simulation in this dissertation.

When selecting the peak temperature, it should also be taken into account that physical simulation tests are extremely sensitive to the condition of the jaws and the geometric accuracy of the specimens. There is always a risk that the simulated HAZ will not be homogeneous over the entire cross-section of the specimen. For the reasons listed, I chose a peak temperature of 775 ºC (safely above A_{c1}) for the physical simulation of the intercritical zone, which is supported not only by the data in the table but also by other physical simulation experiments on carbon steels [14][108][153] [184].

For SCHAZ, based on the literatures [86][110][183] and after several preliminary experiments with different temperatures [86] in this subzone, I chosen 650 °C for physical simulation because it is safer under A_1 temperature and it is also applicable as tempering temperature for high strength structural steel.

The DP steels (4 different grades: cold-rolled DP800, DP1000, DP1200 & DP1400) were physically simulated using Gleeble 3500 simulator (Fig. 5.1) to determine softening and hardening in heat affected zone. Sheet base specimens (1 × 10 × 70 mm) were prepared and subjected to thermal cycles. Samples are simulated with different peak temperatures (CGHAZ-1350 °C, FGHAZ-950 °C, ICHAZ-775 °C and SCHAZ-650 °C), characteristic for the different

DOI: 10.14750/ME.2021.051

subzones, and Rykalin 2D model were selected due to the 1 mm sheet thickness. Based on the literatures [86][110][183] and several preliminary experiments [86] to get similar simulated thermal cycles as programmed with 5 s and 30 s cooling time, heating rate for physical simulation is considered as 500 °C/s and holding time at peak = 0.1 s for all experiments. The energy input for $t_{8/5}$ = 5 s and $t_{8/5}$ = 30 s cooling time were obtained as 88 J/mm and 216 J/mm respectively from the software incorporated with physical simulator. The programmed HAZ thermal cycles for the two technological variants 5 s and 30 s are shown in Fig. 5.2a-b respectively.

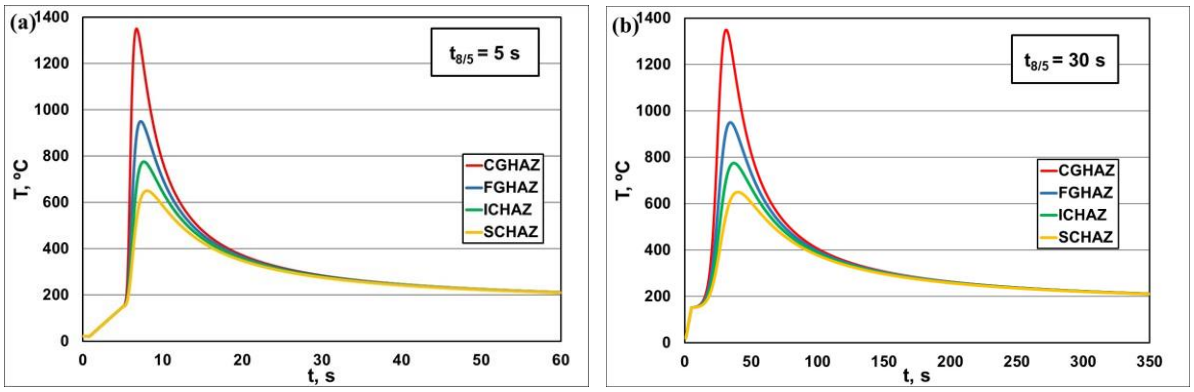

Fig. 5.2. Thermal cycles (a) $t_{8/5}$ = 5 s and (b) $t_{8/5}$ = 30 s

A K (NiCr-Ni) type thermocouple was welded onto the middle of specimen with the use of the specialised micro-welding equipment for temperature record control during the physical simulation as shown in Fig. 5.3a-b respectively.

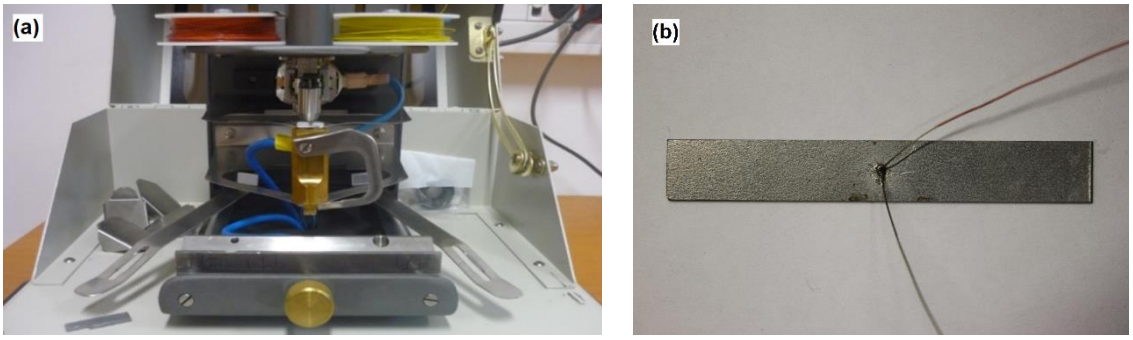

Fig. 5.3. (a) Thermocouple welding machine and (b) sample with the welded thermocouples

The hardness and microstructure of the specimens were then tested and analysed using Vicker's macrohardness test and optical microscope respectively.

5.1.3. Macrohardness and Optical microscopic test

After simulation, the specimens are cut along the symmetry axis where the thermocouples have been attached. The macrohardness of the specimens were tested and analysed using Vicker's hardness tester i.e., Reicherter UH 250 Universal hardness testers with a 10 kgf (or test force of 98.07 N) load and with a 10 s dwell time.

DOI: 10.14750/ME.2021.051

The samples for optical microscopy observations were sectioned through the weld in transverse direction. The sectioned samples were polished with SiC waterproof papers in series of 120, 400, 800 & 2000 ANSI grit and finally with a disc using diamond paste of 1 μm. The specimens were then etched with Nital (2% HNO_3) for 10 s. The specimen for metallography study comprised of BM, HAZ and FZ. The microstructural examination was carried out using an OM (Axio Observer D1m (Zeiss) inverted microscope).

5.2. Results of physical simulation

5.2.1. Optical microscopic tests

The aim is to have some preliminary knowledge about the behaviour of these steels during fusion welding and to estimate what can happen during LBW (especially with the simulation of shorter cooling time). From microstructural figures Appendix [CD, AA4] we can see that in CGHAZ for shorter cooling time ferrite grains (white) are finer but with longer cooling time they are more coarser and in larger number and these softer grains surrounding the martensitic grains (black).

Microstructure of each CGHAZ with $t_{8/5}$ = 5 s is mainly martensite and partially lower bainite. However, in coarse-grained heat affected zone of DP1000, DP1200 and DP1400 with the longer cooling time especially in DP1200 with $t_{8/5}$ = 30 s the microstructure looks like upper bainite. In DP1000 and DP1400 with $t_{8/5}$ = 30 s, mixture of lower and upper bainite and a small fraction of martensite can be observed. The reason for the different transformation microstructures can be found from chemical composition and the CCT-diagram. Martensite formation needs generally fast cooling, while lower and upper bainite are results of slower cooling. Alloying and especially carbon content increases the hardenability and promotes the martensite formation. The lowest C-content of the studied steels in DP1200 may explain the least hardened microstructure (upper bainite) of these steels with $t_{8/5}$ = 30 s. Self-tempering [14] may have some role in the softening of the CGHAZ with $t_{8/5}$ = 30 s compared to 5 s, however it is primarily caused by the formation of upper bainite. Furthermore, the growth of prior austenite grains decreases the hardness, and they may have grown more with higher heat input.

In intercritical heat affected zone martensite begins to transform into austenite. In addition, zone of austenite and ferrite co-existed at this temperature. During cooling process, austenite may transform into ferrite, bainite or martensite in the function of cooling rate. The residual austenite which untransformed may be present and form martensite-austenite constituents. Therefore, martensite content in this zone is generally lower compared to the original microstructure, which results in significant softening.

5.2.2. Hardness tests

The average hardness values for simulated HAZ of DP800, DP1000, DP1200 & DP1400 in the function of the distance from the fusion line are presented in Fig. 5.4a-b. The average hardness values of the base material of DP steels used in this work were measured by using HV10 hardness test are 270, 329, 386 and 470 for DP800, DP1000, DP1200 & DP1400 respectively. The following graphs represent the hardness profiles of the simulated HAZ for all types of dual phase steels used (DP800, DP1000, DP1200 & DP1400), where we can see how the hardness changes in the function of the distance from welding centreline (y). For the

DOI: 10.14750/ME.2021.051

evaluation of hardness data there is no direct standards for DP steels with hardness limits that could be used for the evaluation. Although CR ISO 15608 classification and the related permitted maximum hardness values of EN ISO 15614 cannot be directly connected to these steels, the hardness limits for low-alloyed carbon steels may provide some information. The hardness limit, indicating cold cracking sensivity, is between 380 and 450 HV10 based on the steel category. For shorter (5 s) cooling time the hardness of CGHAZ of all investigated grades is around this value.

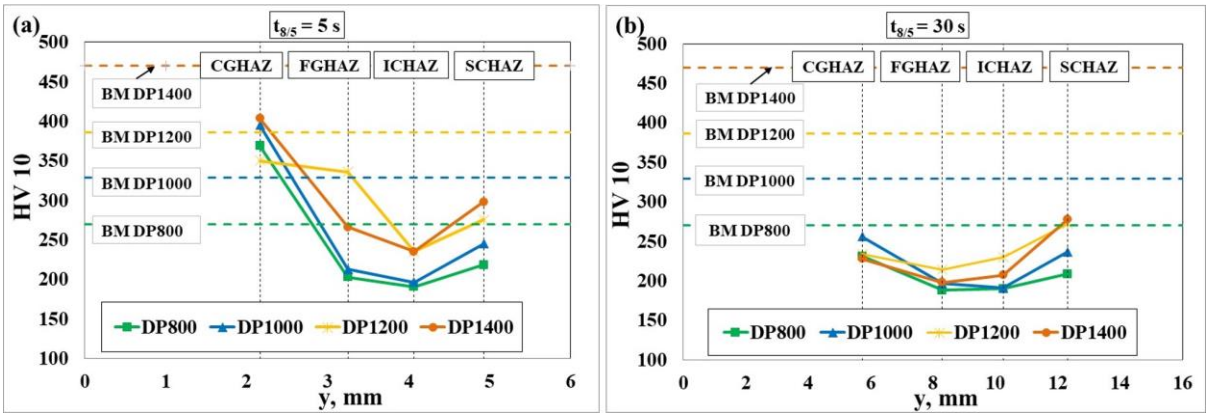

Fig. 5.4. Hardness of simulated HAZ (a) $t_{8/5}$ = 5 s and (b) $t_{8/5}$ = 30 s

For the CGHAZ at $t_{8/5}$= 5 s, the hardness of DP800 is 374 HV10, significantly higher than base metal (39% more), which has the hardness of 270 HV10. In case of DP1000, the CGHAZ having the hardness value of 402 HV10 which is 22% higher than BM. The hardness of DP1200 is 360 HV10, which is 7% less than base metal, which is having the hardness of 386 HV10. For DP1400, the CGHAZ hardness is 411 HV10 which 14% less than the BM (470 HV10). At long cooling time ($t_{8/5}$= 30 s), the CGHAZ hardness of DP800 steel is 241 HV10 which is 11% lower than BM. In case of DP1000, the hardness is 262 HV10 which is 20% less than BM. The CGHAZ hardness of simulated DP1200 is 242 HV10 i.e., 37% less than base metal (386 HV10) which shows significant reduction in hardness value. For DP1400, the CGHAZ hardness is 241 HV10 which is 49% less than the base metal (470 HV10).

For FGHAZ (T_{max} = 950 °C) at $t_{8/5}$ = 5 s, the HAZ hardness of DP800 is 213 HV10 which is 21% lower than BM (270 HV10). For DP1000 the hardness is 224 HV10 which is 32% lower than the BM (329 HV10). In case of DP1200, the FGHAZ hardness is 357 HV10 which is 8% lower than BM (386 HV10). For DP1400, the hardness is 279 HV10 which 41% lower than BM value (470 HV10). At longer $t_{8/5}$ = 30 s, the hardness of DP800 is 195 HV10 which is 28% lower than BM (270 HV10). For DP1000, hardness is 201 HV10 which is 39% lower than the BM (329 HV10). In case of DP1200, the FGHAZ hardness is 217 HV10 which is 44% lower than BM (386 HV10). For DP1400, the hardness is 204 HV10 which 57% lower than BM value (470 HV10).

For ICHAZ (T_{max} =775 °C) at $t_{8/5}$ = 5 s, the hardness of DP800 is 195 HV10 which is 28% lower than BM (270 HV10). For DP1000, hardness is 203 HV10 which is 38% lower than the BM (329 HV10). In case of DP1200, the ICHAZ hardness is 242 HV10 which is 37% lower than BM (386 HV10). For DP1400, the hardness is 239 HV10 which 49% lower than BM value (470 HV10). At longer cooling time, $t_{8/5}$ = 30 s, the hardness of DP800 is 193 HV10 which is 28%

DOI: 10.14750/ME.2021.051

lower than BM (270 HV10). For DP1000, the hardness is 193 HV10 which is 41% lower than the BM (329 HV10). In case of DP1200, the ICHAZ hardness is 233 HV10 which is 40% lower than BM (386 HV10). For DP1400, the hardness is 211 HV10 which 55% lower than BM value (470 HV10).

For SCHAZ (T_{max} =650 °C) at $t_{8/5}$ = 5 s, the hardness of DP800 is 221 HV10 which is 18% lower than BM (270 HV10). For DP1000, the hardness is 246 HV10 which is 25% lower than the BM (329 HV10). In case of DP1200, the SCHAZ hardness is 278 HV10 which is 28% lower than BM (386 HV10). For DP1400, the hardness is 302 HV10 which 36% lower than BM value (470 HV10). At longer $t_{8/5}$= 30 s cooling tme, the hardness of DP800 is 212 HV10 which is 22% lower than BM (270 HV10). For DP1000, the hardness is 239 HV10 which is 27% lower than the BM (329 HV10). In case of DP1200, the SCHAZ hardness is 272 HV10 which is 30% lower than BM (386 HV10). For DP1400, the hardness is 281 HV10 which 40% lower than BM value (470 HV10).

So, we can observe from above results, in CGHAZ, $t_{8/5}$= 5 s, hardening was seen in DP800 and DP1000 while it was significantly higher in DP800 i.e., 39% of BM. In case of FGHAZ and SCHAZ reduction in hardness observed and the maximum reduction seen in SCHAZ. However, in CGHAZ, $t_{8/5}$= 30 s, there is significant reduction in hardness with increasing strength grades of DP steel. So, we can conclude that with higher cooling time, there is increase in softening with the increase of tensile strength of the examined base materials.

Based on the performed HAZ simulations it can be concluded:

- By increasing the $t_{8/5}$ cooling time from 5 s to 30 s the hardness is decreasing in all investigated DP steels and HAZ subzones.
- At short, $t_{8/5}$ = 5 s cooling time, up to DP1000, the CGHAZ of the investigated DP steels tends to hardening, whilst above its grade, in DP1200 and DP1400, CGHAZ is softening compared to BM. In case of long ($t_{8/5}$ = 30 s) cooling time CGHAZ softens in all grades, and the level (ratio) of softening is increasing with the higher grades.
- In case of the investigated DP steels not only ICHAZ and SCHAZ, but FGHAZ also tends to soften in the $t_{8/5}$ = 5-30 s cooling time range, although within the investigated cooling time ($t_{8/5}$ = 5 s) interval ICHAZ is the most critical part of the HAZ in terms of softening.
- In order to minimize the softening in HAZ the application of low heat input LBW is highly recommended as the shortest possible $t_{8/5}$ cooling time resulting sufficient penetration, however the risk of cold cracking may increase in CGHAZ. In this case the supposed critical hardening of CGHAZ might be handled by localized laser PWHT.

DOI: 10.14750/ME.2021.051

6. LASER BEAM WELDING EXPERIMENTS ON DP STEELS

6.1. Welding circumstances

6.1.1. Characteristics of filler material

Based on the material certificate, the chemical composition and the mechanical properties of the filler metal used in diode LBW are presented in Table 6.1 and Table 6.2.

Table 6.1.The chemical composition of the filler metals (weight%)

Material designation	**C**	**Si**	**Mn**	**P**	**S**	**Cr**	**Ni**	**Mo**
***Union X96 (Ø1)	0.1	0.81	1.94	0.015	0.011	0.52	2.28	0.53
Material designation	**V**	**Ti**	**Cu**	**Al**	**Nb**	**B**	**N**	**CE**
***Union X96 (Ø1)	<0.01	0.06	0.06	< 0.01	N/A	N/A	N/A	0.79

Table 6.2.The mechanical properties of the filler metal

Material designation	**$R_{p0.2}$ (MPa)**	**R_m (MPa)**	**A (%)**	**(HV10)**	**CVE, J (at -40 °C)**
***Union X96 (Ø1)	≥ 930	≥ 980	≥ 14.0 (A_5)	N/A	-50 °C: ≥ 47; 20 °C: ≥ 80

***UNION X96 (G895M21Mn4Ni2.5CrMo according to EN ISO 16834-A standard) are Böhler products, Standard minimum values in EN 16834-A

6.1.2. Laser beam welding without filler material

The main motivation for analysing different grade of DP steels using DLBW process is its growing demands in the vehicle industry, to investigate the applicability of diode lasers in this field for welding and PWHT and to understand the hardening and softening behaviour in the welded joint. Based on the literature [25][180] hardening is observed in the CGHAZ and FGHAZ, and some researcher [21][24][22] reported HAZ softening in ICHAZ and SCHAZ with increasing the heat input and the steel grade. Besides the investigated lower strength categories of DP steels (DP800, DP1000) in the literature, in present dissertation higher grades (DP1200 & DP1400) are also studied which are rarely available in the literature. The same, 1 mm thick materials as in the previous section for physical simulation were used with the dimensions of 300 × 150 mm for butt welded joints according to EN 15614-11:2002 and were cut by means of a waterjet cutting machine (CORTINA DS 2600 CNC waterjet). Before welding, the edges of the specimens were cleaned with emery paper and acetone to remove surface oxide. The laser welding was done using a diode laser at the industrial partner. The applied welding parameters, determined by preliminary experiments, used in the present study are shown in Table 6.3.

DOI: 10.14750/ME.2021.051

Table 6.3. Laser beam welding (LBW) and post weld heat treatment parameters (PWHT)

Steel grades	Process	d (mm)	P (W)	s (mm/s)	G (l/min)	Shielding gas purity
DP800/DP1000/ DP1200/DP1400	LBW	2×2	1000	8	7	Ar 4.6
	PWHT	15×6	275	4	7	Ar 4.6

A Laserline LDL 160-3000 diode laser head was mounted on a Reis SRV 40 robotic arm (Fig. 6.1a). The working stretch of the robotic arm is 3800 × 3800 mm. The experimental setup of laser welding is shown in Fig. 6.1b. The diode laser was characterised by a rectangular laser beam spot size 2×2 mm and emitted in continuous wave at 940 nm-980 nm, with maximum output power of 3 kW. The linear heat input was calculated using equation 6.1 [185] with parameters provided in Table 6.3 as 0.125 kJ/mm.

$$Q_{laser} = \frac{P_l}{s} \qquad 6.1$$

where, Q_{laser} is the linear heat input (kJ/mm), P_l is laser output power (kW) and s is the welding speed (mm/s).

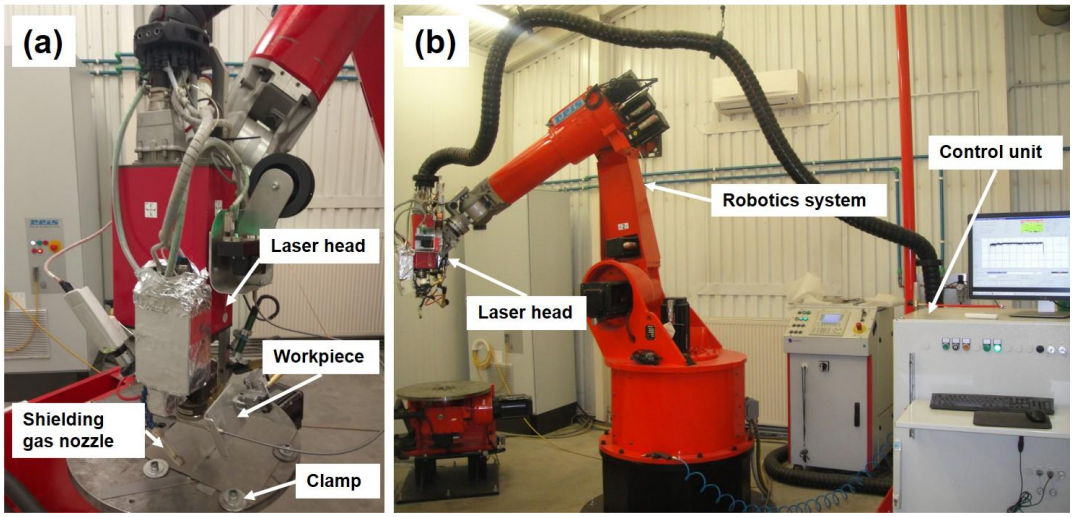

Fig. 6.1. (a) Laser head mounted on robot (b) LBW experimental set up

The specimens to be welded were placed on the working table and mounted to a clamping device to be protect against distortions as shown in Fig. 6.1a. The autogenous laser welded butt joint is presented in Fig. 6.2a.

DOI: 10.14750/ME.2021.051

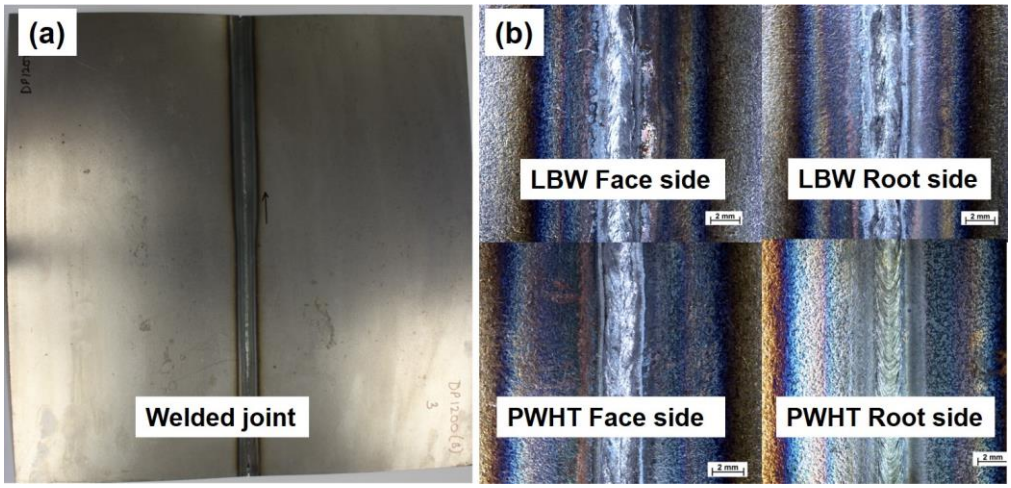

Fig. 6.2. DP1200 (a) Butt welded joint (b) LBW & PWHT joints

Then, the welded joints were subjected to post-weld heat treatments (Fig. 6.2a-b) to study the changes in their microstructure and mechanical properties. A Laserline LDF 5000-40 diode laser (Fig. 6.3a-b) was characterised by a rectangular 15 mm laser beam spot size emitted in continuous wave at 940 nm-1060 nm, with maximum output power of 5 kW was used for post weld heat treatment. Laser heat treatment was carried out at a speed of 4 mm/s in longitudinal direction and output power of 275 W as shown in Fig. 6.3b.

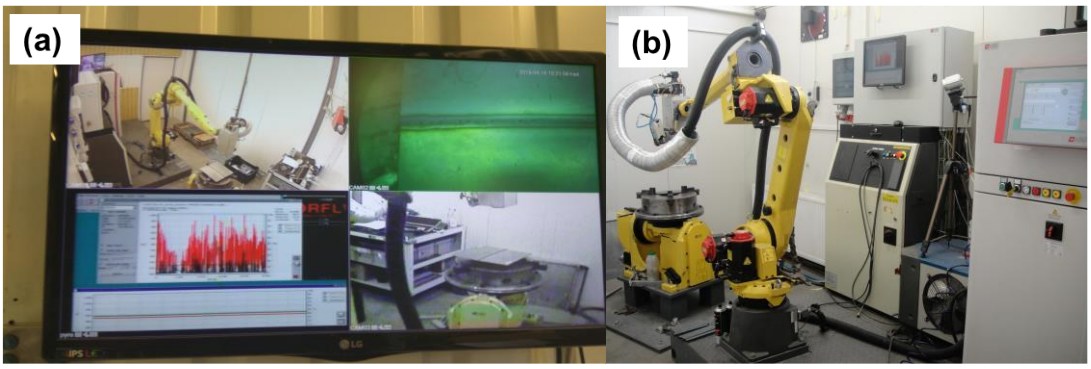

Fig. 6.3. (a) Control display and (b) post welded heat treatment (PWHT) experimental setup

Laser-welding experiments were carried out with the optimal parameters (Table 6.3) to obtain the full-penetrated welds with the good surface quality and the cross-section geometry. Microstructure of the welded joints were observed using an optical microscope (OM) and a scanning electron microscope (SEM). The Vickers microhardness test (ISO 9015-2: 2016) was performed on the etched cross sections with a load of 200 g for a 15 s dwell time. The tensile properties (ISO 4136: 2012) perpendicular to the weld directions were evaluated at room temperature on two samples. A three-point bending test (EN 5173: 2010) was carried out at room temperature on four samples.

DOI: 10.14750/ME.2021.051

6.1.3. Laser beam welding of DP1000 with filler material

The base material used to analyse the LBW with filler material and the effect of PWHT on the welded joint was uncoated cold rolled DP1000 with the dimensions of 300 × 150 mm for butt welded joints according to EN 15614-11:2002 This grade has 1000 MPa guaranteed tensile strength, that can be welded by matching filler material, Union X96 (G895M21Mn4Ni2.5CrMo) with diameter of 1 mm. The motivation of using filler metal was to avoid softening and cross section reduction in the weld. With the application of the filler material the strength of the welded joint may reach the base material level, even after the PWHT. The chemical composition and mechanical properties of the solid filler material are depicted in Table 6.1 and Table 6.2, respectively. A series of preliminary welding tests were performed to obtain optimal laser welding parameters for DP1000 high strength steel. The optimum welding parameters used in the present study are shown in Table 6.4. The linear heat input was calculated using equation 6.1 [185] with parameters provided in Table 6.4 as 0.125 kJ/mm which is similar to the LBW without filler material as presented above in sub-chapter 6.1.2. The parameters were further optimised after the autogenous welding tests in order to get the ideal weld geometry.

Table 6.4.Laser beam welding (LBW) and post weld heat treatment parameters (PWHT)

Steel grade	**Process**	**d (mm)**	**P (W)**	**s (mm/s)**	**f (mm/s)**	**G (l/min)**	**Shielding gas purity**
DP1000	LBW	2×2	2500	20	13	12	Ar 4.6
	PWHT	15×6	275	4	-	7	Ar 4.6

The samples are held rigidly in the fixture by clamp to ensure proper contact between the faying surfaces during laser welding. In addition, each sheet was tack welded by laser at four equidistant places along its length to hold it in place and prevent the contact surfaces from moving away. The single pass laser welding with filler material was carried out using a diode laser as illustrated in Fig. 6.1. The macro-image of the diode laser welded joint with face side and back side are shown in Fig. 6.2b. The post-weld heat treatment was done by diode laser with a rectangular spot of uniform energy distribution after the welded joint cooled down to room temperature, with an output power of 275 W. PWHT was performed on only one side of the welded joint to study the changes in microstructure and mechanical properties, setup as shown in Fig. 6.3. The PWHT temperature used was 650 °C which is ideal for tempering of the martensite and the temperature for PWHT was measured with a pyrometer and also by thermocouples. Microstructure of the welded joints were observed using an optical microscope (OM) and a scanning electron microscope (SEM) analysis. The Vickers microhardness test (ISO 9015-2: 2016) was performed on the etched cross sections with a load of 200 g for a 15 s dwell time. The tensile properties (ISO 4136: 2012) perpendicular to the weld directions and three-point bending test (EN 5173: 2010) were evaluated at room temperature. The residual stress measurement was performed by using X-ray diffraction method (XRD).

DOI: 10.14750/ME.2021.051

6.1.4. Optical microscopy (OM) & Scanning electron microscopy (SEM)

The microstructural examination was carried out using an optical inverted microscope. Fracture surfaces of tensile specimen and the microstructural analysis of different base materials, welded samples were done by scanning electron microscopy by using A ZEISS EVO MA10 scanning electron microscope. Samples were coated with a thin gold layer in order to increase picture quality due to the resin surrounding the specimen.

6.1.5. Microhardness test

The microhardness distributions of joints for LBW and PWHT DP steels samples were obtained using a Mitutoyo MVK-H1 microhardness tester with HV0.2 load and with a 15 s dwell time, and the test was performed on a simple macro test specimen manufactured from the transversal cross section of the welded joint.

6.1.6. Bending tests

The bending test was carried out on LBW and PWHT joints by ZD20 hydraulic testing equipment to identify the tendency to crack during deformation due to the possible presence of weld imperfections in the area of the face and root side of the joint. A three-point bend test (EN 5173: 2010) was carried out on the face side and root side of the joints to evaluate the bending property of joints. The test specimen is a rectangular plate of 300 mm length, width of 20 mm and thickness of 1 mm. The indenter diameter was 10 mm, fixed support roller diameter was 50 mm and the support span (distance between the rollers) was 70 mm.

6.1.7. Tensile tests

The LBW and PWHT transversile tensile test specimens were milled from the welded sheets, and all tests were executed according to ISO 4136:2012 standard with MTS 810.23-250 kN electric hydraulic universal testing equipment. Before tensile tests, the specimens were milled and etched to view FZ & HAZ from the welded sheets for seeing the fracture along the welded specimens.

6.1.8. Cooling time determination, LBW

Analytical method

The major parameter for the determination of the material behaviour of steel is the cooling rate, it dominates overheating rate and holding time. For the evolution of the material properties of steel the $t_{8/5}$ time is the dominating parameter. Transformation of austenite usually takes place in the temperature interval of 800 °C to 500 °C. The cooling time of a given point in weld or HAZ for different heat inputs of laser welding by means of the 2D equation commonly used in a case of arc welding, but adopted for the laser beam welding (Equation 6.2) conditions [186][187].

DOI: 10.14750/ME.2021.051

$$t_{8/5(2D)} = \left(4300 - 4.3 \cdot T_0\right) \cdot 10^5 \cdot \frac{\eta^2 \cdot Q^2}{t^2} \cdot \left[\left(\frac{1}{500 - T_0} \right)^2 - \left(\frac{1}{800 - T_0} \right)^2 \right] \cdot F_2 \qquad 6.2$$

Where, Q= heat input (kJ/mm); T_0= working temperature (°C); η= thermal efficiency; t= material thickness (mm); F_2= joint type factor (for butt joint, value is 0.9)

The component "Q" of the above equation is originally defined as an arc energy in kJ/mm (theoretical heat input), but it was replaced by the energy of laser beam defined as a quotient of the laser power (P) and welding speed (s): Q = P/s (kJ/mm). In turn the thermal efficiency "η" is given for different arc processes and indicates the amount of heat really transferred into the material. Adopting the η factor for laser welding conditions, it was assumed that the thermal efficiency is directly correlated to the value of laser beam absorption by the material. Thus, in the case of conduction laser welding mode the laser beam energy is absorbed on the top surface of a joint and a weld pool (so-called Fresnel absorption). Value of the Fresnel absorption for a laser radiation on the surface of carbon steel is 0.4 [188], so this value was taken as the thermal efficiency "η". The value of absorption coefficient depends upon the surface roughness and surface coating, it can be increased by increasing the surface roughness and providing surface coating [189]. The working temperature was assumed as 20 °C and the material thickness, t = 1 mm. The value of analytical $t_{8/5}$ cooling time during laser beam welding of butt joints with the heat input 0.125 kJ/mm was 2.56 s.

Experimental method (Thermocouple measurement)

The thermal profile in the diode laser beam welding experiments on 1 mm thickness DP800 steel plate was measured. These data can also be used for other grades of DP steels too, since there is not so much difference in their chemical composition, and therefore in the thermophysical properties which affecting temperature field. The 4 sets of K-type thermocouples were welded on the plate along the butt joint and instrumented with Spider8 (4 carrier frequency channels) electronic measuring system for electric measurement of temperature profiles, shown in Fig. 6.4a. The two pairs of thermocouples were placed in the weld zone and remaining two at 2 mm and 3 mm from the edge (Fig. 6.4b) of the joining plates (corresponded to the centreline of the weldment). The experimental set up of the thermocouples for laser beam welding is shown in Fig. 6.4a. The data (temperature-time curve) Fig. 6.4c from the thermocouples output were recorded at a 25 Hz frequency using CATMAN 3 computer software with an HBM Spider8 device connected to a computer.

The measured temperature cycle for a thermocouple at a distance of 1 mm, peak temperature 1350 °C and the $t_{8/5}$ cooling time was 2.8 s. The other two thermocouples were welded at a distance of 2 mm and 3 mm from the weld, measuring a peak temperature of 950 °C and 562 °C, respectively, and the $t_{8/5}$ cooling time for the thermocouple placed at 2 mm was 2.9 s. From both methods (analytical and experimental), it can be concluded that $t_{8/5}$ cooling approximately same which is conforming the result.

DOI: 10.14750/ME.2021.051

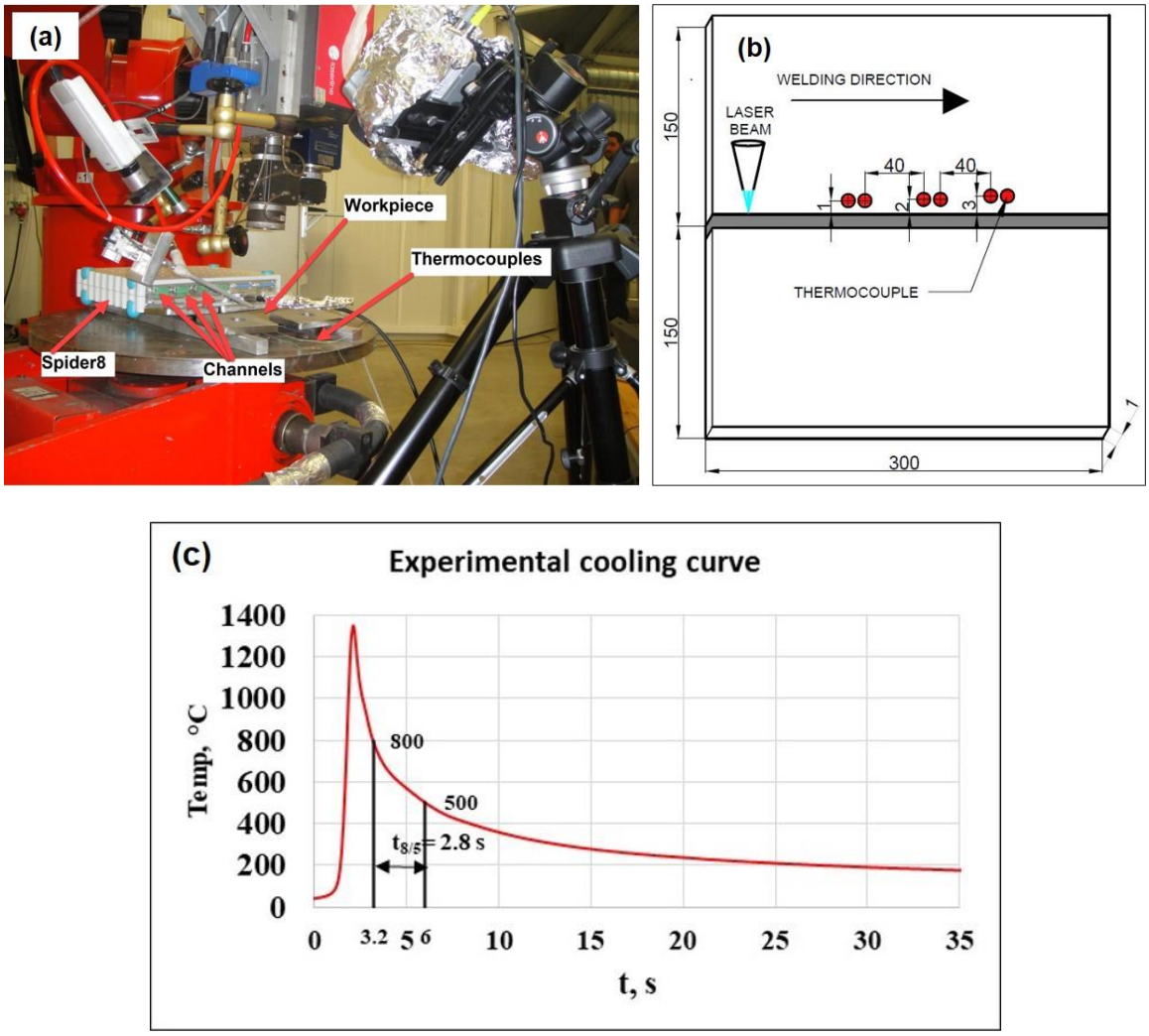

Fig. 6.4. (a) Experimental setup of the thermocouples (b) thermocouple arrangement (c) temperature-time curve, thermocouples output

6.2. Results of autogenous laser beam welding

6.2.1. Microscopic and hardness tests

In the optical micrographs (Fig. 6.6a) of the base materials ferrite parts can be seen in white, and in the SEM images they are more deeply etched than the martensite grains. The BM SEM micrographs of DP800, DP1000, DP1200 & DP1400 are shown in Fig. 6.5. In case of the investigated grades CGHAZ showed mostly lath-like martensitic microstructure forms which is in correlation with measured hardness peaks. The microstructure of the laser-welded and post-weld heat treated joints of DP800 steels were observed by OM and SEM are shown in Fig. 6.6 & Fig. 6.7 respectively.

DOI: 10.14750/ME.2021.051

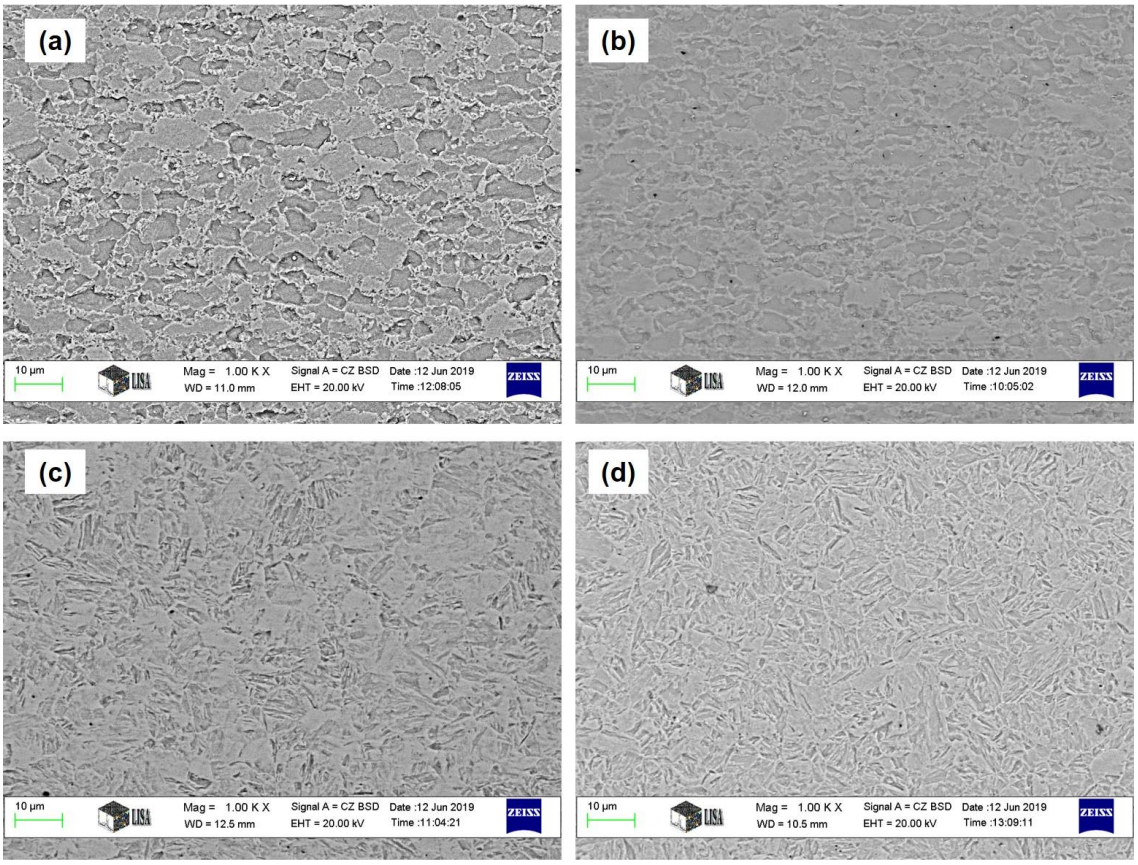

Fig. 6.5.SEM base material (a) DP800; (b) DP1000; (c) DP1200 and (d) DP1400, M= 1000× (2% Nital)

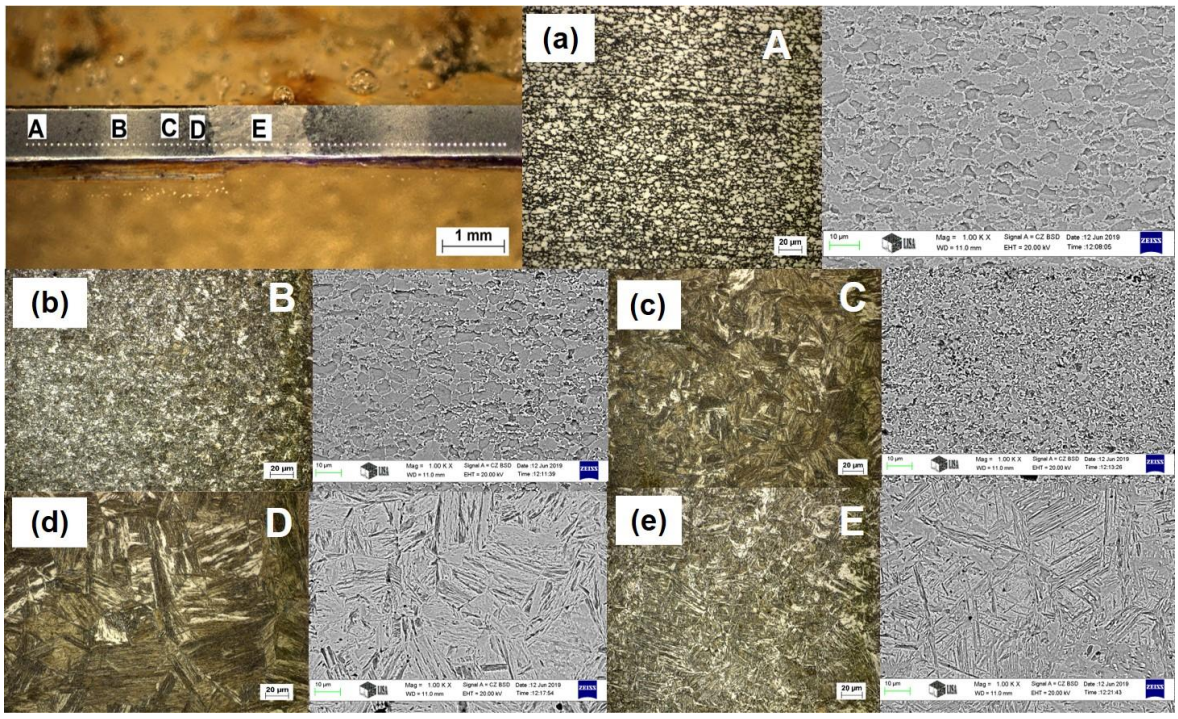

Fig. 6.6. OM and SEM micrographs of different subzones of the LB-welded joint, DP800 steel. (a) BM; (b) ICHAZ; (c) FGHAZ; (d) CGHAZ; (e) FZ; M= 1000× (2% Nital)

DOI: 10.14750/ME.2021.051

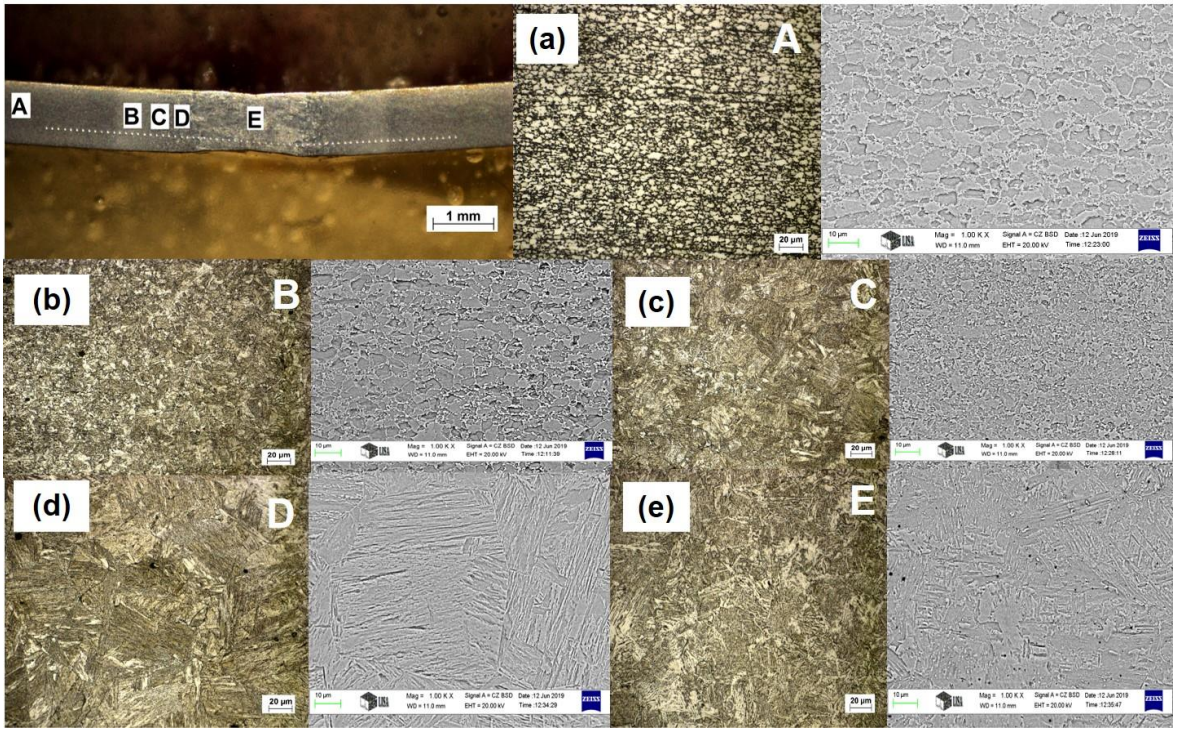

Fig. 6.7. OM and SEM micrographs of different subzones of the PWHT joint, DP800 steel. (a) BM; (b) ICHAZ; (c) FGHAZ; (d) CGHAZ; (e) FZ; M= 1000× (2% Nital)

Also, the microstructure of the laser-welded and post-weld heat treated joints of DP1000, DP1200 & DP1400 steels are presented in the Appendix [CD, AA6 & AA7]

It is remarkable that the value of hardness peaks in HAZ is independent from the grade, which can be explained by the similar chemical composition but different rolling and heat treating routes.In some parts of FGHAZ smaller grain size is measured compared to the base metal. The hardness of FGHAZ was generally higher than the BM due to short $t_{8/5}$ = 2…3 s cooling time in contrary to the physical simulation experiments where basically softening was identified at 5 s. In ICHAZ the ferrite to martensite ratio of the base material is increased due to the welding heat input as a function of the peak temperature. The more amount of ferrite is, the less strength and hardness. This could be the reason for softening of ICHAZ in DP1000, DP1200 and DP1400. When PWHT is applied, tempered martensitic parts can be identified in CGHAZ and in the martensitic grains of ICHAZ. In case of DP1200 and DP1400, the reduction in the strength of the FZ was observed to be nearly the same during LBW and after the PWHT. Due to the PWHT a slight increase of softening was observed near the BM boundary in ICHAZ. PWHT resulted in tempered martensite in HAZ and the overall reduction of hardness peaks in CGHAZ and FGHAZ, nearly equal to BM, which is a significant positive output in terms of cold cracking sensitivity, presumably resulting furthermore in the improvement of energy absorption.

From Fig. 6.8a, for DP800, the FZ has nearly the same hardness as the base material (BM) and most of the HAZ has a higher hardness (around 400 HV0.2), which shows a gradual decrease from the FGHAZ to base metal. PWHT helps in the reduction of hardness peaks, bringing values closer to the base metal, which can be beneficial in terms of cold cracking sensitivity.

DOI: 10.14750/ME.2021.051

In case of DP1000 (Fig. 6.8b) for LBW joint, the FZ and HAZ has higher hardness compared to BM but in SCHAZ softening is observed. However, the PWHT helps in the reduction of hardness peaks in HAZ and FZ.

For DP1200, we can observe from the graph (Fig. 6.8c) that the weld hardness is lower than that of the base metal and also softening occurs in the outer part of the HAZ. Regarding the hardness peaks, similar values were measured compared to DP800, which can be explained by the same heat input and nearly identical chemical compositions but other rolling/heat treating circumstances during steel production. PWHT reduces the hardness peaks in the HAZ without changing significantly the total strength of the welded joint. In case of DP1400 (Fig. 6.8d), the weld zone has a lower hardness for both LBW and PWHT as compared with the BM, but both are approximately the same, even though we can see softening in FZ and lowering of the strength of the weld joint. The ratio of softening could be reduced by the further optimization of PWHT parameters. The CGHAZ and FGHAZ have very high hardness along the length, although it gets lower in ICHAZ, and softening can be observed. The high hardness values can be explained by the presence of high martensite content due to the fast cooling, which is tempered during PWHT.

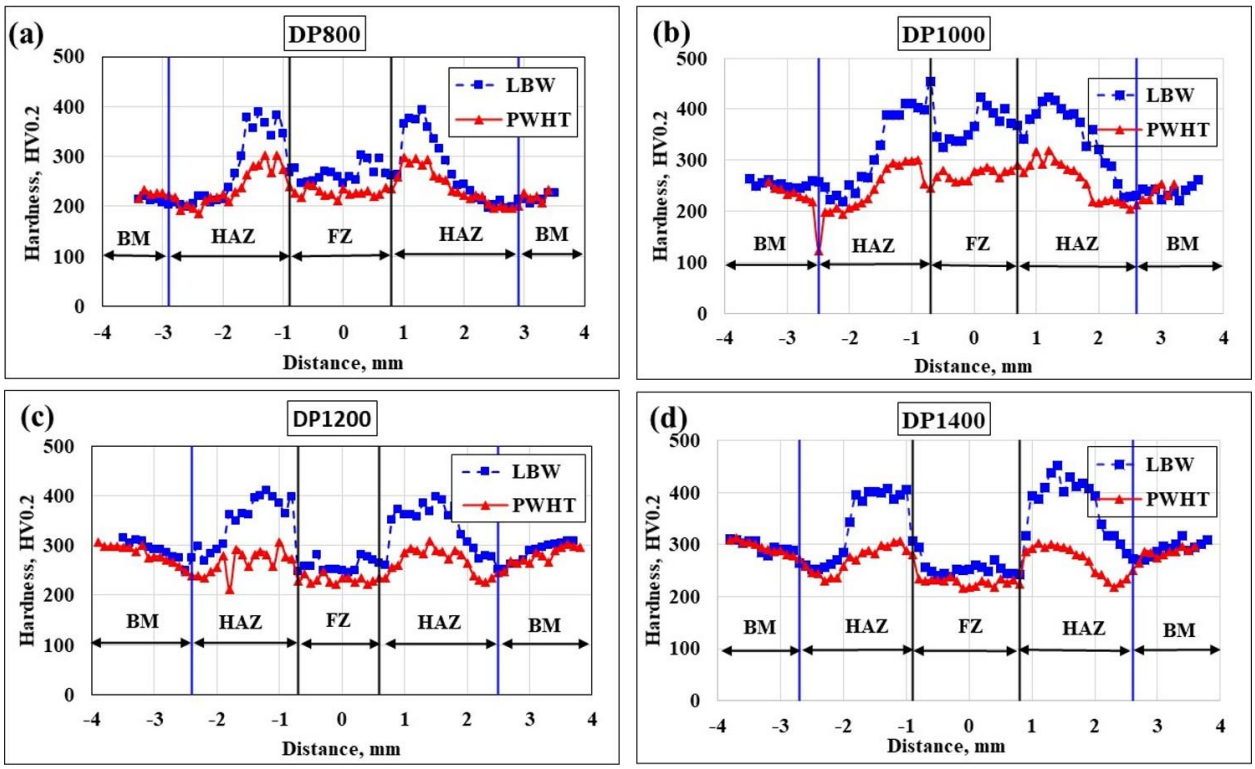

Fig. 6.8. Microhardness distribution graphs: LBW and PWHT (a) DP800 (b) DP1000 (c) DP1200 (d) DP1400

6.2.2. Tensile and bending tests

The tensile specimens of both LBW and PWHT joints were fractured along the weld centreline of the joint for DP800, DP1200, DP1400. While in case DP1000, LBW joints fractured in HAZ and PWHT joint in the weld as shown in Appendix [CD, AA8].

With the given welding parameters, the fracture initiated mostly in the weld zone, which indicates the softening of this part. The softening of weld zone can be presumably compensated

DOI: 10.14750/ME.2021.051

by the application of a matching filler material which are available up to the 1000 MPa tensile strength category (DP1000). Based on the data presented in Appendix [A1], we can conclude that the application of the higher strength base material generally did not result the higher strength of the welded joint with this heat input. PWHT had no significant effect in terms of the tensile strength results since the measured values were just slightly lower (sometimes even higher) compared to the simple LBW tests. Fractography results in DP1400 Appendix [CD, AA9] showed that in laser beam welded samples, failure occurred in welded part, which was typical shear and ductile. Failure took place completely at the 45° plane, which correspond to the plane of maximum shear stress in a specimen under load and is sometimes called ‘‘shear lips’’ However, in the PWHT tensile sample fracture also occurred in FZ, failure was completely shear and ductile. The appearance of extensive micro voids coalescence (MVC) results in the dimple rupture of the fractured surface.

In nearly all cases, results of the bending test for the face side or root side were perfect, without cracks, which indicates good plastic properties of the welded joint. The two exception was root side bending of LBW joint DP800 steel (5F2) & DP1400 (2F2), where the metal is weakened by fusion defect and finally bending fracture occurred. In sample number 3FP1 (PWHT, DP1200) a larger bending angle (α) was achieved because of better plasticity in the zone. The results of the bending test and macrophotos are presented in Appendix [CD, AA10] & [CD, AA11] respectively.

6.3. Results of LBW with filler material

6.3.1. Microscopic and hardness tests

The microstructure is heterogeneous due to the temperature and the chemical gradients that generate during the welding process. Regarding CGHAZ we can conclude that the generally a martensitic microstructure forms which is in correlation with measured hardness peaks. When PWHT is applied, tempering of martensite can be observed in the CGHAZ and in the martensitic grains of ICHAZ which reduces the hardness pattern in HAZ. The microhardness distribution pattern of LBW and PWHT DP1000 welded joint with Union X96 filler material is presented in Fig. 6.9

DOI: 10.14750/ME.2021.051

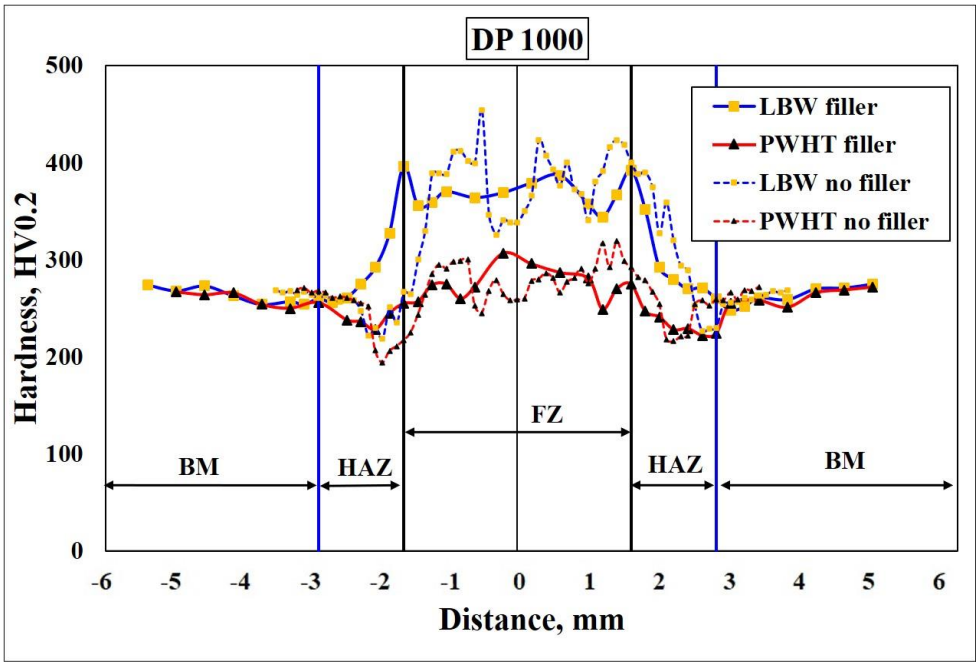

Fig. 6.9. The micro hardness distribution of DP1000 LBW joint with & without filler material

During the LBW of DP1000, the FZ has higher hardness than the BM and the CGHAZ has higher hardness (around 400 HV0.2) than FZ, further there was gradual decrease in the hardness value from CGHAZ to SCHAZ. The hardness change with the heat treatment time was significant, and temperature was more of an influential factor on the hardness. PWHT helps in the reduction of hardness peaks in all zone i.e. FZ and HAZ, but the hardness in the FZ was slightly higher in comparison to the HAZ area.

6.3.2. Tensile and bending tests

The tensile test results of all tested specimens for DP1000 of both LBW and PWHT joints and macrophoto of fractured (SCHAZ) specimen of the joint, are shown in Appendix [A1] and Appendix [CD, AA13].

With the given welding parameters, the fracture initiated in the HAZ, which indicates the softening of SCHAZ part. Based on the data presented for two tested specimens in the table Appendix [A1], we can conclude that the application of the filler material for laser beam welding of DP1000 results the higher tensile strength (1324 MPa & 1592 MPa) of the welded joint with the given heat input. PWHT had significant effect and reduces the tensile strength results however the measured values for tested specimens (1125 MPa & 1183 MPa) are higher compared to the BM guaranteed tensile strength. This reduction in strength, could probably be explained by the tempering of martensite. It can be considered that the microstructural softening during PWHT by tempering effects such as release of internal stress or reduction of dislocation density is comparatively large in the tempered at 650 °C condition. All the fractured LBW and PWHT joints took place approximately 1 to 1.5 mm away from the weld toe in HAZ. The significant difference in the tensile strength of the joint with the filler material is due to the deposition of more filler material at the joint in order to compensate the shrinkage of the material.

DOI: 10.14750/ME.2021.051

In nearly all cases, results of the bending test for the face side or root side were perfect, without cracks, which indicates good plastic properties of the welded joint with filler material. In PWHT samples larger bending angle was achieved because of better plasticity in the zone. The results of the bending tests and bended specimen macro photo are shown in the Appendix [CD, AA14] & [CD, AA15] resspectively. By the combination of filler material and PWHT nearly an equal matching (equal hardness, equal strength) LBW joint of DP1000 has been prepared.

6.3.3. Residual stress measurements

Results of the residual stress measurements in longitudinal and transverse direction were presented in the Fig. 6.10a & Fig. 6.10b respectively for both LBW and PWHT. The longitudinal residual stress in LBW joint near the weld toes was highest i.e. 669 MPa and it further reduces to 520 MPa 1.5 mm away from weld toe in HAZ. However, after PWHT the stress at the weld toe was 40 MPa and 1.5 mm away from the weld toe in HAZ, the stress reduced gradually to -12 MPa (compressive). PWHT can be also considered as a stress relieving process (besides high temperature tempering) whereby residual stresses are reduced in the welds, including the weld metal and HAZ.

In LBW joint, the transverse stress at the weld toe was 24 MPa (tensile) while 1.5 mm away from weld toe in HAZ it was -13 MPa (compressive). In case of PWHT, stress observed at toe was 7 MPa and further in HAZ 1.5 mm away from weld toe was -76 MPa (compressive). So, we can observed from the above results, PWHT significantly reduces the stress in the HAZ which is quite beneficial for the welded joint.

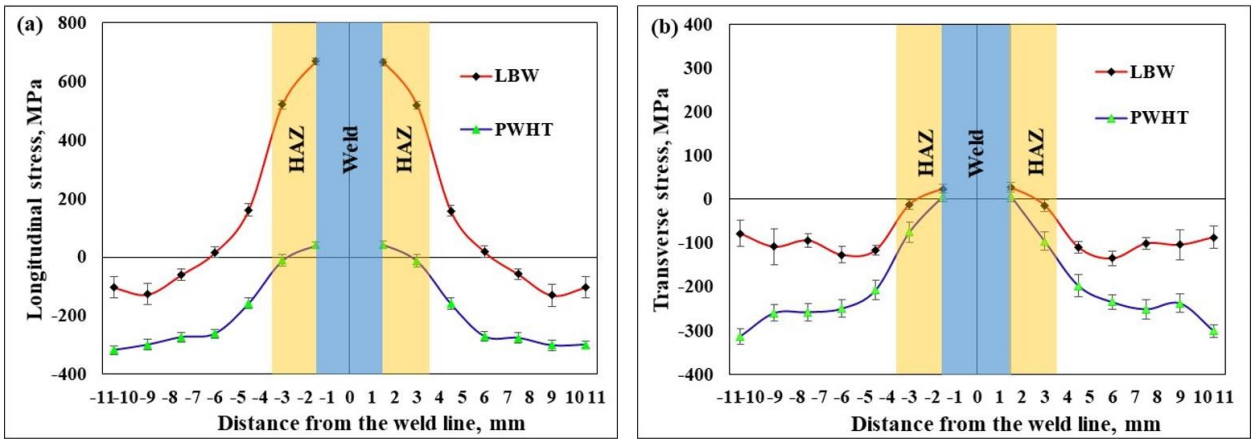

Fig. 6.10. Residual stress graphs on DP1000: (a) longitudinal stress, (b) Transverse stress

DOI: 10.14750/ME.2021.051

7. ELECTRON BEAM WELDING EXPERIMENTS ON HSSS

7.1. Welding circumstances

7.1.1. Characteristics of base materials and filler material

The chemical composition of WELDOX 960E (S960QL in EN 10025-6) and ALFORM 960M, a product of SSAB and VOESTALPINE respectively (for EBW) base materials, filler metal used in EBW, and the mechanical properties based on the materials certificates, Appendix [CD, AA16] are provided in Table 7.1 and Table 7.2, respectively. The CE formulas are used to judge the influence of the alloying elements on the weldability. It can be seen that the thermomechanically controlled process (TMCP) steels i.e. S960M (CE= 0.40) has smaller CE than the quenched and tempered (Q+T) steel i.e. S960QL (CE= 0.55) grades for the same yield strength.

Table 7.1.The chemical composition of the base materials and the filler metal (weight%)

Material designation	**C**	**Si**	**Mn**	**P**	**S**	**Cr**	**Ni**	**Mo**
Weldox 960E	0.170	0.23	1.23	0.011	0.0010	0.20	0.04	0.59
Alform 960M	0.084	0.33	1.65	0.011	0.0005	0.61	0.03	0.29
***Union X96 (Ø1.2 mm)	0.1	0.81	1.94	0.015	0.011	0.52	2.28	0.53
Material designation	**V**	**Ti**	**Cu**	**Al**	**Nb**	**B**	**N**	**CE**
***Union X96 (Ø1.2 mm)	<0.01	0.06	0.06	< 0.01	N/A	N/A	N/A	0.79

Table 7.2.The mechanical properties of the examined base materials and the filler metal

Material designation	**$R_{p0.2}$ (MPa)**	**R_m (MPa)**	**A (%)**	**(HV10)**	**CVE, J (at -40 °C)**
Weldox 960E	1014	1053	14 (A_5)	350	75
Alform 960M	1051	1058	16.9 (A_5)	355	177
***Union X96 (Ø1.2 mm)	≥ 930	≥ 980	≥ 14.0 (A_5)	N/A	-50 °C: ≥ 47; 20 °C: ≥ 80

***UNION X96 (G895M21Mn4Ni2.5CrMo according to EN ISO 16834-A standard) are Böhler products, Standard minimum values in EN 16834-A

7.1.2. Electron beam welding experimental details

The base metals (BM), S960QL and S960M was used for welding experiments and the steel plate of thickness 15 mm were cut into pieces of 300 mm × 150 mm each for a butt welded joint

DOI: 10.14750/ME.2021.051

(according to EN 15614-11:2002 by means of a plasma cutting machine. The area of the HAZ of plasma cutting was removed by machining before the welding. Backing plate from the same grades were used for EBW in single pass with not-through penetration mode to get better result, support the molten materials in the weld pool, to ensure the welding of full thickness of the material and to exclude the possibility of root cavities and spiking [171], formed an assembled unit with the original butt welded joint. The backing plate material was same as of BM and cut into the dimension of 300 mm × 50 mm. Before welding, the edges of the samples were cleaned and milled, base of the specimen from the joining edge on both sample and the surface of backing plate were properly cleaned and carefully machined to secure precise assembling for EBW with maximum allowable air gap of 0.15 mm along all the joint length as shown in Fig. 7.1a. The precise machining and proper assembling are most important part to obtain a good quality of welded joint. The sample were tack welded at few positions by manual TIG welding using the copper-coated solid wire UNION X96 filler material to obtain full depth penetration, prevent any misalignment and to reduce localised thermal stresses and strains at the joint before final EBW. The clamping device was prepared according to the specimen size as shown in Fig. 7.1b for the required EB welded joint. The specimens to be welded were kept with welding fixture to hold the plate rigidly and minimize the distortion as shown in Fig. 7.1b.

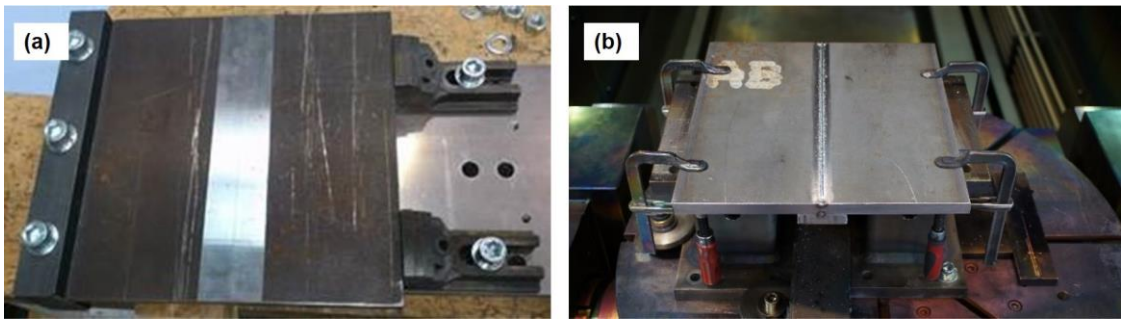

Fig. 7.1. (a) Clamping device and (b) clamp configuration in EB welding of S960QL & S960M specimen

The several preliminary tests were conducted to determine the ideal EBW parameters in full depth penetration condition. The optimal parameters used in the present study are mentioned in Table 7.3. The welding was performed at a speed of 10 mm/s (60 cm/min), accelerating voltage (V_a) of 150 kV and a beam current (I_b) of 49 mA. The working distance (WD) in the welding process was selected as 500 mm and chamber ceiling to surface of the workpiece distance was 284 mm.

Table 7.3. EBW optimal parameters

Steel grade	**V_a (kV)**	**I_b (mA)**	**s (mm/s)**	**d_b (mm)**	**Focus lens for welding (mA)**
S960QL/S960M	150	49	10	0.4	2067

The welding was done in a single pass without a filler metal addition and no preheating. The EBW was performed using EBOCAM EK74C – EG150-30BJ EBW machine, Appendix [CD, A17] in completely vacuum condition, 2×10^{-4} mbar (1.97×10^{-7} atm) and the same level was

DOI: 10.14750/ME.2021.051

maintained in the electron gun and work chamber. The EB welded samples were then allowed to cool in chamber for few minutes to avoid any oxidation and kept outside for further cooling. The linear heat input was calculated using equation 7.1 [190][191] with parameters provided in Table 7.3 and efficiency (η= 0.9) [177] as 661.5 J/mm.

$$Q = \eta \frac{V_a I_b}{s} \qquad 7.1$$

After welding, microstructural and mechanical properties of the EBW joints were investigated. The samples for optical microscope (OM) and scanning electron microscope (SEM) observations were sectioned through the weld in transverse direction. The specimen for metallography study comprised of BM, HAZ and FZ. The microstructural examination was carried out using an OM (Axio Observer D1m (Zeiss) inverted microscope) and SEM (Zeiss Evo MA10) analysis. The Vicker's macro hardness (ISO 22826: 2005) of the BM, HAZ and FZ are tested by Reicherter UH 250 Universal hardness testers with a 10 kgf (or test force of 98.07 N) load and with a 10 s dwell time. Instrumented Charpy V-notch impact tests (according to EN ISO 14556) were done by Heckert instrumented impact testing equipment and fractured surface was observed by SEM. Tensile test was executed with a ZD 100 (1000 kN) hydraulic materials testing equipment at room temperature and the specimens used for mechanical tests were designed according to ISO 4136:2012 standard.

7.1.3. Optical microscopy (OM) & Scanning electron microscopy (SEM)

The specimen for metallography study comprised of BM, HAZ and FZ. Fracture surfaces of Charpy specimens and the microstructural analysis of different base materials, welded samples were done by scanning electron microscope. From the microstructural perspectives, EB welded joint (fusion zone) and HAZ are very important areas for analysis because both these areas undergo very fast cooling rate and major metallurgical transformation takes place.

7.1.4. Macrohardness test

The macrohardness distribution (HV10) were obtained across the EBW and GMAW welded joints of S960QL and S960M steels samples for BM, HAZ and FZ.

7.1.5. Tensile tests

The transverse (perpendicular to welding direction) tensile tests were performed on EB-welded specimens (S960QL & S960M, 15 mm thickness) at room temperature with a ZD 100 (1000 kN) hydraulic tensile testing due to the necessary higher maximal force in accordance with ISO 4136:2012 standard and the ultimate tensile strength of all welded specimens have been determined.

7.1.6. Instrumented Charpy V-notch impact tests (ICITs)

The instrumented Charpy V-notch pendulum impact tests was performed in accordance with EN ISO 14556 standards to evaluate the impact toughness of BM, HAZ, FZ using Heckert instrumented equipment. Specimens incised in the FZ are marked VWT and specimens incised in the HAZ are marked VHT.

DOI: 10.14750/ME.2021.051

Five Charpy V-notch specimens with dimensions of 10 × 10 × 55 mm at -40 °C for BM, HAZ and FZ were tested. The fracture surfaces of the tested samples (whose average value is nearest among 5 tested samples) obtained for BM, HAZ & FZ and examined via a SEM equipped with three-dimensional (3D) fractographic imaging analysis are shown in Appendix [A2]. Also, the expansion (e) of the fractured specimens were measured and analysed.

7.1.7. Residual stress measurement

The base materials (BM) used in this work were the same S960QL & S960M HSSs of the EBW experiments with plate thickness of 15 mm.

The experimental details and optimal parameters of EBW used to produce the joints are described in sub section 7.1.2. During the welding process, the specimens were held rigidly with welding jigs in four corner regions shown in Fig. 7.2.

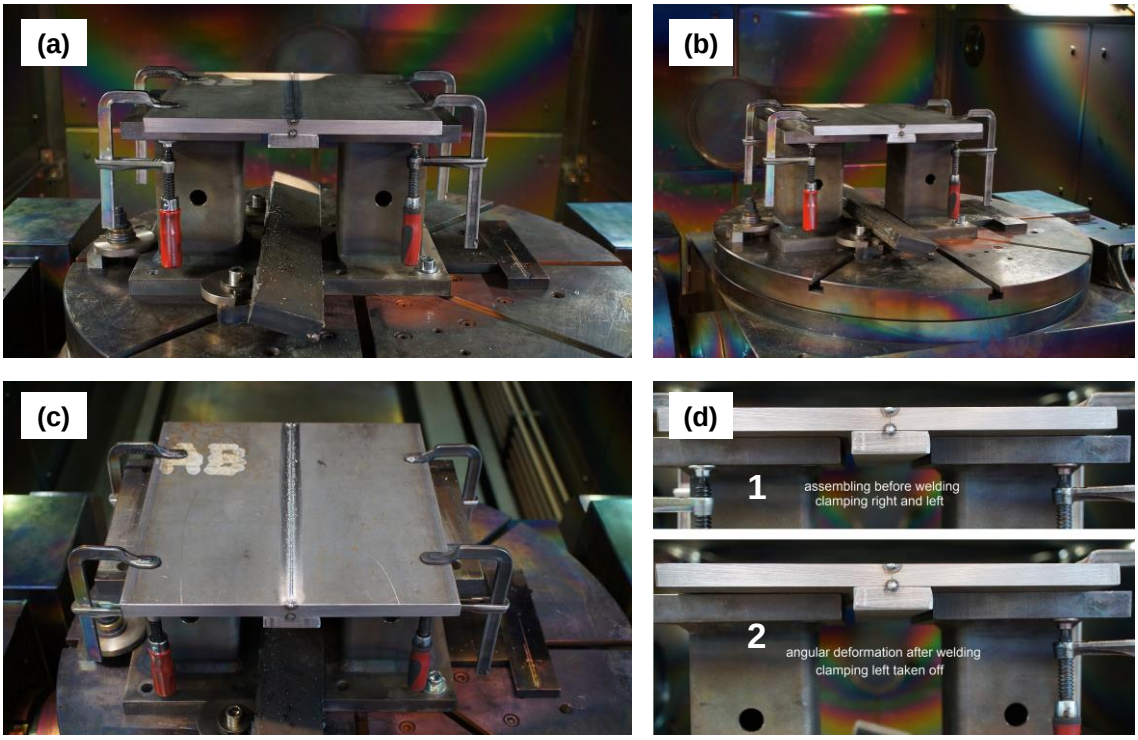

Fig. 7.2. EB welding setup (a) assembly-front (b) assembly-front left (c) after welding (d) after welding, angular deformation

The as-welded surface RS distribution in the 15 mm thick EB welded sample was measured with the X-ray diffraction (XRD) method, presented in Fig. 7.3a. The XRD method with present technology of centreless diffractometers that there are no limitations to the size of the sample and also stress in complicated geometries can be measured at very high angle approximation (usually in the 2θ range of 120°- 170°). In this work, we used very high reflection, 2θ i.e. 155.9° [192].

DOI: 10.14750/ME.2021.051

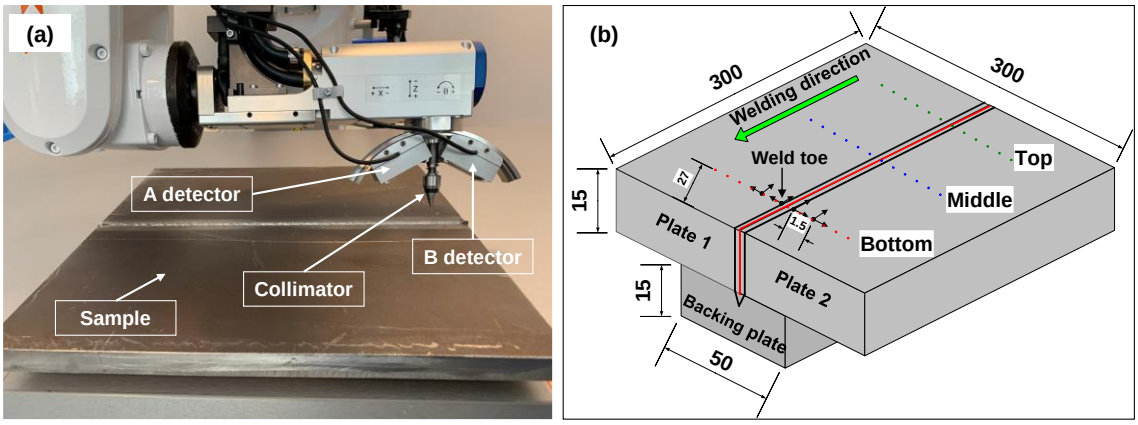

Fig. 7.3. (a) Residual stress test arrangement and (b) schematic of residual stress measurement location

This method is based on the interplanar distances variation of the crystal lattice [117][193]. Fig. 7.3b shows the measurement arrangement and the schematic of the pattern of residual stress taken.

The main purpose is to provide detailed investigation and comparison of the magnitude of RS field induced in two different HSS grades. The RS determinations were carried out on the surface of the welded samples, on top of the bead, in the HAZ, and in the BM. These measurements were carried out according to the well-known modified $\sin^2 \Psi$ technique (elliptical method) where small depth of penetration signify that the sampled region assumed to be in plane stress [28][194]. Standard Cr-Kα source with 30 kV tube voltage and 8 mA tube current was used to measure the ferrite interference line of {211} plane series. Collimator size was 1 mm in diameter. 7/7 tiltings were applied between Ψ: -45°and +45° at each measuring point. Three-line measurements were done on an EBW butt welded plate, 2 lines (top & bottom) are 27 mm from edge and third one in the middle of work piece. Stresses were calculated in longitudinal and in transverse direction at 14 measurement points and distance between them are 1.5 mm. During stress calculation, the Young modulus (E)= 211 GPa and the Poisson's ratio (ν) with 0.3 were considered. The first point (zero) was taken at the weld toe and further the rest of the measurement done as shown in Fig. 7.3b.

7.1.8. Cooling time determination, EBW

Analytical method

The cooling time determination is very important because the microstructural changes in the welded joint and heat affected zone (HAZ) depends on it and further it influences the steels mechanical properties. The cooling time $t_{8/5}$ (3D) is described by the following equation for the three-dimensional heat flow for thick plate [195]:

$$t_{8/5(3D)} = \frac{1}{2\pi\lambda} Q \left[\left(\frac{1}{500 - T_0} \right) - \left(\frac{1}{800 - T_0} \right) \right] \qquad 7.2$$

Q= 661.5 J/mm, η= 0.9 (EBW) [196], λ= 0.0378 J/ (mm.s.K) [14], T_0= 21 °C

DOI: 10.14750/ME.2021.051

where,
$t_{8/5\ (3D)}$ = 3D cooling time from 800 °C to 500 °C (s)
λ= thermal conductivity (W/ (mmK))
Q= linear heat input (J/mm)
T_o= plate initial temperature (°C)

The calculated cooling time from the above mentioned data using equation 7.2 is 2.23 s. The lower ($t_{8/5}$ < 5 s) cooling time (energy input) than arc welding is usual and characteristic of the electron beam welding process. The $t_{8/5}$ depends on energy input which includes the welding speed, welding voltage, welding current and thermal efficiency. Higher the energy input more will be the $t_{8/5}$ cooling time. Higher the preheating temperature and interpass temperature greater will be the $t_{8/5}$ time.

Numerical simulation

The numerical simulation was used to determine the $t_{8/5}$ cooling curve using FE software SYSWELD. EBW numerical model was created using the software. It basically involves three important steps in welding simulation, these are modelling, analysis and post processing. The sample geometry, materials and heat sources fitting belong to the first steps i.e., modelling in weld simulation sequence. The dimensions of the plate used for simulation is 300 x 150 x 15 mm and the number of plates is two for butt welded joint. The important parameters considered for numerical simulation for S960QL material were presented in Table 7.3. The material properties of the steel S355J2 are integrated in the software and used for the calculations because it is similar to the low alloyed as S960QL, therefore there is not a big difference in the thermo-physical properties. The efficiency is a very important parameter, and it is considered η=0.9 for EBW analysis. For modelling electron beam, a conical shaped source with 3D Gaussian distributed thermal energy density source model [197] is applied to get thermal field analysis, shown in Fig. 7.4a.

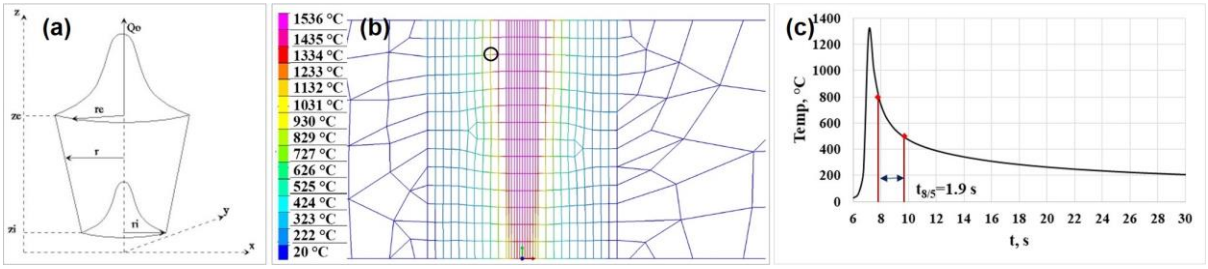

Fig. 7.4.(a) Heat source model [197] *(b) Temperature field (c) Exported HAZ thermal cycle*

The numerically simulated temperature field is presented in the cross section at the heat source in Fig. 7.4b. After numerical simulation, one node in the HAZ was selected (Fig. 7.4c) for finding $t_{8/5}$ cooling time and exported the curve as shown in Fig. 7.4c, the observed cooling time was 1.9 s.

DOI: 10.14750/ME.2021.051

7.2. Comparative analysis results of EB and GMA welded Q+T steel

7.2.1. Comparison of EBW and GMAW by macro examination

Fig. 7.5a & Fig. 7.5b shows a comparison of experimentally observed (stereo microscope) cross sections of an EB and a GMA welded S960QL butt welded joints. The fusion zone is indicated by yellow marked line (liquidus temperature, $T_{liq.}$) in Fig. 7.5. The black marked line in the Fig. 7.5., indicates A_1 line temperature, which represent the visible HAZ region of the welded joints [198]. The experimental results showed the measured fusion zone area and HAZ area are 28 mm^2 and 34 mm^2 respectively, and the corresponding values for GMA welded joint are 257 mm^2 and 95 mm^2 respectively. The process variables comparison of GMAW and EBW are presented in Table 7.4.

Table 7.4.Comparison of GMAW and EBW process variables (t=15 mm).

Steel	**Process variable**	**GMAW**	**EBW**
S960QL	**Weld pass**	9	1
	Filler material	Yes	No
	Speed (mm/s)	3-10	10
	Linear heat input (J/mm)	600 (root pass) 700 (2nd-9th pass)	661
	Interpass temperature, °C	150	0
	Welding main time (s)	40*9=360* (9 passes)	30

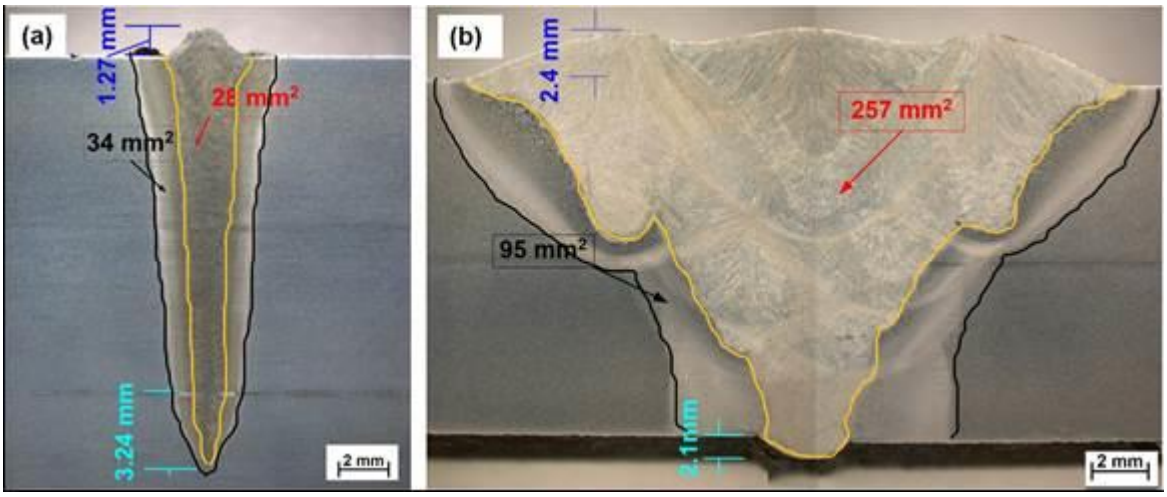

Fig. 7.5. Calculated cross sections area of FZ and HAZ in case of S960QL: (a) EBW (b) GMAW, M=6.5× [62]

DOI: 10.14750/ME.2021.051

7.2.2. Microscopic test

In Fig. 7.6(a), the HAZ subzones are marked in the macro photo and (b) shows the S960QL base material microstructure. Energy dispersive X-ray spectroscopy (EDS) was performed in the FZ to study the distributions of chemical elements are presented in Appendix [CD, AA20].

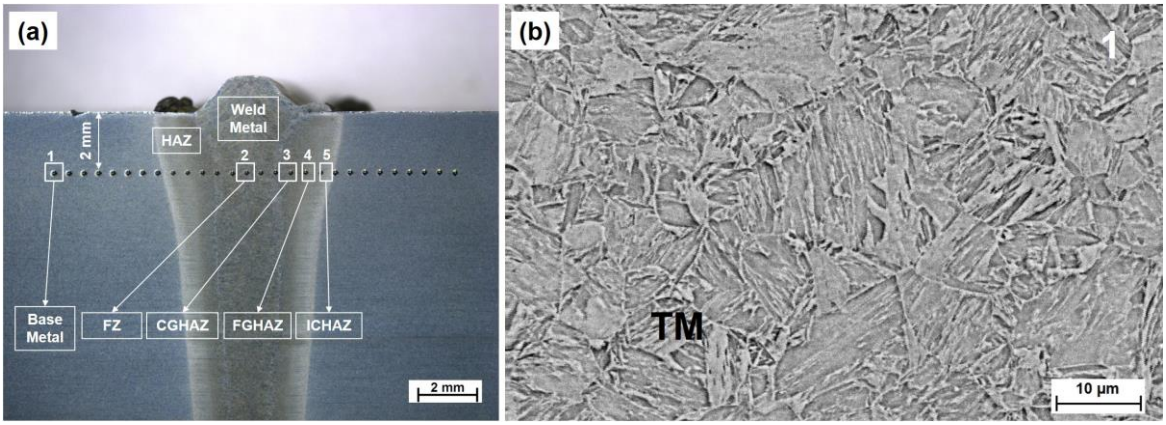

Fig. 7.6. Schematic photograph (a) welded cross section showing the areas where SEM micrographs taken; (b) S960QL base material (2% Nital), M= 1500×

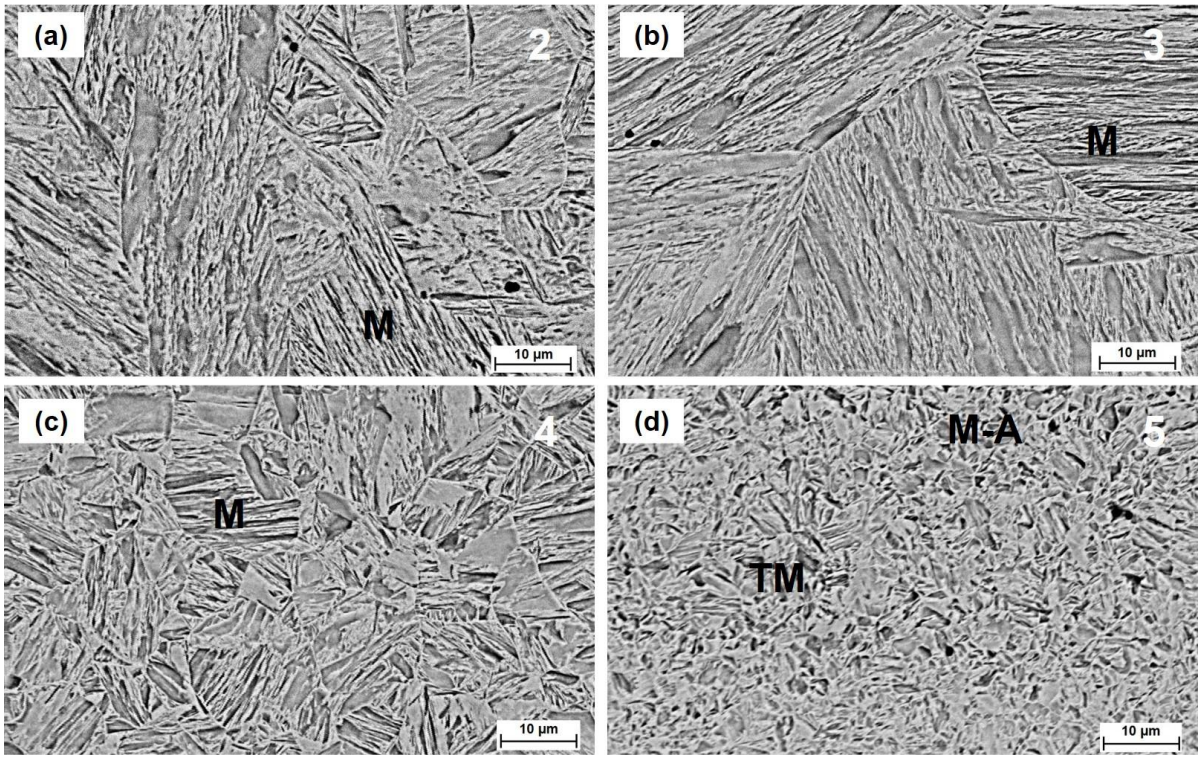

Fig. 7.7. SEM micrographs of different subzones of the EB welded joint, S960QL steel. (a) FZ; (b) CGHAZ; (c) FGHAZ; (d) ICHAZ, (2% Nital), M= 1500×

The microstructure of as-received S960QL base material is consists of tempered martensite in Fig. 7.6(b). The SEM micrograph, Fig. 7.7(a) of FZ shows that it consists of fine dendritic martensitic microstructure which orientation is nearly perpendicular to the weld centre line. This

DOI: 10.14750/ME.2021.051

happened during fusion zone solidification when grains tend to grow in the direction of the maximum heat extraction. The nucleation of prior austenite grains at the fusion boundary caused because it is energetically more favourable [181][115]. The different sub zones of the HAZ viz. CGHAZ, FGHAZ, and ICHAZ are clearly identified depends upon the distance from weld face. The CGHAZ area, Fig. 7.7(b) near the fusion boundary line composed of fully martensite. FGHAZ, Fig. 7.7(c) area also primarily constitutes martensite in accordance with the hardness measurement. The area near the vicinity of base material i.e. ICHAZ, Fig. 7.7(d) composed of a mixture of tempered martensite and M-A parts. So, the HAZ microstructure is predominantly consists of martensite.

7.2.3. Hardness test

The macro hardness tests were performed in accordance with ISO 22826:2005(E) standard practices of EB welded joints using a Reicherter UH250 universal macro hardness tester with a 10 kg load and a 10 s dwell time. Evaluation was performed according to the EN ISO 15614-11 standard which permits HV_{max} = 450 HV10 for the non-heat-treated welded joints (including HAZ) of quenched and tempered high strength steels belonging to the 3rd group of CR ISO 15608. The macro hardness value was measured over weld cross section in three lines (top, middle & bottom) of a simple transversal macro test specimen after the surface preparation using the grinding and polishing. The macro indentations were taken in three horizontal direction of different regions (BM, HAZ & FZ) of a specimen for S960QL are shown in Fig. 7.8a and the GMAW hardness graph for face and root side is shown in Fig. 7.8b.

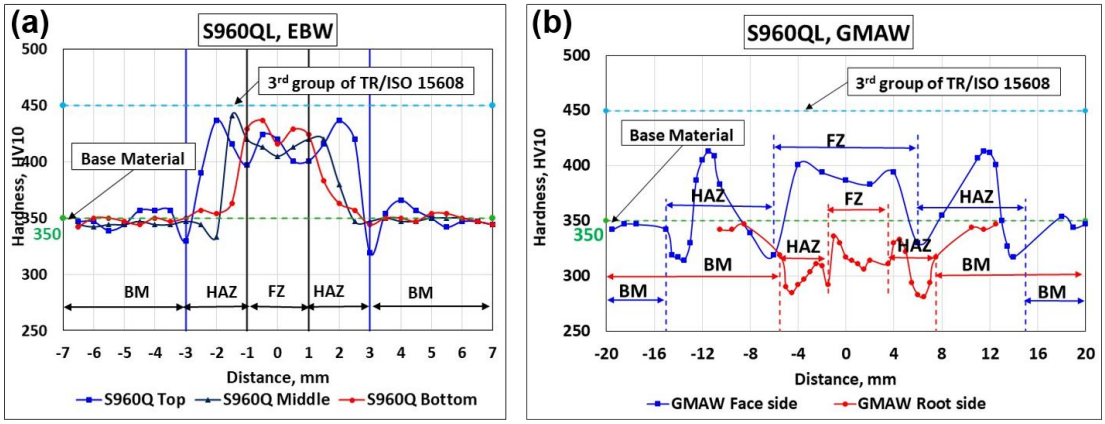

Fig. 7.8.The macro hardness distribution. (a) EBW (b) GMAW [62]

The measured macro hardness of as-received base metal S960QL was approximately 350±7 HV10. The average hardness value of EB welded and GMAW joint for HAZ and FZ are presented in Appendix [CD, AA21]. In EBW, the macro hardness measurement obtained in all three lines of the welded joint are following the similar trend. In FZ, average hardness pattern showed increase in values from top to bottom line while the highest average hardness observed in bottom line. The average hardness of all three lines at the centreline of the FZ was 414±6 HV10. The highest hardness of the HAZ near the fusion line was observed in all three lines which correspond to the FGHAZ and the hardness values decreased further as we moved along the BM. An increased hardness in CGHAZ and FGHAZ was observed since the base metal

DOI: 10.14750/ME.2021.051

transformed fully to martensite after austenitization. The highest hardness in HAZ was 441 HV10 measured in middle line and second highest in top line which was 437 HV10, which can be clearly observed from Fig. 7.8. Blacha et al. [1] in his studies found maximum hardness value in HAZ was 447 HV10 and the average hardness value of FZ was 433 HV10 while considering top line hardness measurement on the same material. A modest variation in the hardness value among the top, middle and bottom of the EB welded specimen was observed, which was mainly related to the different thermal gradient in the thickness. However, little softening can be seen in the ICHAZ area close to A_1 due to the tempering of martensite and small amount of brittle zones.

In GMAW welded joint, FZ has also higher average hardness as compared to HAZ in both face side and root side although in this case the higher hardness was achieved by the use of filler metal. It can be seen from Fig. 7.8(b), the average hardness decreased drastically in root side both in HAZ and FZ, even under to the level of BM due to the tempering effect of multipass welding, which phenomenon did not occur implicitly during EBW due to the single-pass weld.

7.2.4. Tensile test

The tensile strength of the BM according to EN 10204 3.1, material certificate provided by the steel producer was 1053 MPa. According to EN 15614-11 the tensile strength of the test specimen should not be less than the corresponding specified minimum value for the base metal, which is 980 MPa in this case (according to EN 10025-6). However, the measured tensile strength of EBW samples were having the strength of 1038 MPa and 1049 MPa which was approximately around the BM strength.
The tensile test results of EB & GMA welded joints are given in Table 7.5.

Table 7.5.Tensile properties of EBW and GMAW S960QL welded joints.

Steel	**Sample No.**	**EBW**			**GMAW** *[62]*	
		Force (kN)	**Tensile strength (MPa)**	**Fracture location**	**Avg. tensile strength (MPa)**	**Linear Energy (J/mm)**
S960QL	1	397	1038	BM	1030	700
	2	384	1049	BM	977	1000

Also, it was observed that all failures in the tested samples were occurred in the BM not in the welded part as shown in Appendix [CD, AA22]. Also, Blacha et al. [1] in his research work, EBW of HSS S960QL observed that tensile strength of the EBW welded joints were at the same level of the BM and rupture took place out of the weld. Gáspár and Balogh [62] studies showed that average tensile strength of S960QL GMAW joint for the same thickness were 1030 MPa for cooling time ($t_{8/5}$) 5-6 s and linear energy 700 J/mm which is quite close to experimental linear energy used in this paper for EBW i.e. 661.5 J/mm and when GMAW linear energy was increased to 1000 J/mm, then the cooling time was 10 s and corresponding average tensile strength of the welded joints was 977 MPa. So, it can be concluded from above comparison that the average tensile strength of GMAW and EBW are nearly similar with cooling time of 5-6 s while in the case of higher cooling time i.e. 10 s there is high risk that the tensile strength will be below the required minimum limit i.e. 980 MPa. So, by EBW the same strength welded joint was prepared as in GMAW without the application of filler material.

DOI: 10.14750/ME.2021.051

7.2.5. Instrumented Charpy V-notch impact test & fractography

The Charpy V-notch impact test was done to quantify the toughness of the welded joints at the guaranteed operating temperature of the base material [199]. For S960QL steel, in accordance with EN 10025-6 the required minimum impact energy is 27 J at -40 °C. According to the material certificate, the investigated steel plate has 75 J CVN, although 162±46 J was measured during the performed impact test of the base material. The five impact test specimens with dimensions of 10 × 10 × 55 mm at -40 °C for BM, HAZ and FZ were tested. The fracture surfaces of the tested samples (whose average value is nearest among 5 tested samples) obtained for BM, HAZ & FZ and examined via a SEM equipped with three-dimensional (3D) fractographic imaging analysis are shown in Appendix [A2]. In Appendix [A3], the CVN values of the real EB welded joints from the investigated S960QL material are presented with average (Avg.) CVN, standard deviation (Std. dev.) of CVN, where, W_i is crack initiation, W_p is the crack propagation. The average impact toughness value of HAZ and FZ are 45±11 J and 44±20 J respectively. This clearly shows that there is decrease in HAZ and FZ toughness values compared to BM and the average toughness values between HAZ and FZ are similar. However, impact toughness of some tested samples in FZ found to be 20 J which is below the minimum permissible limit provided by the standard and in HAZ, CVN value of one tested sample observed as 27 J which is in consonance with the standard requirement. In particular, the toughness depends upon many factors such as amount of martensite transformation, carbide precipitation and grain size. By comparing the impact test results of EBW and GMAW joints it can be concluded that the measured impact energy values are nearly in the same range, since 44 J average value was measured in the weld zone and 43 J average value in HAZ at the low heat input (5-10 s) GMAW process. By the increase of welding heat input ($t_{8/5}$= 20-30 s) the impact energy values are decreasing both in the weld (38 J) and the HAZ (26 J) of GMAW joints [62]. In another study where ICITs were performed on a GMA welded joint of the same grade 53 J average impact energy was measured in FZ [14]. The Charpy V-notch impact test results on GMAW joint and simulated HAZ are presented in Appendix [A3] [14][62]. It can be remarked that nearly the same toughness level can be achieved in the weld zone with EBW as with GMAW without the application of filler metal.

The instrumented Charpy V-notch impact testing was used because it provides more detailed information about the fracture process and the ductile/brittle behaviour of the material while the conventional Charpy V-notch impact test can provide only the whole energy absorbed during the fracture. The experimental set up of instrumented Charpy V-notch pendulum impact tests was shown in [CD, AA23]. With the application of strain gauge measurement technique, the load-time graph was obtained, and the characteristic points of the fracture process are identified (the start of the plastic strain, maximal force, start of the unstable crack propagation, end of the unstable crack propagation). In the registered graph the unstable crack propagation stage was correlated with the amount of brittle fracture on the fracture surface. From the load-time graph, the force-displacement graph was calculated. Considering that the crack initiation occurs at the maximal force, the registered graph was divided into two parts according to the maximal force. Until the maximum force the area under the curve was considered as the absorbed energy for crack W_i, while the rest for W_p. The toughness of the examined material reduces with the increase of absorbed energy ratio for the crack initiation. The edges show the cleavage cracking in all sub zones; however, the fractured surface appears completely smooth due to its polycrystalline structure. The different fracture features can be clearly seen from the Appendix

DOI: 10.14750/ME.2021.051

[A2]. A brittle fracture with low amount of ductile parts was detected in the registered force-displacement diagrams (VWT & VHT), since the absorbed energy mostly consisted of the crack initiation energy. Since the previous studies verified that the critical, local toughness reduction in the HAZ of the investigated S960QL cannot be avoided by the simple modification of the welding parameters (by the modification of $t_{8/5}$ cooling time range) therefore one of the possible solutions is to minimize the extension of HAZ. By EBW, the area of HAZ, including the brittle subzones (CGHAZ, ICHAZ) can be reduced by three times.

The relationship between CVN and expansion shows that in the weld (FZ) and HAZ whether the CVN values fulfilled the 27 J requirement, mostly brittle fracture was occurred. This is due to the fact that during the impact testing of high strength steels generally higher maximum force values are measured compared to mild steels, which results relatively high CVN, however the value of CVN mostly include the W_i and not W_p, which is almost zero. So, the CVN is higher because of the high W_i, and not unfortunately because of the high W_p. So, if CVN is around or above the requirement, but expansion is almost zero, it means that the material is brittle. It concludes that HAZ of EB welded joint is brittle like HAZ of GMAW joint. However, the major advantage of EBW is that the area of brittle zone is much less especially in HAZ as compared to GMAW process. The toughness will reduce but not in a large cross section as in conventional GMAW.

7.3. Experimental results of EB welded TMCP steel

7.3.1. Microscopic test

SEM micrographs of experimental steel for BM and different sub zones of HAZ are presented in Fig. 7.9(a-e).

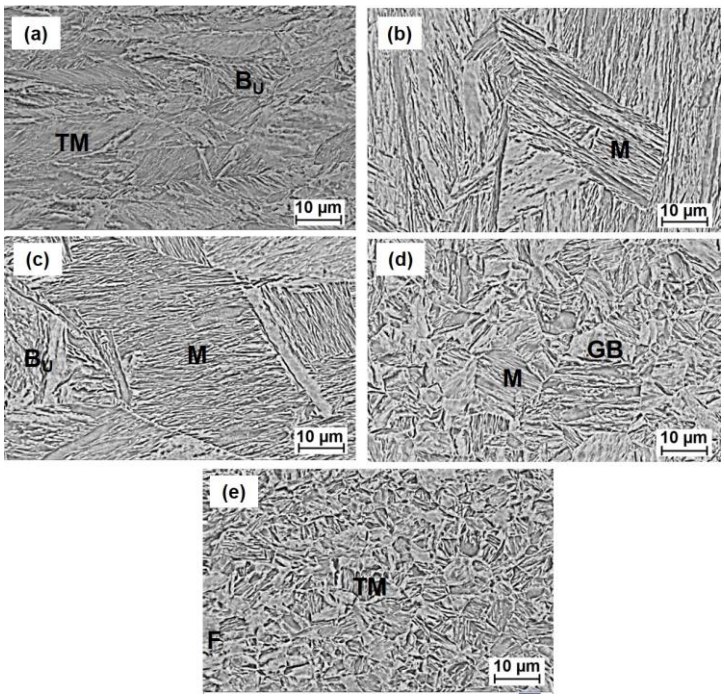

Fig. 7.9. Microstructure: (a) BM, (b) FZ, (c) CGHAZ, (d) FGHAZ and (e) ICHAZ. (2% Nital), M= 1500×

DOI: 10.14750/ME.2021.051

S960M steel BM typically consists of upper bainite (B_U) and auto tempered martensite (TM) microstructure as shown in Fig. 7.9a. Microstructure are very fine and homogenous. The FZ consists of mainly martensitic (M) microstructure, is clearly observed in Fig. 7.9(b). In CGHAZ (Fig. 7.9c), due to lower linear heat input the microstructure has relatively fine grained with upper bainitic and martensitic structure. Also, the grain size of CGHAZ of S960M observed as finer compared to S960QL microstructure in the same subzone. Schaupp et al. also demonstrated in his study that the grain size in the CGHAZ of S960M is smaller and fine-grained than S960QL [200]. The FGHAZ (Fig. 7.9d) has martensitic and granular bainitic (GB) structure. In ICHAZ (Fig. 7.9e), the microstructure comprised of scattered small islands of ferrite (F) and tempered martensite microstructure.

7.3.2. Hardness test

The hardness profiles across the middle of welded joint are shown in Fig. 7.10. The measured BM, FZ and HAZ average hardness were 357±5 HV10, 366±8 HV10 and 370±9 HV10, respectively. FZ and especially HAZ hardness values are slightly higher as compared to the BM. In CGHAZ small local hardness drop can be observed due to the large prior austenite grain size but the FGHAZ has highest hardness of 380 HV10 mainly due to the fine-grained martensitic-bainitic microstructure.

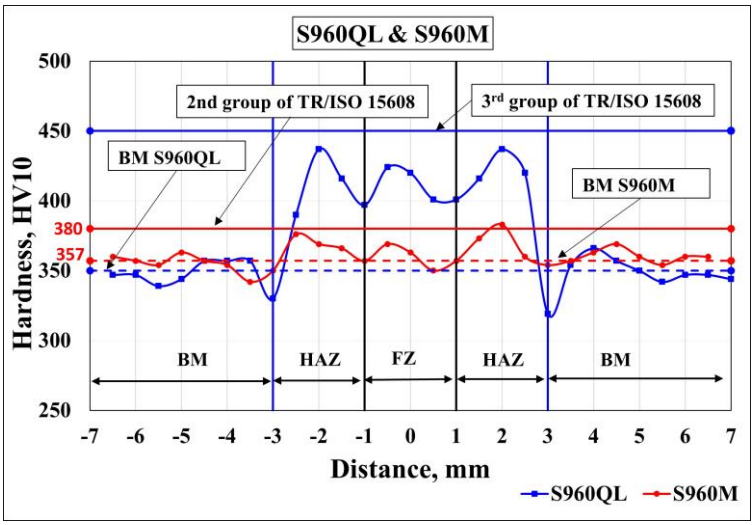

Fig. 7.10. Macrohardness, S960QL & S960M

7.3.3. Tensile test

The tensile strength of the welded joints reached to 995,5 MPa (6% lower than the tensile strength of base material) which is in lower level as of the base material (1058 MPa according to the material certificate).

Table 7.6. Tensile properties of EBW S960M welded joints.

Steel	No.	Force (kN)	Tensile strength (MPa)	Fracture location
S960M	1	366	997	Base material
	2	361	994	Base material

DOI: 10.14750/ME.2021.051

In all the tested samples of welded joints, the fractures occurred in base metal not in weld part as shown in Appendix [CD, AA22]. The tensile test results of S960M EB welded joints are given in Table 7.6.

7.3.4. Results of Instrumented Charpy V-notch test & fractography

The required criterion for minimum absorbed energy for S960M at -40 °C is CVN = 40 J. The average absorbed energy of BM, FZ and HAZ reached to 142±22 J, 78±21 J & 125±64 J, respectively The force-displacement graphs of ICITs and fractograph of tested samples (fractured specimen whose absorbed energy closest to the average absorbed energy of 5 sample) obtained for BM, FZ & HAZ are presented in Appendix [A2]. The observed CVN for BM was 141 J and energy absorbed during W_i and W_p are 42.3 J (30%) & 98.7 J (70%) respectively of the total absorbed energy. The CVN for FZ was observed as 91 J out of this W_i= 68.3 J (75%) while W_p= 22.7 J (25%). However, in case of HAZ, the CVN was 91 J, W_i= 78.3 J (86%) and W_p= 12.7 J (14%). In Appendix [A3], the CVN values, avg., std. dev., W_i & W_p of the all the tested samples for EB welded joints from the investigated S960QL material are presented.

Fractography examination of the BM shows fully ductile fracture with typical dimple morphology at several locations. Fracture morphologies of FZ, was typical transcrystalline in nature and individual grains cannot distinguished on the fractured surface, cleavage facets well observed characterize by river pattern. Fracture surface of HAZ was mixed mode mainly brittle and small portion of ductile characteristic, coarse and fine transcrystalline fracture zone along with small-sized dimples on the surface as shown in Appendix [A2]. It was mostly unstable crack propagation can be seen in the graph.

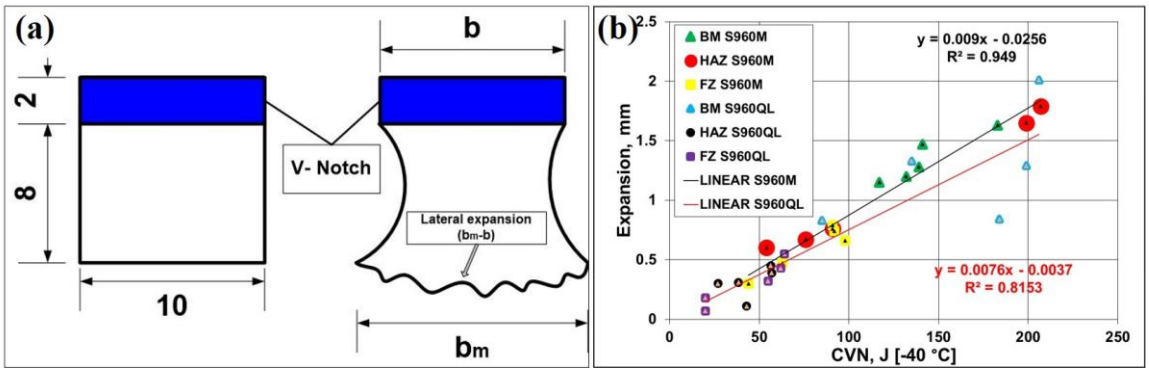

Fig. 7.11. (a) Lateral expansion on CVN test specimen (All dimensions in mm) [201]*; (b) Expansion graph S960QL & S960M.*

The lateral expansion of the fractured surfaces was measured and evaluated; it is a measure of test sample's ductility. When the ductile materials fracture, the materials get deformed. The amount of specimen deformation is measured (in mm) as the difference between deformed width (b_m) and original measured width (b) and is expressed as lateral expansion (b_m-b) or it is defined as the increase in fractured sample width as measured opposite side of the notch, on the striking side. So, as the ductility of material decreases, lateral expansion decreases and vice versa [201]. The schematic diagram and expansion graph of lateral expansion measurement on impact specimen is shown in Fig. 7.11a and Fig. 7.11b respectively.

DOI: 10.14750/ME.2021.051

In Fig. 7.11b, lateral expansion shows the amount of deformation of the material, in case of BM expansion is higher and all values lies above straight line which clearly indicates the toughness of material is higher. Two HAZ specimens exhibit an expansion higher than BM. However, HAZ and FZ has brittle-ductile characteristic, expansion is comparatively lower. From the Fig. 7.11b and the registered force-displacement diagrams, S960M steel and its EB welded joint shows higher toughness as compared to the S960QL category.

7.4. Residual stress measurements

The measured RS distribution i.e. longitudinal and tensile (parallel and perpendicular to the weld direction at each point of measurement respectively) in as welded samples at three different location top, middle and bottom marked by green, blue and red colour respectively as shown in Fig. 7.3b. The data points at 0 mm correspond to the centre of the EB weld whilst the RS data points at positive and negative distances are measured from the toe of the EB weld.

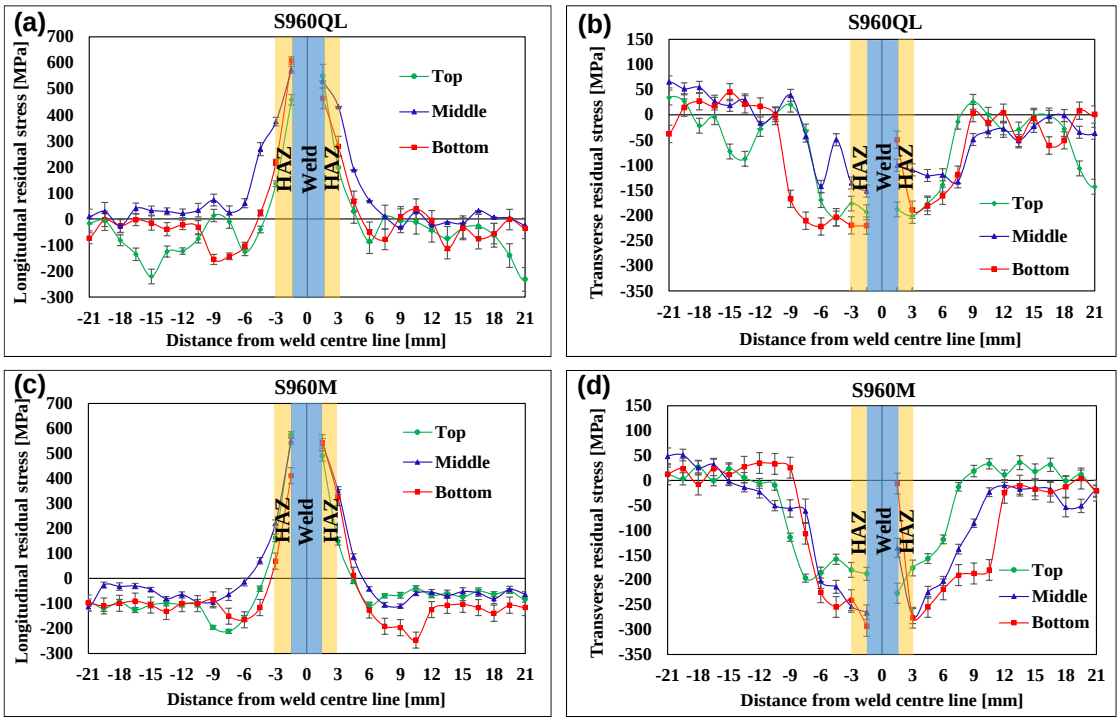

Fig. 7.12.Residual stress graphs: (a) Longitudinal stress, S960QL (b) Transverse stress, S960QL (c) Longitudinal stress, S960M (d) Transverse stress, S960M

In Fig. 7.12(a), the longitudinal RS distribution of S960QL showed the stress profile and the magnitude are almost symmetric about centre. The bottom line having the maximum tensile peak of 609 MPa near the toe of the EB weld. In HAZ, longitudinal tensile stresses decreased rapidly to 218 MPa at -1.5 mm from weld toe and it continues along the BM up to -6 mm and further nearly constant in BM i.e. average -55 MPa. Stress level differences outside of HAZ in BM are due to different surface treatment of the plates before welding. However, in the top and bottom line, the longitudinal tensile stress distribution lies till ±1.5 mm & ±3 mm away from weld toe but in case of the middle of the plate, it was extended along the whole width in BM.

DOI: 10.14750/ME.2021.051

The compressive stress observed in BM at 3 mm and 4.5 mm away from weld toe in both top and bottom line but in middle line it was nearly constant to zero axis. However, it was -221 MPa at -13.5 mm from weld toe. In middle line, tensile stress continued along whole width.

The longitudinal RS distribution of S960M (Fig. 7.12c) in top line showed the maximum tensile peak of about 574 MPa near the weld toe while in HAZ at a distance -1.5 mm from weld toe it decreased to 162 MPa. Tensile longitudinal stress present till 1.5 mm from the weld toe in HAZ, maximum of it lies near the weld toe in both top and bottom line while it decreased further to 70.5 MPa at -3 mm away from weld toe in middle line. In the beginning and end of the welding, longitudinal tensile stress distribution occurs till ±1.5 mm away from weld toe but in case of the middle of the plate, it was observed till ±3 mm from it.

The compressive stress in BM observed at ±3 mm away from weld toe in both beginning and end of the weld but in middle of the plate, it lies ±4.5 mm away from it. However, the compressive stress in bottom line was maximum compared to others two line but the lowest in middle line. The maximum longitudinal tensile stress near the weld toe of the EB welded S960QL joint was slightly higher than the S960M and also higher near the BM-HAZ interface, so overall tensile stress in HAZ of S960QL was more compared to the S960M steel. The amount of restrictive shrinkage was not so high therefore tensile RS does not reach the yield strength of BMs. Besides higher toughness and the lower cold cracking sensitivity of S960M due to the lower HAZ and weld hardness, the additional positive advantage is the lower RS. The transverse RS on the surface of an EB welded plate of S960QL and S960M are shown in Fig. 7.12(b) and Fig. 7.12(d) respectively.

In summary, the stresses vary significantly within the confined area due to the concentrated heat source. The transverse stress is compressive in S960QL near the weld toe i.e. -220 MPa and in S960M it was -293 MPa near the weld toe. It was found that the S960M exhibits more compressive stress than S960QL near the weld toe and for HAZ it follows nearly the same pattern for both steels. The maximum tensile stress experienced in EB welded joints are in longitudinal direction since this direction subjected to highest contraction as a result of the welding thermal cycle. The magnitude of tensile stress near toe of S960QL joint was maximum (60% of the yield strength of the BM) compared to S960M joint (55% of the yield strength of the BM). The effect of the lower linear heat input of the EB welding process can be well observed in the transverse RS of welded samples of HSS S960QL and S960M compared to GMAW [121] & TIG welding [123]. Mobark [50] study showed the average angular deformation at the four corner of GMAW welded joint of S960M with medium heat input was 2.5 mm which is comparatively higher than EBW joint. Due to the smaller linear heat input, the shrinkage process especially the phase transformation leads to the reduction of the tensile RS and also the compressive RS resulting in the characteristic W-shape of RS distribution as shown in the Fig. 7.12(b) and Fig. 7.12(d) respectively.

DOI: 10.14750/ME.2021.051

8. FATIGUE CRACK GROWTH (FCG) TEST

8.1. Experimental circumstances

The FCG tests were executed on three-point bending (TPB) specimens, nominal W values were W= 26 mm and W= 13 mm for the base materials and the welded joints (t= 15 mm), in the 21W and 23W directions, respectively. The position of the notches correlated with the rolling direction (T-S and T-L). Straight notches were applied with 0.2W nominal length, 2 mm wide, 90° tip angle and 0.25 mm tip radius. The positions of the cut specimens from the welded joints are shown in Fig. 8.1[14][139][175].

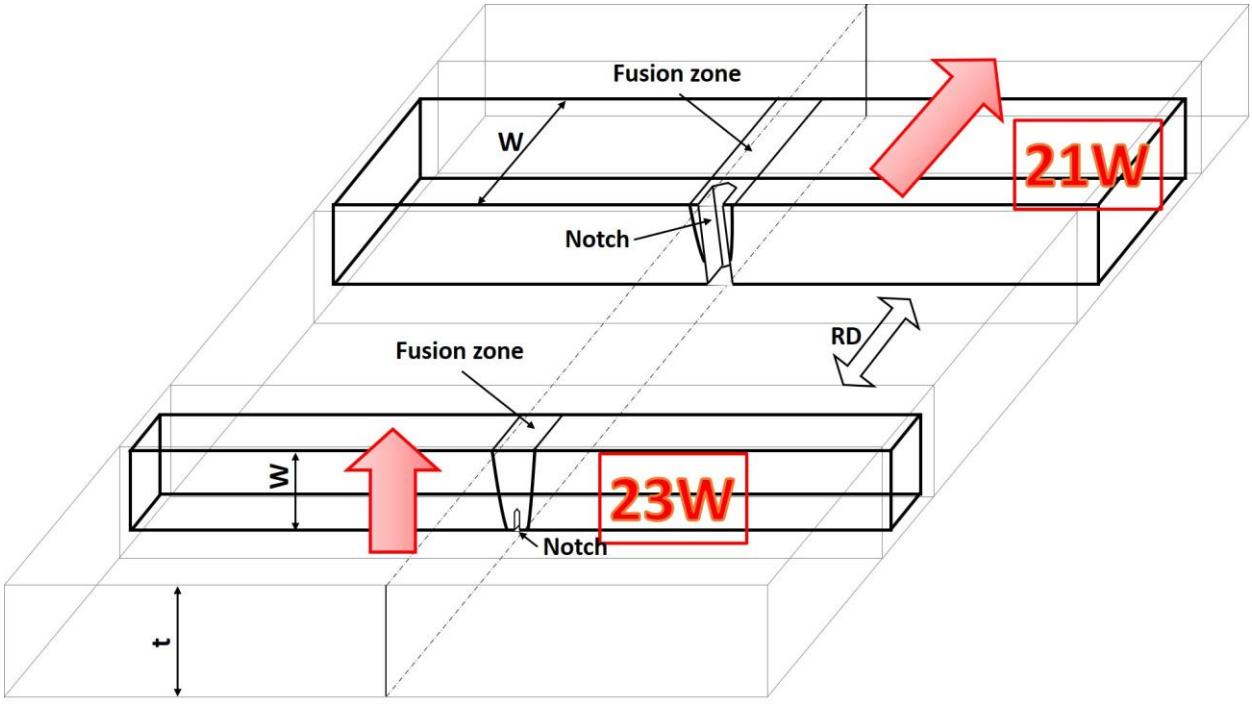

Fig. 8.1. TPB specimen locations in welded joint with notch directions (RD = rolling direction) [14][139][175].

The notch locations, were different, therefore the positions of the notches and the crack paths represent the most important and the typical crack directions in a real welded joints. The notch locations at weld metal (WM), fusion line (FL) and heat-affected zone (HAZ) were presented in schematic diagram Fig. 8.2.

DOI: 10.14750/ME.2021.051

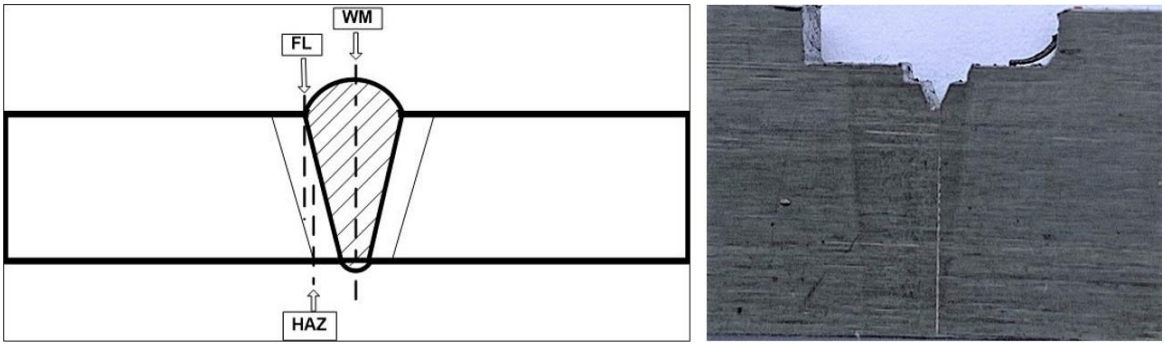

Fig. 8.2. Notch locations and crack paths in the welded joints.

The FCG examinations were performed with tensile stress, R = 0.1 stress ratio, sinusoidal loading wave form, at room temperature using MTS type electro-hydraulic testing equipment (see Fig. 8.3). The loading frequency was f = 20 Hz for two-thirds of the growing crack's length, approximately, and it was f = 5 Hz for the last third. The propagating crack was registered with optical method, using video camera and hundredfold magnification (N = 100x).

Post-weld treating (thermal and/or mechanical) was not applied after welding of electron beam welded joints (investigations in as-welded condition).

Fig. 8.3. MTS type electro-hydraulic testing system equipped for FCG investigations.

The dissertation summarizes the results of FCG investigations on S960QL Q+T, and on S960M thermomechanically rolled high strength steel autogenous EB welded joints (WJ). Furthermore, it also describes the crack length vs. number of cycles curves, kinetic diagram of fatigue crack propagation and presents various calculated results and statistical analysis for both materials and its comparison with GMAW welded joints.

DOI: 10.14750/ME.2021.051

8.2. Fatigue crack growth test

The crack length vs. number of cycles curves can be seen in different orientations for
– S960QL and S960M, autogenous EB welded, T-S/23W orientation in Fig. 8.4;
– S960QL and S960M, autogenous EB welded, T-L/21W orientation in Fig. 8.5;

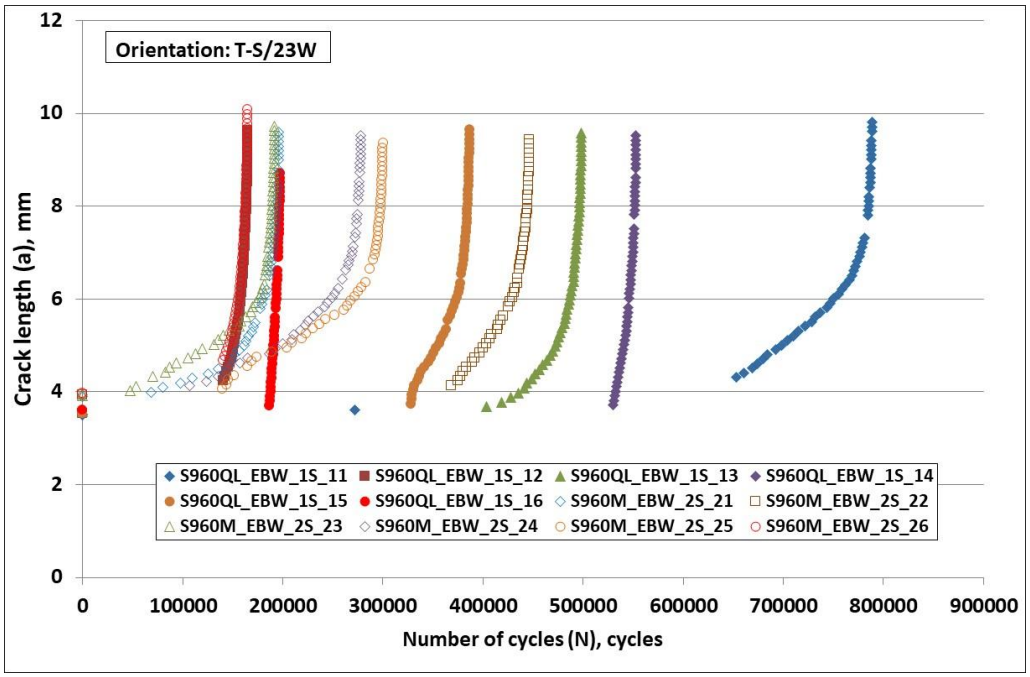

Fig. 8.4.Crack length vs. number of cycles curves in T-S/23W orientation (S960QL/S960M, autogenous EB welded joint).

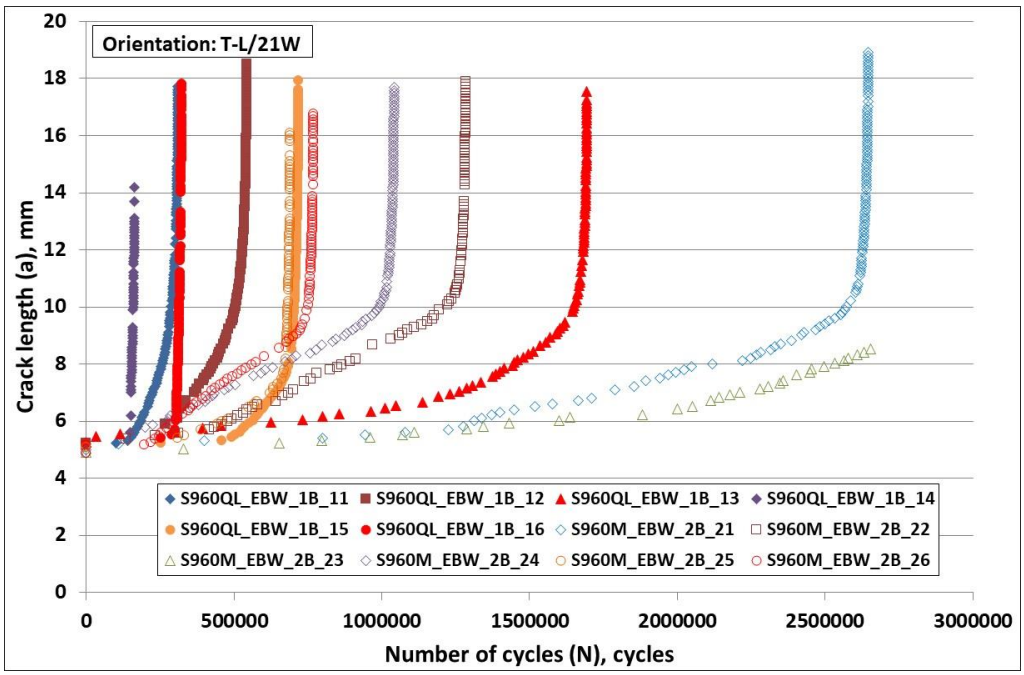

Fig. 8.5. Crack length vs. number of cycles curves in T-L/21W orientation (S960QL/ S960M, autogenous EB welded joint).

DOI: 10.14750/ME.2021.051

Secant method [202] was used to evaluate the fatigue crack growth data. The calculated stress intensity factor range vs. fatigue crack growth rate values, the kinetic diagrams of FCG, are shown in Fig. 8.6 and Fig. 8.7.

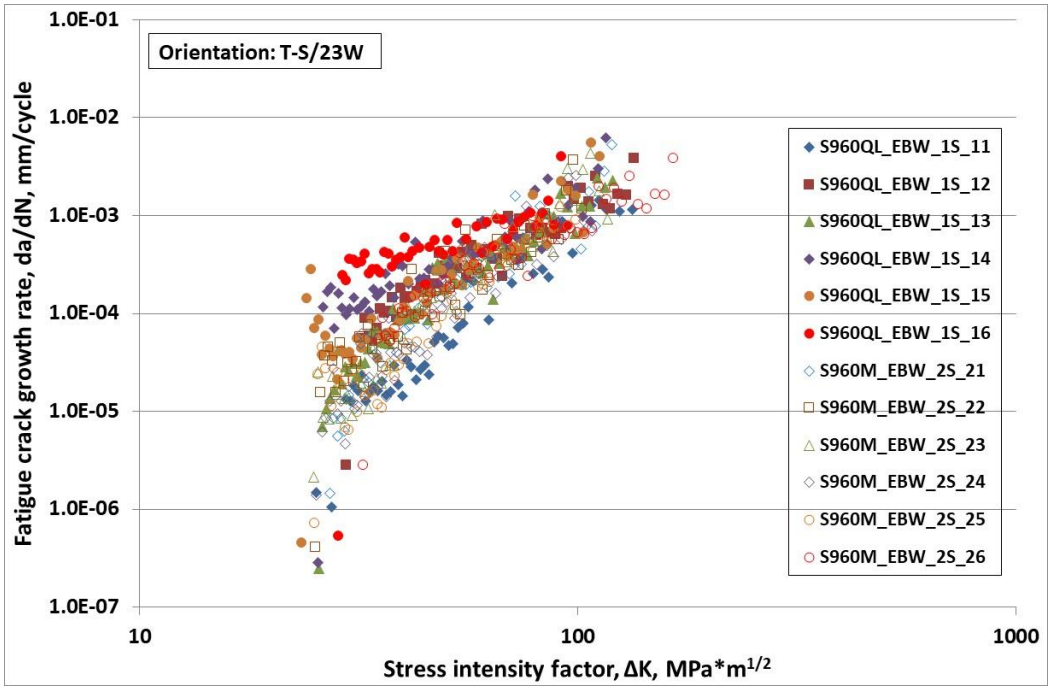

Fig. 8.6. Kinetic diagrams of FCG tests on S960QL / S960M welded joints (altogether 12 specimens).

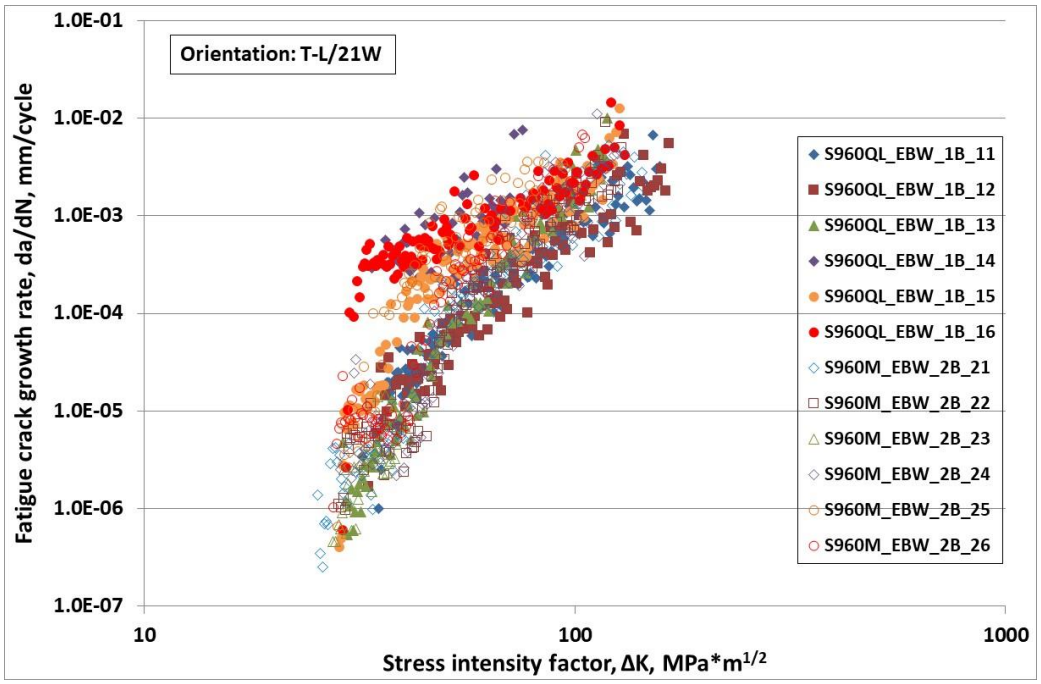

Fig. 8.7. Kinetic diagrams of FCG tests on S960QL/ S960M welded joints (altogether 12 specimens).

DOI: 10.14750/ME.2021.051

The constants (C and n) of the Paris-Erdogan relationship [135] were calculated using the least squares regression method. The data do not belong to the stage II of the kinetic diagram of fatigue crack propagation have been eliminated during the least square regression analysis, for each specimen, systematically.

The calculated n, C values and the dimensions of the tested specimens for S960QL and S960M were summarized in Table 8.1 and Table 8.2.

Table 8.1. FCG test results: S960QL

Specimen ID	**W**	**B**	**a_0**	**Crack path**	**n**	**C**	**Correlation coefficient**
	mm	**mm**	**mm**		**(mm/cycle, MPam$^{1/2}$)**		**(–)**
Specimen location: T-S/23W							
1S_11	12.96	6.55	3.51	WM	3.481	7.411E-11	0.9716
1S_12	12.97	6.56	3.54	WM	2.468	1.502E-08	0.9508
1S_13	12.95	6.56	3.58	FL	3.061	1.014E-09	0.9675
1S_14	12.98	6.55	3.52	FL	1.977	1.534E-07	0.9198
1S_15	12.96	6.54	3.54	HAZ	3.071	1.236E-09	0.9599
1S_16	12.96	6.53	3.61	HAZ	1.330	2.870E-06	0.8347
Specimen location: T-L/21W							
1B_11	25.90	12.87	5.12	WM	3.649	3.976E-11	0.9574
1B_12	25.93	12.87	5.22	WM	3.866	1.292E-11	0.9468
1B_13	25.92	12.87	5.25	FL	5.791	6.381E-15	0.9665
1B_14	25.85	12.87	5.20	FL	2.631	2.184E-08	0.7083
1B_15	25.92	12.87	5.12	HAZ	3.993	2.553E-11	0.9293
1B_16	25.84	12.87	5.21	HAZ	2.062	1.897E-07	0.9245

Table 8.2. FCG test results: S960M

Specimen ID	**W**	**B**	**a_0**	**Crack path**	**n**	**C**	**Correlation coefficient**
	mm	**mm**	**mm**		**(mm/cycle, MPam$^{1/2}$)**		**(–)**
Specimen location: T-S/23W							
2S_21	12.98	6.56	3.90	WM	3.149	6.165E-10	0.9363
2S_22	12.98	6.56	3.94	WM	3.131	7.767E-10	0.9294
2S_23	12.95	6.56	3.93	FL	3.814	4.408E-11	0.9557
2S_24	12.94	6.56	3.93	FL	3.704	4.833E-11	0.9479
2S_25	12.97	6.56	3.96	HAZ	4.021	1.424E-11	0.9653
2S_26	12.97	6.54	3.98	HAZ	2.290	2.314E-08	0.9497
Specimen location: T-L/21W							
2B_21	25.93	13.05	5.01	WM	4.981	1.593E-13	0.9446
2B_22	25.94	13.05	5.19	WM	5.192	6.125E-14	0.9575
2B_23	25.94	13.04	4.92	FL	6.722	1.340E-16	0.7651
2B_24	25.89	13.04	4.89	FL	5.341	3.755E-14	0.9431
2B_25	25.94	13.03	5.09	HAZ	5.367	2.044E-11	0.8991
2B_26	25.94	13.05	4.87	HAZ	5.548	3.465E-14	0.9560

DOI: 10.14750/ME.2021.051

8.3. Comparing the FCG resistance of EB welded and GMA welded joints

The statistical samples of Paris-Erdogan exponent values (n) and their characteristics for S960QL & S960M HSSs EB welded joints and its comparative data with GMA welded joint are presented in Table 8.3. However, the details comparison for Paris-Erdogan exponent values (n) for the notches incised in the FZ are presented and analysed. The comparison of Paris-Erdogan exponent values (n) for S960QL EB welded joint with S960QL GMA welded for the same thickness are presented in Table 8.4. and the comparison of S960M EB welded joint with S960M GMA welded are shown in Table 8.5. The photos of breaking of each specimen for S960QL & S960M are presented in Appendix [A4]. The macrophotos of FCG fractured specimens are presented in Appendix [CD, AA25]

Table 8.3. Statistical samples of Paris-Erdogan exponent values (n)

Base material	**Tech.used**	**Orientation**	**Number of samples**	**Average**	**SD**	**SD coefficient**	**Source**
S960QL	EBW	T-L/21W	6	3.66	1.288	0.351	OWN
		T-S/23W	6	2.56	0.802	0.313	
		T-L/21W and T-S/23W	12	3.11	1.124	0.361	
S960QL	GMAW	T-L/21W	*8*	*4.45*	*0.594*	*0.134*	[14]
		T-S/23W	*7*	*4.19*	*1.106*	*0.264*	
		T-L/21W and T-S/23W	15	4.32	0.847	0.196	
S960M	EBW	T-L/21W	6	5.52	0.616	0.111	OWN
		T-S/23W	6	3.35	0.632	0.188	
		T-L/21W and T-S/23W	12	4.43	1.227	0.276	
S960M	GMAW	T-L/21W	*5*	*3.06*	*0.639*	*0.208*	[50]
		T-S/23W	*6*	*3.23*	*1.017*	*0.315*	
		T-L/21W and T-S/23W	11	3.15	0.830	0.262	

DOI: 10.14750/ME.2021.051

Table 8.4. The mean values of Paris-Erdogan exponent (n) for the welds of S960QL.

Base material	Orientation, Mismatch type	Specimen ID	Crack path	n	$n_{avg.}$	Technology used	Source
S960QL	T-S/23W	1S_11	WM	3.481	2.97	EBW	OWN
		1S_12	WM	2.468			
S960QL	T-L/21W	1B_11	WM	3.649	3.75	EBW	OWN
		1B_12	WM	3.866			
S960QL	T-S/23W, M	9-GMm-FC-23W1	WM	4.133	4.28	GMAW	[14]
		9-GMm-FC-23W3	WM	4.454			
		9-GMm-FC-23W7	WM	4.262			
S960QL	T-L/21W, M	9-GMm-FC-21W1	WM	4.760	4.21	GMAW	[14]
		9-GMm-FC-21W3	WM	3.848			
		9-GMm-FC-21W4	WM	3.466			
		9-GMm-FC-21W6	WM	4.772			

Table 8.5. The mean values of Paris-Erdogan exponent (n) for the welds of S960M.

Base material	Orientation, Mismatch type	Specimen ID	Crack path	n	$n_{avg.}$	Technology used	Source
S960M	T-S/23W	2S_21	WM	3.149	3.14	EBW	OWN
		2S_22	WM	3.131			
S960M	T-L/21W	2B_21	WM	4.981	5.08	EBW	OWN
		2B_22	WM	5.192			
S960M	T-S/23W, M	D9013-5s	WM	3.075	3.17	GMAW	[50]
		D9013-6s	WM	3.281			
S960M	T-L/21W, M	D9013-1	WM	3.933	3.51	GMAW	[50]
		D9013-2	WM	3.104			

DOI: 10.14750/ME.2021.051

8.4. Conclusions of FCG tests

Based on the FCG experimental investigations and their results, comparing them with previous research of various GMA welded joints of S960QL & S960M HSS, the following conclusions can be drawn:

- With the application of high energy beam welding processes required welded joints can be produced, where the appropriate quality consists the eligible resistance to fatigue crack propagation.
- The results of the executed investigations justified the necessity of statistical approaches, especially referring to the directions of the base materials (T-L, L-T, T-S and L-S) and the welded joints (21W and 23W), and the determination of the number of the tested specimens.
- The average values of Paris-Erdogan exponents (n) of the investigated S960QL autogenous EB welded joints were statistically lower in T-L/21W, T-S/23W & (T-L/21W and T-S/23W) direction than the exponents of the S960M EB welded joint.
- The average values of Paris-Erdogan exponents (n) of the investigated S960QL autogenous EB welded joints were lower in T-L/21W, T-S/23W & (T-L/21W and T-S/23W) direction than the exponents of the corresponding grade of GMA welded HSS with same thickness.
- The average values of Paris-Erdogan exponents (n) of the investigated S960M autogenous EB welded joints were higher in T-L/21W, T-S/23W & (T-L/21W and T-S/23W) direction than the exponents of the corresponding grade of GMA welded HSS with same thickness.
- The tendency of the FCG resistance of EBW & GMAW are not the same at the investigated Q+T and TMCP steels. Therefore, the statistical based qualification of the differences requires further tests.
- The electron beam welded joints of the investigated S960QL steel are significantly more sensitive to the location (FZ, FL, HAZ) of the fatigue cracks than the welded joints of the examined S960M steel.
- The fatigue crack growth resistance of the investigated S960M steel in the examined directions (21 and 23) is significantly different, there is no such difference for the investigated Q+T steel.

DOI: 10.14750/ME.2021.051

9. THESES – NEW SCIENTIFIC RESULTS

T1. Based on the detailed HAZ characterization of dual-phase steels (DP800, DP1000, DP1200 & DP1400) by GLEEBLE 3500 thermomechanical simulator for the 5-30 s cooling time interval the HAZ is susceptible to hardening and softening in the function of subzones and $t_{8/5}$ cooling time (6):

a) At short, $t_{8/5}$ = 5 s cooling time, up to DP1000, the CGHAZ of the investigated DP steels tends to hardening, whilst above its grade, in DP1200 and DP1400, CGHAZ is softening compared to BM. In case of long ($t_{8/5}$ = 30 s) cooling time CGHAZ softens in all grades, and the level (ratio) of softening is increasing with the higher grades.

b) Among the investigated subzones not only ICHAZ and SCHAZ, but FGHAZ also tends to soften in the $t_{8/5}$ = 5-30 s cooling time range, although at the shorter ($t_{8/5}$ = 5 s) cooling time ICHAZ is the most critical part of the HAZ in terms of softening.

T2. Based on the performed diode laser beam welding and post weld heat treating experiments on the investigated DP steels (DP800, DP1000, DP1200, DP1400), I verified the beneficial effect of the technology on the joint properties (3) (4) (8):

a) Due to the flexible adjustment of spot diameter in autogenous diode laser beam welding and post-weld heat treatment the hardness peaks in CGHAZ and FGHAZ of the investigated DP steels can be reduced to the level of base materials, resulting lower cold cracking sensitivity, without losing significantly the load bearing capacity of the welded joints.

b) Nearly equal-matching welded joint can be prepared with significantly lower longitudinal and transversal residual stresses from 1 mm thick DP1000 steel sheets by diode laser welding with G895M21Mn4Ni2.5CrMo (according to EN ISO 16834-A standard) filler metal and post-weld heat treatment.

T3. Based on the performed high vacuum electron beam welding experiments on the investigated 15 mm thick S960QL and S960M steels (1) (25):

a) Approximately same strength and toughness welded joint could be prepared from S960QL with electron beam welding as with gas metal arc welding without the application of alloyed filler material. Electron beam welding is an effective way to compensate the HAZ brittleness, characteristic in the whole 2.5-30 s $t_{8/5}$ range of S960QL, by the significantly narrower heat affected zone.

b) A nearly equal matching weld with low cold cracking sensitivity can be achieved by the autogenous EBW with S960M.

DOI: 10.14750/ME.2021.051

T4. Based on the performed residual stress measurements with XRD on the electron beam welded joints (2):
   a) The maximum longitudinal tensile stress near the weld toe of the EB welded S960QL joint is higher than the S960M.
   b) The transverse residual stresses in the S960QL and S960M welded samples shown the characteristic W-shape of residual stress distribution.

T5. The electron beam welded joints of the investigated S960QL steel are significantly more sensitive to the location (FZ, FL, HAZ) of the fatigue cracks than the welded joints of the examined S960M EB welded joint. I proved this statement by fatigue crack growth tests performed and analyzed with cracks propagating in different zones of the welded joint. (26)

T6. The fatigue crack growth resistance of the investigated S960M EB welded joints in the examined directions (21 and 23) is significantly different, there is no such difference for the investigated S960QL grade. I proved this statement by fatigue crack growth tests performed and analyzed in different directions. (26)

DOI: 10.14750/ME.2021.051

10. SUMMARY

The high power density beam processes have given major impetus in the application of HSSs over other traditional welding processes. In this dissertation, application of LBW process for thin sheet (1 mm) of different grades of DP steel (DP800, DP1000, DP1200, DP1400) and EBW process for thick plate (15 mm) HSSs (S960Q & S960M) are presented.

The major findings of this work are listed below:

Physical simulation results of various grades of DP steels presented in the dissertation, showed that the HAZ of DP steels can harden and also soften depending on the peak temperature in the subzones and the value of $t_{8/5}$ cooling time. So, DP steels can have a more complex behaviour in fusion welding (especially in LBW) compared to RSW, when basically the significant hardening generates problems. By increasing the cooling time the hardness is decreasing in all investigated DP steels and HAZ subzones. At short, $t_{8/5}$ = 5 s cooling time, up to DP1000, the CGHAZ of the investigated DP steels tends to hardening, whilst above its grade, in DP1200 and DP1400, CGHAZ is softening compared to BM. In case of long ($t_{8/5}$ = 30 s) cooling time CGHAZ softens in all grades, and the level (ratio) of softening is increasing with the higher grades. Not only ICHAZ and SCHAZ, but FGHAZ also tends to soften in this cooling time range, although within the investigated cooling time interval ICHAZ is the most critical part of the HAZ in terms of softening. In order to minimize the softening in HAZ the application of low heat input LBW is highly recommended as the shortest possible cooling time resulting sufficient penetration, however the risk of cold cracking my increase in CGHAZ. In this case the supposed critical hardening of CGHAZ can be handled by localized laser PWHT, as it was verified during the diode laser experiments.

There are significant benefits associated with choosing a diode laser based welding process over other laser beam welding processes for the welding of various grades of DP steels. These include the fact that the welding and post weld heat treatment for the reducation of brittle hardness peaks in HAZ can be performed with the same equipment. Autogeneous LBW experiments showed that diode lasers can be effectively used to the welding of DP steels. Due to the relatively short, 2…3 s cooling time, the softening of FGHAZ can be avoided by this technology and the width of softened subzones can be minimized. Although significant hardness peaks can be identified in HAZ close to the fusion line, which can be reduced by PWHT with an increased spot size and reduced power of diode laser. Another beneficial effect is the elimination of residual stresses which were measured by XRD on as-welded and PWHT joints. In the investigated grades, the peak hardness in HAZ was nearly the same in all grades, which can be explained by the similar chemical composition of the base materials. It should be also remarked that PWHT had no significant effect in terms of the tensile strength results since the measured values were just slightly lower (sometimes even higher) compared to the simple LBW tests, therefore the static load bearing ability of the joints did not reduce significantly.

DOI: 10.14750/ME.2021.051

Related to the LBW experiments on DP steels with a matching filler material (X96, Ø1) the higher tensile strength of the welded joint should be highlighted, although the hardness distribution was similar to the autogeneous welded joints. Therefore, the basic motivation of the application of filler metal is not (only) the increase of weld hardness, but to avoid the cross section reduction characteristic in autogeneous weld. The location of the fracture in this case was observed mostly in the outer part of the HAZ instead of the weld.

During the cooling time measurements and calculations related to the LBW experiments it was verified that the analytical method results close value ($t_{8/5}$= 2.56 s) to the thermocouple measurement ($t_{8/5}$= 2.8 s) by considering k=0.4 to the Fresnel absorption value proposed by the literature, however this value should be modified to 0.42 for these experimental circumstances in order to get exactly the same value with the temperature measurement. However, for EBW process the calculated cooling time by analytical method was 2.23 s and the cooling time determined by the numerically simulated method was 1.9 s.

There are significant benefits associated with choosing a electron beam welding process over GMAW for the welding of S960QL HSSs of thickness 15 mm. These include the fact that the extent of brittle HAZ is significantly reduced (3 times), and the average extension of the FZ is 10 times lower through using a EBW process. For EBW, the cooling time obtained by the analytical method was 2.23 s, which is significantly shorter than during GMAW.

The electron beam welding process offer significant productivity, since the the high number of weld passes (7-9 passes depending on the heat input) can be avoided at the same thickness due to the high penetration and welding speed. The use of filler material is also eliminated altogether in the case of single-pass autogenous EBW process. A clear advantage, that the same strength and toughness level welded joint could be prepared with EBW as with GMAW without the application of alloyed filler material. Although, the hardness of the weld and HAZ was found to be near to the permitted 450 HV10 value, it does not cause higher cold cracking sensitivity due to the lack of hydrogen thanks to the high vacuum. Based on the performed FCG investigations the S960QL EB welded joints have shown lower FCG resistance as compared to S960QL GMA welded joint. In case of S960M, with application of EBW process, the tensile strength of EBW welded joint also reached the level of BM. EBW resulted higher average hardness in HAZ than FZ, the highest hardness observed in FGHAZ while a local reduction in hardness observed in CGHAZ, however it also reaches the level of BM. The S960M EB welded joints shown higher FCG resistance than S960QL EB welded joint. FCG resistance varies in relation to the notch direction in comparison to the GMA welded joint. However, in case of notch incised in weld metal, it can be concluded, that the tendency of the FCG resistance of EBW & GMAW are not the same at the investigated Q+T and TMCP steels. Therefore, the statistical based qualification of the differences requires further tests.

Based on the residual stress investigations it was found that the S960M exhibits more compressive stress than S960QL near the weld toe and for HAZ it follows nearly the same pattern for both steels. The maximum tensile stress experienced in EB welded joints are in longitudinal direction since this direction subjected to highest contraction as a result of the welding thermal cycle. The magnitude of tensile stress near toe of S960QL joint was maximum (60% of the yield strength of the BM) compared to S960M joint (55% of the yield strength of the BM). In the case with autogenous EBW, due to the smaller linear heat input, the shrinkage process especially the phase transformation leads to the reduction of the tensile RS and also the compressive RS resulting in the characteristic “W-shape” of RS distribution.

DOI: 10.14750/ME.2021.051

11. APPLICATION POSSIBILITIES OF THE RESULTS

There is an increasing demand, especially in the vehicle industry for the application of high strength steels. HSSs are achieved by a varying micro alloying elements and special manufacturing technology that results in a special, complex microstructure. As a result, the main challenges for development engineers and researchers to understand the weldability of these HSSs with application of various welding technological processes, including conventional and high energy beam welding processes to take up technological advancement and benefits of it. The extensive experimental work and the gained achievement of present dissertation from material, technology and design perspectives, can contribute to the wider spread of high strength steels in the industry.

Related to DP steels the gained experiences during the physical simulation of HAZ and real welding experiments provide opportunity to study the weldability of newly developed high-strength steels. The results presented in the dissertation provide important information not only for welding professionals but also for material engineers involved in steel development.

The application of diode LBW process for various grades of DP steels and the effect of PWHT provide the detailed information about the mechanical properties and the microstructural changes, which may provide a basis for the development of new types of steels. The comparison of $t_{8/5}$ cooling time by analytical and experimental methods can contribute to the more accurate predictions of the properties of the weld. The application of diode lasers in fusion welding can be considered as a relatively new area, however the welding and PWHT can be performed by the same equipment due to the widely adjustable spot diameter. This property could be effectively utilized in the examined DP steels, however this methodology can be also beneficial for other types of high strength steels having even higher hardenability. PWHT had clearly a beneficial effect in terms of the cold cracking sensitivity and residual stresses, therefore its application should be in focus related to high strength steel welds.

The application of power beam processes for the HSSs (S960QL & S960M) has clearly an industrial significance. Practical guides and tips for welding these steels with conventional arc welding process are already available in many cases, however, sufficient information is not yet available on the effects of lower welding heat input (EBW process), dynamic and fatigue behavior of welded joints made of these steels. Therefore, the basic aim of the present dissertation is to summarize knowledge that will also provide useful information to industry professionals. These results will help the engineers/technologists and users of HSS for the application of research data and can be implemented in the production of cranes and vehicles (trucks, trailers etc.). In this dissertation, applicability of the electron beam welding for two types of HSSs were presented which will have significant contribution in reducing the HAZ, weld zone, full-penetration in thicker plate without filler materials, good strength, reduced brittle zones, higher speed, better quality, higher production time, reduced material wastage etc. as compared to the conventional arc welding processes. Electron beam welding is considered to be

DOI: 10.14750/ME.2021.051

the most promising welding method for the structural fabrication, thick material welding etc. as the micro-structural properties of the produced weld are outstanding and the faster processing times are favourable to conventional arc welding techniques. By EBW process, the tensile strength of the EB welded joints can reach the level of BM without the application of filler metal and similar toughness can be achieved as by GMAW. Although in the near future primarily the application of LBW is predictable in this sector, the EBW experimental results can be partially transmissible to the application of LBW on the same grades with keyhole technique due to the similar weld and HAZ structure. It is worth noting that during performed instrumented impact tests, the specimens, which far exceeded the 27 J & 40 J impact work required at -40 ºC for S960QL & S960M respectively, also behaved basically a brittle fracture with low amount of ductile parts, in accordance with literature. The absorbed energy during the fracture mostly included the energy for crack initiation which is generally high, even during brittle behaviour, due to the high tensile strength of the investigated HSSs. Consequently, it is worth critically considering to increase the present 27 J requirement in these high strength steels.

The FCG analysis results of the two different grades of HSSs welded joint using EBW process and its comparison with previously performed work by the different researchers on GMAW welded joint for the same grade of HSSs provided the deep insight into critical investigation and characteristic influence on the FCG resistance. The obtained results provide useful information to the researcher and as well as engineers designing the welded structures and can be applied for future applications and research.

Miskolc, Hungary, 02nd July, 2021

Raghawendra Pratap Singh Sisodia
Mechanical Engineering (Production) (ME)
Mechanical Engineering (CAD/CAM) (MSc)
International Welding Engineer/European Welding Engineer (IWE/EWE)

DOI: 10.14750/ME.2021.051

ACKNOWLEDGEMENTS

I would especially like to express my deepest gratitude to my supervisor, Dr. Marcell Gáspár, associate professor, Institute of Materials Science and Technology for his input, direction, expert guidance, mentorship, support throughout the course of this study and continuous encouragement during all stages of PhD study. His help in the form of valuable information, expert opinion and fruitful suggestion has brought life in this dissertation and also in research papers and in making this dissertation a success. I feel lucky to get an opportunity to work with him. Not only understanding the subject, but also interpreting the results drawn thereon from the experiment was much thought provoking, as it helped me morally to complete the work.

As a supervisor, he is always ready and willing to help his students to achieve their career goals and considers his students success as his great happiness. I have learned a great deal from him, which is so important for me to become an independent, critical thinking researcher beyond my school life.

I owe my sincere thanks to Prof. Dr. Lukács Janos, director, Institute of Materials Science and Technology, University of Miskolc for his invaluable support, suggestion and guidance in my research activities especially in performing fatigue crack growth experiments and result evaluation. Prof. Lukács has always been helpful and supportive and gave me the best support I required during my PhD study and research.

I would like to thank Prof. Dr. Miklós Tisza, who, as previous head of the István Sályi Doctoral School of Mechanical Sciences, he taught me “Fundamentals of Materials Science during the 1st semester of PhD study.

I extend my heartiest thank to the current head of the István Sályi Doctoral School of Mechanical Sciences Prof. Dr. Gabriella Vadászné Bognár for her kind support and guidance at every stage of my PhD studies.

I am extremely thankful to Dr. Andras Molnar honorary associate professor for his consistent help and valuable guidance, provided several study materials related to laser beam welding.

Cooperation with industry had an important role in this dissertation and I would like to thank and express my deep appreciation to Steigerwald Strahltechnik GmbH, Maisach, Germany (www.sst-ebeam.com) for the production of electron beam welded joints and Mr. Timcsák István, sales manager, IGM Robot Systems Ltd., Hungary for his contribution and organising EBW experiments.

I would like to acknowledge and express my deep appreciation to the Budai Benefit Ltd., Halásztelek, Hungary for their generous cooperation in the production of the laser welded joints used in this research. I would also like to thank the engineers of Budai Benefit Ltd. for their willingness to share their knowledge and extending their assistance in performing laser beam welding experimental tasks. I would like to thank Mr. László Draskóczi, technical director, Budai Benefit Ltd., for his precious time, guidance, technical know-how support, basic training

DOI: 10.14750/ME.2021.051

and for providing me the greater freedom with broader vision in the field of diode laser beam welding system and organizing the laser experiments.

I thank Mr. Róbert Pető, head of Welding Division, Voestalpine High Performance Metals Hungary Ltd. for their assistance and helps in providing with the filler material for laser welding experiments.

I want to express my utmost gratitude to Prof. Dr. Valéria Mertinger, head of the Institute of Physical Metallurgy, Metal Forming and Nanotechnology, University of Miskolc, for providing me the opportunity to perform SEM, XRD residual measurement at 3D lab and constantly supporting me through her valuable guidance, fruitful suggestion and evaluation of residual stress measurement results.

I would like to express my sincere and heartiest gratitude to Dr. Zoltán Siménfalvi, dean, Faculty of Mechanical Engineering and Informatics, for his support and help. I would like to extend my gratitude to the Faculty coordinator Dr. László Kovács and Dr. Samad Dadvandipour. I would like to express my special appreciation to Dr. Krisztián Hriczó for his help. Also, I would like to express my sincere thanks to Dr. Katalin Voith, senior research fellow, Ms. Emese Homonnai and Ms. Edit Gárdosi, Faculty administrator of the PhD students, Faculty of Mechanical Engineering and Informatics.

I offer my sincere thanks to the director of International Relation Office (IRO), Ms. Krisztina Sandor; Institutional Coordinator, Stipendium Hungaricum program, Ms. Krisztina Erdősi Mádainé and IRO student advisors, Ms. Katalin Gergely Csiréné & Ms. Nikolett Tóth for their cooperation, constant support, help during my PhD studies at the University of Miskolc, which will always in my heart forever and unforgettable.

Thanks to every faculty for instructing the courses I have taken during PhD course especially to Prof. Lukács Janos, Prof. Emeritus György Szeidl, Prof. Balogh Andras, Prof. Jenő Szigeti, Dr. Judit Makó, Prof. Péter Varga, Dr. Marcell Gáspár and from whom I learned so much.

I would also like to express my gratitude to all the colleagues and staff members of the Institute of Materials Science and Technology for their continuous support and help.

I would like to thanks to the institute administrative official, Mrs. Szegeczki Tiborné and Ms. Kőmíves Mariann for their sincere help in the departmental related offical work.

I would like to extend my sincerest thank to lab staff Mr. László Szentpéteri for his help in conducting tensile, bending test and long, tedious fatigue crack grow tests and special thanks are due to Mr. Géza Csukás for his assistance and help in performing instrumented Charpy V-notch impact tests and cooling time measurements with LBW using spider 8 instrument. Also, I would like to thanks Mr. Béla Fodor for his help and support in cooling time measurement with LBW.

I particularly wish to thank Mr. Kovács Árpád and Mrs. Agnes Csurillane Balogh, Metallurgical Lab, for their help and assistance in performing the SEM and optical microscopy & microhardness tests respectively.

Thanks are due to the noted technical staff, Mr. Kecskés Kristóf Sándor, Mr. András Petrovics, and Mr. Bartók András welding workshop who have contributed in many ways, their kind cooperation and helping hand in sample preparation for physical simulation, electron beam welding and laser beam welding experiments.

Thanks go to all past and present fellow graduate international students of University of Miskolc that I have had the pleasure of working with and their support. I could not have completed this long journey without their friendship, knowledge and discussions. I would also like to thanks Manoj Kumar Pal for his support and help.

DOI: 10.14750/ME.2021.051

Furthermore, I would like to thank my colleagues Péter Jámbor & Veres Zsombor at the Welding Research Group for their sincere help in organising sample cutting, all my classmate for their consistent help and support throughout my years of study and elsewhere who have in one way or another been involved in this dissertation.

It is my privilege to express my gratitude and respect to all of the people who mentored, guided, inspired and helped me during my course of study at the University of Miskolc.

I would like to acknowledge the support that I received for my doctoral studies through the Bilateral state scholarship program between University Grants Commission (UGC), Ministry of Education, Govt. of India and the Tempus Public Foundation, Govt. of Hungary. I am extremely grateful to the Stipendium Hungaricum Scholarship program for giving me this golden opportunity to pursue my PhD studies at the University of Miskolc, Miskolc, Hungary and helping to fulfil my dream with financial support covering all expenses (academic course fee, living allowances, stipend etc.) which boosted my self-confidence.

My acknowledgement would be incomplete without thanking the biggest source of my strength, my family. The blessings of my late parents and the constant love, care and unending support of my brothers and sister. Thanks to my brothers for their guidance, encouragement, inspiration, always being patient and supportive to me during this long but fruitful journey of my studies and preparation of PhD dissertation.

I would like to acknowledge the projects that supported the base materials purchase and publication. The present research work based on the results achieved within the TÁMOP-4.2.2/A-11/1-KONV-2012-0029 project realized in the framework of the New Széchenyi Plan. The experimental work could not be performed without the high strength steels base material purchasement of this project.

This research was supported by the European Union and the Hungarian State, co-financed by the European Regional Development Fund in the framework of the GINOP-2.3.4-15-2016-00004 project, aimed to promote the co-operation between the higher education and the industry.

DOI: 10.14750/ME.2021.051

REFERENCES

[1] S. Błacha, M.S. Węglowski, S. Dymek, M. Kopuściański: *Microstructural and mechanical characterization of electron beam welded joints of high strength S960QL and WELDOX 1300 steel grades*, Archives of Metallurgy and Materials, . Vol. 62, pp. 627–634, 2017. https://doi.org/10.1515/amm-2017-0092.

[2] K. Zsuzsanna, Gy. Nagy, J. Lukács: *COD assessment of S960M grade steel at different temperatures*, in: 72nd IIW Annual Assembly and International Conference: Proceedings of International Conference, IIW-DOC X-1958-19, 2019.

[3] M. Eshraghi, M.A. Tschopp, M.A. Zaeem, S.D. Felicelli: *A parametric study of resistance spot welding of dual-phase steel using finite element analysis*, in: Proceedings of the 8th Pacific Rim International Congress on Advanced Materials and Processing, Springer, pp. 3073–3074, 2013. https://doi.org/10.1007/978-3-319-48764-9_379.

[4] A. Wrożyna, M. Pernach, R. Kuziak, M. Pietrzyk: *Experimental and Numerical Simulations of Phase Transformations Occurring During Continuous Annealing of DP Steel Strips*, Journal of Materials Engineering and Performance. Vol. 25, pp. 1481–1491, 2016. https://doi.org/10.1007/s11665-016-1907-9.

[5] Á. Dobosy, J. Lukács: *Welding properties and fatigue resistance of S690QL high strength steels*, Materials Science Forum. Vol. 812, pp. 29–34, 2015. https://doi.org/10.4028/www.scientific.net/MSF.812.29.

[6] G.C.C. Correard, G.P. Miranda, M.S.F. Lima: *Development of laser beam welding of advanced high-strength steels*, International Journal of Advanced Manufacturing Technology, Vol. 83, pp. 1967–1977, 2016. https://doi.org/10.1007/s00170-015-7701-2.

[7] F. Schröter: *Trends of using high-strength steel for heavy steel structures*. https://doi.org/https://www.dillinger.de/d/downloads/download/7916 (accessed March 23, 2021).

[8] M.S. Węglowski, S. Błacha, A. Phillips: *Electron beam welding - Techniques and trends* - Review, Vacuum, Vol. 130 pp. 72–92, 2016. https://doi.org/10.1016/j.vacuum.2016.05.004.

[9] Nuclear science abstract, 1969, *Air space frontiers challenge welding*, Weld. Eng. Vol. 54, pp. 39–44, 1969.

[10] J. Svenungsson, I. Choquet, A.F.H. Kaplan: *Laser Welding Process - A Review of Keyhole Welding Modelling*, Physics Procedia, Vol. 78, pp. 182–191, 2015. https://doi.org/10.1016/j.phpro.2015.11.042.

[11] M. Sága, M. Blatnická, M. Blatnickỳ, J. Dižo, J. Gerlici: *Research of the fatigue life of welded joints of high strength steel S960QL created using laser and electron beams*, Materials, Vol. 13, 2020. https://doi.org/10.3390/ma13112539.

[12] L. Kuzsella, J. Lukács, K. Szűcs: *Nil-Strength Temperature and Hot Tensile Tests on S960QL High-Strength Low-Alloy Steel*, Production Processes and Systems, Vol. 6, pp. 67–78, 2013.

[13] F. Schröter: *Steels for modern steel construction and offshore applications*, in: 10th Nordic Steel Construction Conference, Copenhagen, pp. 13–24, 2004.

DOI: 10.14750/ME.2021.051

[14] M. Gáspár: *Physical simulation based development of welding technology for quenched and tempered structural high strength steels*, PhD Thesis, István Sályi Doctoral School of Mechanical Engineering Sciences, University of Miskolc, Miskolc, Hungary, 2016 (In Hungarian).

[15] M. Gáspár, A. Balogh, J. Lukács: *Toughness examination of physically simulated S960QL HAZ by a special drilled specimen*, in: Vehicle and Automotive Engineering, Lecture Notes in Mechanical Engineering, Springer, pp. 469–489, 2017. https://doi.org/10.1007/978-3-319-51189-4_40.

[16] M.S. Węglowski: *Modern toughened steels – their properties and advantages*, Bulletin of the Institute of Welding, Vol. 2, pp. 25–36, 2012.

[17] E. Evin, M. Tomáš: *The influence of laser welding on the mechanical properties of dual phase and trip steels*, Metals, Vol. 7, 2017. https://doi.org/10.3390/met7070239.

[18] B. Varbai, C. Sommer, M. Szabó, T. Tóth, K. Májlinger: *Shear tension strength of resistant spot welded ultra high strength steels*, Thin-Walled Structures, Vol. 142, pp. 64–73. 2019. https://doi.org/10.1016/j.tws.2019.04.051.

[19] E. Javaheri, J. Lubritz, B. Graf, M. Rethmeier: *Mechanical properties characterization of welded automotive steels*, Metals, Vol. 10, pp. 1–20, 2020. https://doi.org/10.3390/met10010001.

[20] N. Farabi, D. L. Chen, J. Li, Y. Zhou, S.J. Dong: *Microstructure and mechanical properties of laser welded DP600 steel joints*, Materials Science and Engineering A, Vol. 527, pp. 1215–1222, 2010. https://doi.org/10.1016/j.msea.2009.09.051.

[21] P.H.O.M. Alves, M.S.F. Lima, D. Raabe, H.R.Z. Sandim: *Laser beam welding of dual-phase DP1000 steel*, Journal of Materials Processing Tech, Vol. 252, pp. 498–510, 2018. https://doi.org/10.1016/j.jmatprotec.2017.10.008.

[22] K. Bandyopadhyay, S. K. Panda, P. Saha: *Optimization of fiber laser welding of DP980 steels using RSM to improve weld properties for formability*, Journal of Materials Engineering and Performance, Vol. 25, pp. 2462–2477, 2016. https://doi.org/10.1007/s11665-016-2071-y.

[23] K. Bandyopadhyay, S.K. Panda, P. Saha, V.H. Baltazar-Hernandez, Y.N. Zhou: Microstructures and failure analyses of DP980 laser welded blanks in formability context, Materials Science and Engineering A, Vol. 652, pp. 250–263, 2016. https://doi.org/10.1016/j.msea.2015.11.091.

[24] E. Biro, J. R. McDermid, J. D. Embury, Y. Zhou: *Softening kinetics in the subcritical heat-affected zone of dual-phase steel welds*, Metallurgical and Materials Transactions A: Physical Metallurgy and Materials Science, Vol. 41, pp. 2348–2356, 2010. https://doi.org/10.1007/s11661-010-0323-2.

[25] J. Wang, L. Yang, M. Sun, T. Liu, H. Li: *Effect of energy input on the microstructure and properties of butt joints in DP1000 steel laser welding*, Materials and Design, Vol. 90, pp. 642–649, 2016. https://doi.org/10.1016/j.matdes.2015.11.006.

[26] A. Klimpel, D. Janicki, A. Lisiecki, Z. Wilk: *Laser welding technologies: High power diode laser application examples*, Welding International. Vol. 24, pp. 689–698, 2010. https://doi.org/10.1080/09507111003655077.

[27] P. J. Withers, H. K. D. H. Bhadeshia: *Residual stress Part 2 – Nature and origins*, Materials Science and Technology, Vol. 17, pp. 366–375, 2001. https://doi.org/10.1016/s0160-4120(16)30771-1.

[28] P. J. Withers, H. K. D. H. Bhadeshia: *Residual stress. Part 1– Measurement techniques*, Materials Science and Technology, Vol. 17, pp. 366–375, 2001. https://doi.org/10.1179/026708301101510087.

[29] K. Easterling: *Introduction to the Physical Metallurgy of Welding*, 2nd ed., Butterworth-Heinemann, 1992. ISBN: 9781483141664.

DOI: 10.14750/ME.2021.051

[30] N. Bailey, F. R. Coe, T.G. Gooch, P. H .M. Hart, N. Jenkins, R. J. Pargeter: *Welding steels without hydrogen cracking*, 2nd ed., Woodhead Publishing Limited, 1993. (ISBN; 978-1-85573-014-4)

[31] J.Wartiainen, *Residual stress in Welding*, https://www.stresstech.com/Bulletin_15_Residual_Stress_in_Welding, pp. 1–4. (accessed April 21, 2021).

[32] M. Junaid, F. N. Khan, N. Baksh, M. N. Baig, K. Rahman: *Study of microstructure, mechanical properties and residual stresses in full penetration electron beam welded Ti-5Al-2.5Sn alloy sheet*, Materials and Design, Vol. 139, pp. 198–211, 2018. https://doi.org/10.1016/j.matdes.2017.11.009.

[33] C. M. Sonsino: *Effect of residual stresses on the fatigue behaviour of welded joints depending on loading conditions and weld geometry*, International Journal of Fatigue, Vol. 31, pp. 88–101, 2009. https://doi.org/https://doi.org/10.1016/j.ijfatigue.2008.02.015.

[34] L. Suominen, M. Khurshid, J. Parantainen: *Residual stresses in welded components following post-weld treatment methods*, Procedia Engineering,Vol. 66, pp. 181–191, 2013. https://doi.org/10.1016/j.proeng.2013.12.073.

[35] B. A. Burgan, M. R. Sansom: *Sustainable steel construction*, Journal of Constructional Steel Research. Vol. 62, pp. 1178–1183, 2006. https://doi.org/10.1016/j.jcsr.2006.06.029.

[36] Zs. Lukács: *Modeling and testing of the springback of high-strength steels*, PhD Thesis, István Sályi Doctoral School of Mechanical Engineering Sciences, University of Miskolc, Miskolc, Hungary, 2014 (In Hungarian).

[37] L. Szunyogh et al.: *Welding and related technologies*, Handbook, Mechanical Engineering Scientific Association, Budapest, 2007.

[38] M. Tisza: *Advanced materials in sheet metal forming*, Key Engineering Materials. Vol. 581 pp. 137–142, 2014. https://doi.org/10.4028/www.scientific.net/KEM.581.137.

[39] M. Tisza: *Material Developments in Sheet Metal Forming*, Production Processes and Systems. Vol. 6, pp. 79–88, 2013.

[40] G. A. Kunitsyn, S. V. Denisov, A. V. Gorbunov, A.G. Vetrenko, A.I. Brus'Yanina, E. V. Zharkov: *Production of high-strength steel sheet for the auto industry*, Steel in Translation, Vol. 38, pp. 585–588, 2008. https://doi.org/10.3103/S0967091208070231.

[41] S. Keeler, M. Kimchi, P.J. Mooney: *Advanced High-Strength Steels Guidelines Version 6.0*, WorldAutoSteel, 2017. 314. https://www.worldautosteel.org/projects/advanced-high-strength-steel-application-guidelines/. (accessed April 21, 2021).

[42] A. Romeijn: *Steel Bridges, Part 1*, TU Delft, 2006.

[43] R. Rudolf, S. Ronald: *The world's first system for high-strength welded structures*, Alform welding system, Voestalpine, pp. 1–47, 2012.

[44] Voestalpine, *S960M Application*, https://www.voestalpine.com/alform/en/Applications/Machinery-Industry (accessed March 18, 2021).

[45] D.T. Fossl: *Implementation "alform welding system"* presentation, in: Konrad Forsttechnik GmbH, www. forsttechnik.at, Linz, Austria, 2012.

[46] SSAB: *DP1200 & DP1400M application with car*. https://www.ssab.com/products/brands/docol/products/martensitic-steel (accessed March 18, 2021).

[47] N. Fonstein: *Dual-phase steels*, 2016. https://doi.org/10.1016/B978-0-08-100638-2.00007-9.

[48] Alform: *Applications*. https://www.voestalpine.com/alform/en/Products/x-treme (accessed March 18, 2021).

[49] M. Pirinen: *The effects of welding heat input on the usability of high strength steels in welded structures*, PhD Thesis, Lappeenranta University of Technology, Lappeenranta,

Finland, 2013. ISBN: 978-952-265-400-7.
[50] H. F. H. Mobark: *Fatigue Strength and Fatigue Crack Propagation Design Curves for High Strength Steel Structural elements*, PhD Thesis, University of Miskolc, Miskolc, Hungary, 2020.
[51] R.N. Jha, K. Dutta, K.K. Ray: *Effect of tempering on mechanical properties of V-added AISI 4335 steel*, ISIJ International, Vol. 50 pp. 607–612, 2010. https://doi.org/10.2355/isijinternational.50.607.
[52] Z. Shi, K. Liu, M. Wang, J. Shi, H. Dong, J. Pu, B. Chi, Y. Zhang, L. Jian: *Effect of tensile deformation of austenite on the morphology and strength of lath martensite*, Metals and Materials International, Vol. 18, pp. 317–320, 2012. https://doi.org/10.1007/s12540-012-2015-5.
[53] F. Zhen, K. Zhang, Z. L. Guo, J. B. Qu: *Effect of Martensite Fine Structure on Mechanical Properties of an 1100 MPa Grade Ultra-high Strength Steel*, Journal of Iron and Steel Research International, Vol. 22, pp. 645–651, 2015. https://doi.org/10.1016/S1006-706X(15)30052-2.
[54] C. Wang, M. Wang, J. Shi, W. Hui, H. Dong: *Effect of microstructural refinement on the toughness of low carbon martensitic steel*, Scripta Materialia. Vol. 58, pp. 492–495, 2008. https://doi.org/10.1016/j.scriptamat.2007.10.053.
[55] D. A. Porter: *Weldable high-strength steels: challenges and engineering applications*, in: IIW Int. Conf. on High Strength Steels – Challenges and Applications, Helsinki, Finland, 2015.
[56] M. Klein, M. Sonnleitner, P. Stiaszny: *Alform_ x-treme innovation*, in: 1st Alform_ Welding Day, Linz, Austria, 2012.
[57] SSAB: *The ultra-high-strength steel at 1300 MPa*, www.ssab.com/products/brands/strenx/products/strenx-1300 (accessed January 31, 2021).
[58] Dillinger: *High, extra-high and ultra-high-strength quenched and tempered fine grained structural steels*, https://www.dillinger.de/d/en/products/heavyplate/highstrength-finegrained/index.shtml (accessed January 31, 2021).
[59] Voestalpine: *Ultra-high-strength cut-to-length sheets made of hot-rolled steel strip*, https://www.voestalpine.com/alform/en/Products/x-treme (accessed January 31, 2021).
[60] S. Błacha, M.S. Węglowski, S. Dymek, M. Kopuściański: *Microstructural characterization and mechanical properties of electron beam welded joint of high strength steel grade S690QL*, Archives of Metallurgy and Materials, Vol. 61, pp. 1193–1200, 2016. https://doi.org/10.1515/amm-2016-0198.
[61] P. Seyffarth, R. Schmidt, W.F. Demtschenko, U. Jasnau: *Simulation of microstructure – transformation – kinetics of unalloyed constructional steel in case of fast thermal cycles*, in: Proceedings of the 3rd LANE, Meisenbach Verlag, Bamberg, 2001.
[62] M. Gaspar, A. Balogh: *GMAW experiments for advanced (Q+T) high strength steels*, Production Process and System, Vol. 6, pp. 9–24, 2013.
[63] J. Kömi: *Hot-rolled ultra-high strength steels*, in: Ruukki Metals, Raahe, Finland, 2011.
[64] M. S. Węglowski, W. Osuch, G. Michta: *Microstructure and mechanical properties of ultra-high strength steel Weldox 1300*, Inżynieria Materiałowa. Vol. NR3, pp. 205–208, 2013.
[65] ISO/EN 10025-6+A1: *Hot rolled products of structural steels Part 6: Technical delivery conditions for refined flat products made of high-yield structural steels*, 2009.
[66] R. Willms: *High strength steel for steel constructions*, Nordic Steel Construction Conference. pp. 597–604, 2009.
[67] D. Raabe: *Dual Phase steels*, http://www.dierk-raabe.com/dual-phase-steels/ (accessed February 1, 2021).
[68] R.W. K. Bhadesia, H. K. D. H., Honeycombe: *Steels Microstructure and Properties*, 3rd

DOI: 10.14750/ME.2021.051

ed., Elsevier Linacre House, Jordan Hill, Oxford OX2 8DP, 2006. ISBN: 9780080462929

[69] Y. Weng: *Ultra-fine grained steels*, Springer, Berlin, Heidelberg, 2009. https://doi.org/10.1007/978-3-540-77230-9.

[70] M. Klein, H. Spindler, A. Luger, R. Rauch, P. Stiaszny, M. Eigelsberger: *Thermomechanically Hot Rolled High and Ultra High Strength Steel Grades - Processing, Properties and Application*, Materials Science Forum. pp. 543–550, 2005. https://doi.org/10.4028/www.scientific.net/msf.500-501.543.

[71] H. Spindler, M. Klein, R. Rauch, A. Pichler, P. Stiaszny: *High strength and ultra high strength hot rolled steel grades – products for advanced applications*, in: Super High Strength Steels (SHSS): International Conference, Rome, 2005.

[72] Voestalpine: *High-strength heavy plates: High-strength heavy plates enable weight savings and optimum weldability*, https://www.voestalpine.com/stahl/Gesellschaften/voestalpine-Grobblech-GmbH/Produkte/Grobbleche/Hochfeste-Grobbleche (accessed April 8, 2021).

[73] B. Hechler, O. Axmann, G. Donnay: *The rigth choice of steel - According to the Eurocode, Economical bridge solutions based on innovative composite dowels and integrated abutments*, in: Springer Vieweg, pp.1–169, 2015. https://doi.org/10.1007/978-3-658-06417-4.

[74] N. Shikanai, S. Mitao, S. Endo: *Recent development in microstructural control technologies through the thermo-mechanical control process (TMCP) with JFE Steel's high-performance plates*, JFE Technical Report. 11, pp. 1–6, 2008.

[75] Commission of the European Communities: *High strength structural steels: A European review*, Vol. 1, pp. 218, 1988.

[76] M. Weglowski: *High strength quenched and tempered steels: Weldability and welding*, in: Nova science publishers, Inc, 2018.

[77] M. S. Weglowski, M. Zeman: *Prevention of cold cracking in ultra-high strength steel Weldox 1300*, Archives of Civil and Mechanical Engineering, Vol. 14, pp. 417–424, 2014. https://doi.org/10.1016/j.acme.2013.10.010.

[78] P. Hansson: *Control of weldability - Research leading to the development of two new quenched and tempered tool steels*, Dissertation, Royal Institute of Technology, Stockholm, pp. 47, 2004. (ISSN:1650-1888)

[79] Metals Handbook, Vol. 6: *Welding, Brazing, and Soldering*, ASM International, USA, 1995.

[80] A. Balogh, J. Sárvári, J. Schäffer, M. Tisza: *Mechanical Technologies*, pp. 270, 4th ed., Miskolc University Press, Miskolc, Hungary.

[81] P. Romvári: *Welding technology. Part I. Welding is physical and metallurgical basics*, Textbook publisher, Budapest, Hungary, 1980.

[82] D. A. Porter, K. E. Easterling, M. Y. Sherif: *Phase transformations in metals and alloys*, 3rd ed., CRC Press, Taylor & Francis group, 2009. ISBN: 978-1-4398-8357-0

[83] P. Nevasmaa: *Evaluation of HAZ Toughness Properties in Modern Low Carbon Low Impurity 420, 550 and 700 MPa Yield Strength Thermomechanically Processed Steels with Emphasis on Local Brittle Zones*, Lisensiaatintyö, University of Oulu, Oulu, Finland, 1996.

[84] P. Nevasmaa: *Predictive model for the prevention of weld metal hydrogen cracking in high-strength multipass welds*, Academic Dissertation, University of Oulu, Oulu, Finland, 2003. (http://herkules.oulu.fi/isbn9514271815/), ISBN: 951-42-7181-5.

[85] L. Prém: *The influence of technology on high-strength DP steels is spot welded the structure of its bonds*, in: 27th Welding Conference, pp. 1-16, University of Óbuda, Budapest, Hungary, 2014.

[86] R. P. S. Sisodia: *Comparative analysis about the weldability of Q+T and TMCP steels by*

DOI: 10.14750/ME.2021.051

physical simulation, MSc Thesis, University of Miskolc, Miskolc, Hungary, 2017.
[87] M. Opiela: *Hydrogen embrittlement of welded joints for the heat-treatable XABO 960 steel heavy plates*, Journal of Achievements in Materials and Manufacturing Engineering, Vol. 38, pp. 41–48, 2010.
[88] M. Lachowicz, W. Nosko: *Welding of structural steel Weldox 700*, Welding Technology Review. Vol. 82, pp. 13–18, 2010.
[89] M. Fukuhisa, P. Bernasovsky: *An investigation on the behaviour of M-A constituent in simulated HAZ of HSLA steels*, Doc. IX-1591-98, in: International Institute of Welding., 1998.
[90] E. Tasak: *Weldability of steels*, Krakow, Fotobit, 2002.
[91] D. Dütta, J. Wardenier, N. Yeomans, K. Sakae, O. Bucak, J. A. Packer: *Design guide 7- For fabrication, assembly and erection of hollow section structures*, CIDECT, TÜV Verlag, 1998.
[92] Y. Nie, Y., C. J. Shang, Y. You, X. C. Li, J. P. Cao, X. L. He: *960 MPa Grade High Performance Weldable Structural Steel Plate Processed by Using TMCP*, Journal of Iron and Steel Research International, Vol. 17, pp. 63–66, 2010. https://doi.org/10.1016/S1006-706X(10)60061-1.
[93] D. Porter: *Development in hot-rolled high-strength steel*, in: Nordic Welding Conference, New Trends in Welding Technology, Tampere, Finland, 2006.
[94] K. Umekuni, A. Masubuchi: *Usefulness of Undermatched Welds for High Strength Steels*, Welding Journal, Vol. 76, pp. 256–263, 1997.
[95] M. Zeman: *Assessment of weldability of WELDOX 1100 high-strength quenched and tempered steel*, Welding International, Vol. 23, pp. 73–82, 2009. https://doi.org/10.1080/09507110802349122.
[96] J. Verwimp, J. Gedopt, G. Maes, W. V. Haver, *Hybrid Nd: Yag- Laser/GMAW Welding of Ultra High Strength Steel*, in: 12th NOLAMP Conference in Laser Processing of Materials, Copenhagen, Denmark, 2009.
[97] F. Hochhauser, W. Ernst, R. Rauch, R. Vallant, N. Enzinger: *Influence of the soft zone on the strength of welded modern HSLA steels*, Welding in the world, Vol. 56, pp. 77-85, 2012. https://doi.org/10.1007/BF03321352.
[98] Gleeble: *Physical simulation*, https://www.gleeble.com/resources/what-is-physical-simulation.html (accessed January 21, 2021).
[99] M. Dunder, I. Samardzic, G. Simunovic, P. Konjatic: *Steel weldability investigation by single and double-pass weld thermal cycle simulation*, International Journal of Simulation Modelling. Vol. 19, pp. 209–218, 2020. https://doi.org/10.2507/IJSIMM19-2-510.
[100] E. H. El-Shenawy: *Physical simulation technology for thermo-mechanical processing of metallic alloys using Gleeble system*, Materials Today: Proceedings. Vol. 28, pp. 998–1004, 2019. https://doi.org/10.1016/j.matpr.2019.12.339..
[101] C. D. Lundin, G. Zhou: *A comparison of published HAZ thermal simulation methods to derive weld HAZ thermal cycles*, Acta Metallurgica Sinica (English Letters), Vol. 13, pp. 223–232, 2000.
[102] Y. Adonyi: *Heat-affected zone characterization by physical simulations*, Welding Journal, pp. 42–47, 2006.
[103] D. Rosenthal: *Mathematical theory of heat distribution during welding and cutting*, Welding Research Supplement, pp. 220–234, 1941.
[104] N. Rykalin: *Teplovie processzi pri szvarke, Vüpuszk 2*, Izdatelsztvo Akademii Nauk SzSzSzR, Moscow, Vol. 56, 1953.
[105] M. Łomozik: *New methodology of testing phase transformations in structural steels in welding thermal cycle conditions*, Kovove Materialy, Vol. 50, pp. 97–105, 2012. https://doi.org/10.4149/km_2012_2_97.

[106] J. Wang, L. Yang, M. Sun, T. Liu, H. Li: *A study of the softening mechanisms of laser-welded DP1000 steel butt joints*, Materials and Design, Vol. 97, pp. 118–125, 2016. https://doi.org/10.1016/j.matdes.2016.02.071.
[107] Q. F. Wang, C. J. Shang, R. D. Fu, Y. N. Wang, W. Chen: *Physical simulation and metallurgical evaluation of heat-affected zone during laser welding of ultrafine grain steel*, Materials Science Forum, Vol. 475–479, pp. 2717–2720, 2005. https://doi.org/10.4028/www.scientific.net/msf.475-479.2717.
[108] R. Laitinen, D. A. Porter, L. P. Karjalainen, P. Leiviskä, J. Kömi: *Physical simulation for evaluating heat-affected zone toughness of high and ultra-high strength steels*, Materials Science Forum. Vol. 762, pp. 711–716, 2013. https://doi.org/10.4028/www.scientific.net/MSF.762.711.
[109] M. Gáspár: *Effect of welding heat input on simulated HAZ areas in S960QL High strength steel*, Metals, Vol. 9, 2019. https://doi.org/10.3390/met9111226.
[110] M. Mičian, J. Winczek, D. Harmaniak, R. Koňár, M. Gucwa, J. Moravec: *Physical simulation of individual heat-affected zones in S960MC steel*, Archives of Metallurgy and Materials. Vol. 66, pp. 81–89, 2021. https://doi.org/10.24425/amm.2021.134762.
[111] G. S. Schajer: *Practical residual stress measurement methods*, John Wiley & Sons Ltd, 2013. https://doi.org/10.1002/9781118402832.
[112] Y. Ueda, H. Murakawa, N. Ma: *Welding deformation and residual stress prevention*, Elsevier Inc., 2012. ISBN: 9780123948205
[113] P. Kapadia, C. Davies, T. Pirling, M. Hofmann, R. Wimpory, F. Hosseinzadeh, D. Dean, K. Nikbin: *Quantification of residual stresses in electron beam welded fracture mechanics specimens*, International Journal of Solids and Structures. Vol. 106–107, pp. 106–118, 2017. https://doi.org/10.1016/j.ijsolstr.2016.11.028.
[114] D. J. Smith, G. Zheng, P. R. Hurrell, C. M. Gill, B. M. E. Pellereau, K. Ayres, D. Goudar, E. Kingston: *Measured and predicted residual stresses in thick section electron beam welded steels*, International Journal of Pressure Vessels and Piping. Vol. 120–121, pp. 66–79, 2014. https://doi.org/10.1016/j.ijpvp.2014.05.001.
[115] P.V. Ramana, G.M. Reddy, T. Mohandas, A.V.S.S.K.S. Gupta: *Microstructure and residual stress distribution of similar and dissimilar electron beam welds – Maraging steel to medium alloy medium carbon steel*, Materials and Design, Vol. 31, pp. 749–760, 2010. https://doi.org/10.1016/j.matdes.2009.08.007.
[116] R.H. Leggatt: *Residual stresses in welded structures*, International Journal of Pressure Vessels and Piping, Vol. 85, pp. 144–151, 2008. https://doi.org/10.1016/j.ijpvp.2007.10.004.
[117] K. Masubuchi: *Analysis of welded structures*, Pergamon press, New York, 1980.
[118] BS7910:2013+A1:2015, British Standards Institution: *Guide to methods for assessing the acceptability of flaws in metallic structures*.
[119] H. J. Stone, P. J. Withers, S. M. Roberts, R. C. Reed, T. M. Holden: *Comparison of three different techniques for measuring the residual stresses in an electron beam-welded plate of WASPALOY*, Metallurgical and Materials Transactions A., Vol. 30, pp. 1797–1808, 1999. https://doi.org/10.1007/s11661-999-0178-6.
[120] T. Ślęzak, L. Śnieżek: *Properties of welded joints made in high strength steel using laser technology*, Bulletin of the Military University of Technology. Vol. 66, pp. 55–66, 2017. https://doi.org/10.5604/01.3001.0009.9484.
[121] T. Schaupp, D. Schröepfer, A. Kromm, T. Kannengiesser: *Welding residual stress distribution of quenched and tempered and thermo-mechanically hot rolled high strength steels*, Advanced Materials Research, Vol. 996, pp. 457–462, 2014. https://doi.org/10.4028/www.scientific.net/AMR.996.457.
[122] T. Schaupp, D. Schroepfer, A. Kromm, T. Kannengiesser: *Welding residual stresses in*

960 MPa grade QT and TMCP high-strength steels, Journal of Manufacturing Processes, Vol. 27, pp. 226–232, 2017. https://doi.org/10.1016/j.jmapro.2017.05.006.

[123] D. Schroepfer, A. Kromm, T. Schaupp, T. Kannengiesser: *Welding stress control in high-strength steel components using adapted heat control concepts*, Welding in the World, Vol. 63, pp. 647–661, 2019. https://doi.org/10.1007/s40194-018-00691-z.

[124] J. Hensel, T. Nitschke-Pagel, K. Dilger: *On the effects of austenite phase transformation on welding residual stresses in non-load carrying longitudinal welds*, Welding in the World, Vol. 59, pp. 179–190, 2014. https://doi.org/10.1007/s40194-014-0190-3.

[125] T. Nitschke-Pagel: *Recommendations for the measurement of residual stresses in welded joints by means of X-ray diffraction—results of the WG6-RR test*, Welding in the World, Vol. 65, pp. 589-600, 2020. https://doi.org/10.1007/s40194-020-01029-4.

[126] J. Lukács, Gy. Nagy, I. Harmati, R. Fótos, Zs. Koncsik: *Excerpts from engineering the integrity of structures*, in: Miskolc, 2012. ISBN 978-963-358-000-4

[127] D.W. Hoeppner, W.E. Krupp: *Prediction of component life by application of fatigue crack growth knowledge*, Engineering Fracture Mechanics. Vol. 6 pp. 47-62, 1974. https://doi.org/10.1016/0013-7944(74)90046-0.

[128] C.J. Hellier: *Handbook of Nondestructive Evaluation*, 2nd ed., McGraw-Hill Companies, Inc, 2013.

[129] A. Pickard: *Component lifting*, Materials Science and Technology, Vol. 3, pp. 743–749, 1987.

[130] J. Lukács: *Dimensions of Lifetime Management*, Materials Science Forum, Vol. 473–474, pp. 361–368, 2005. https://doi.org/10.4028/www.scientific.net/msf.473-474.361.

[131] J. Lukács: *Reliability of cyclic loaded welded joints having cracks*, CSc dissertation, Miskolc-Budapest, 1992.

[132] J. Lukács: *Structural integrity*, PhD lecture, 5th lecture, University of Miskolc, 2018.

[133] D. Broek: *The practical use of fracture mechanics*, Kluwer Academic Publishers, 1988.

[134] P. L. M. Klesnil: *Effect of stress cycle asymmetry on fatigue crack growth*, Materials Science and Engineering, Vol. 9, 1972.

[135] P. Paris, F. Erdogan: *A critical analysis of crack propagation laws*, Journal of Basic Engineering, Transactions of the ASME, Vol. 85, pp. 528–534, 1963.

[136] R. G. Forman, V. E. Kearney, R. M. Engle: *Numerical Analysis of Crack Propagation in Cyclic-Loaded Structures*, Journal of Basic Engineering, Vol. 89, pp. 459–463, 1967. https://doi.org/10.1115/1.3609637.

[137] R. I. Stephens, A. Fatemi, R. R. Stephens, H. O. Fuchs: *Metal Fatigue in Engineering*, 2nd ed., John Wiley & Sons, Inc., 2000. ISBN: 978-0-471-51059-8

[138] H. Naubereit, J. W. Weihert: *Einführung in die Ermüdungsfestigkei*, Carl Hanser Verlag, München - Wien, 1999.

[139] J. Lukács, Á. Dobosy: *Matching effect on fatigue crack growth behaviour of high-strength steels GMA welded joints*, Welding in the World, Vol. 63, pp. 1315–1327, 2019. https://doi.org/10.1007/s40194-019-00768-3.

[140] H. T. Li, X. D. Song*: Fatigue Crack Propagation Rate of High Strength Steel's Welded Joints*, 2nd Annual International Conference on Advanced Material Engineering, pp. 450–456, 2016. https://doi.org/10.2991/ame-16.2016.74.

[141] B. Varbai, K. Májlinger: *Physical and theoretical modeling of the nitrogen content of duplex stainless steel weld metal: Shielding gas composition and heat input effects*, Metals, Vol. 9, 2019. https://doi.org/10.3390/met9070762.

[142] J. Górka, A. Ozgowicz: *Structure and properties of laser beam welded joints of low alloy high strength steel DOCOL 1200M with a martensitic structure*, Materiali in Tehnologije/Materials and Technology, Vol. 52, pp. 189–193, 2018. https://doi.org/10.17222/mit.2017.077.

DOI: 10.14750/ME.2021.051

[143] W. Chen, P. Ackerson, P. Molian: *CO_2 laser welding of galvanized steel sheets using vent holes*, Materials and Design, Vol. 30, pp. 245–251, 2009. https://doi.org/10.1016/j.matdes.2008.05.009.
[144] LaserlineTechnical, *Laser basics*, BOC, A Memeber of Linde Group. https://www.boconline.ie/en/images/laser_basics_tcm674-78871.pdf (accessed May 11, 2021).
[145] S. Němeček, T. Mužík, M. Míšek: *Differences between Laser and Arc Welding of HSS Steels*, Physics Procedia, Vol. 39, pp. 67–74, 2012. https://doi.org/10.1016/j.phpro.2012.10.015.
[146] C.S. Wu, H.L. Wang, Y.M. Zhang: *Numerical analysis of the temperature profiles and weld dimension in high power direct-diode laser welding*, Computational Materials Science, Vol. 46, pp. 49–56, 2009. https://doi.org/10.1016/j.commatsci.2009.02.005.
[147] E. Kennedy, G. Byrne, D.N. Collins: *A review of the use of high power diode lasers in surface hardening*, Journal of Materials Processing Technology, Vol. 155–156, pp. 1855–1860, 2004. https://doi.org/10.1016/j.jmatprotec.2004.04.276.
[148] A. Lisiecki: *Study of optical properties of surface layers produced by laser surface melting and laser surface nitriding of titanium alloy*, Materials, Vol. 12, pp. 1–14, 2019. https://doi.org/10.3390/ma12193112.
[149] A. Lisiecki: *Titanium matrix composite Ti/TiN produced by diode laser gas nitriding*, Metals, Vol. 5, pp. 54–69, 2015. https://doi.org/10.3390/met5010054.
[150] N. Bailey: *Factors influencing weldability, in: Woodhead Publishing Series in Welding and Other Joining Technologies*, Woodhead Publishing, pp. 1–44, 1994. https://doi.org/10.1533/9781845698935.1.
[151] M. Moradi, M. Karamimoghadam: *High power diode laser surface hardening of AISI 4130 ; statistical modelling and optimization*, Optics and Laser Technology, Vol. 111, pp. 554–570, 2019. https://doi.org/10.1016/j.optlastec.2018.10.043.
[152] H. Pantsar, V. Kujanpää: *The absorption of a diode laser beam in laser surface hardening of a low alloy steel*, in: International Congress on Applications of Lasers & Electro-Optics (ICALEO®), pp. 185, 2018. https://doi.org/10.2351/1.5065721.
[153] S. J. Heikkilä, D. A. Porter, L. P. Karjalainen, R. O. Laitinen, S. A. Tihinen, P. P. Suikkanen: *Hardness profiles of quenched steel heat affected zones*, Materials Science Forum, Vol. 762, pp. 722–727, 2013. https://doi.org/10.4028/www.scientific.net/MSF.762.722.
[154] H. Tervo, S. Pallaspuro, A. Kaijalainen, D. Porter, J. Kömi, S. Mehtonen, T. Pikkarainen: *Detrimental effect of coarse Titanium-Niobium Nitrides on the fracture toughness of the CGHAZ in a 500 MPa offshore steel for cold climate conditions*, 10th International Conference on Clean Steel, Budapest, Hungary, 2018.
[155] H. Tervo, J. Mourujärvi, A. Kaijalainen, J. Kömi: *Mechanical properties in the physically simulated heat-affected zones of 500 MPa offshore steel for arctic conditions*, Lecture Notes in Mechanical Engineering, Springer, pp. 779–788, 2018. https://doi.org/10.1007/978-3-319-75677-6_66.
[156] L. Li: The a*dvances and characteristics of high-power diode laser materials processing*, Optics and Lasers in Engineering, Vol. 34, pp. 231-253, 2000. https://doi.org/10.1016/S0143-8166(00)00066-X.
[157] J. A. Alcock, B. Baufeld: *Diode laser welding of stainless steel 304L*, Journal of Materials Processing Techologies, Vol. 240, pp. 138–144, 2017. https://doi.org/10.1016/j.jmatprotec.2016.09.019.
[158] F. Bachmann: *Industrial applications of high power diode lasers in materials processing*, Applied Surface Science. Vol. 208–209, pp. 125–136, 2003. https://doi.org/10.1016/S0169-4332(02)01349-1.

DOI: 10.14750/ME.2021.051

[159] H. Staufer: *Laser hybrid welding for industrial applications*, in: XVI International Symposium on Gas Flow, Chemical Lasers, and High-Power Lasers, Vol. 634614, pp. 1–8, 2006. https://doi.org/10.1117/12.738144.
[160] Laserline: *High Power Diode Lasers*, https://www.laserlines.co.uk/wp-content/uploads/2019/03/Laserline_High_Power_Diode_Lasers.pdf (accessed April 27, 2020).
[161] K. Parker: *Welding with High Power Diode Lasers*, https://www.photonics.com/images/Web/WhitePapers/372/Welding_with_High_Power_Diode_Lasers.pdf (accessed January 27, 2021).
[162] Laserline: *Diode lasers and their applications – Part 1: The basics*, https://www.laserline.com/en-int/diode-laser/ (accessed May 1, 2020).
[163] A. Eltze: *Diode lasers enter new dimensions for metal welding*, in: Pacific International Conference on Applications of Lasers and Optics, 902, 2004. https://doi.org/10.2351/1.5056130.
[164] M. Shome, M. Tumuluru: *Welding and Joining of Advanced High Strength Steels (AHSS)*, Woodhead Publishing, 2015. https://doi.org/http://dx.doi.org/10.1016/B978-0-85709-436-0.00006-0.
[165] Y. Shi, P. Zhu, L. Shen, Z. Lin: *Lightweight design of automotive front side rails with TWB concept*, Thin-Walled Structures. Vol. 45, pp. 8–14, 2007. https://doi.org/10.1016/j.tws.2007.01.013.
[166] S. Katayama: *Handbook of laser welding technologies*, Woodhead Publishing Limited, 2013.
[167] Laserline: *Softening & Annealing of Materials*, https://www.laserline.com/en-int/softening/ (accessed April 27, 2020).
[168] A. Hesse, T. Nitschke-pagel, K. Dilger: *Fracture Toughness of Electron Beam Welded Fine Grain Steels*, Procedia Structural Integrity, Vol. 2, pp. 3523–3530, 2016. https://doi.org/10.1016/j.prostr.2016.06.439.
[169] X. He, X. Yang, G. Zhang, J. Li, H. Hu: *Quenching microstructure and properties of 300M ultra-high strength steel electron beam welded joints*, Materials and Design, Vol. 40, pp. 386–391, 2012. https://doi.org/10.1016/j.matdes.2012.04.010.
[170] C.M. Adams: *Phases and Processes*, *Electron beam welding*, Journal of Metals. 410 (1960).
[171] H. Schultz: *Electron beam welding*, Abington Publishing, Cambridge, 1993.
[172] T. Olshanskaya, V. Belenkiy, E. Fedoseeva, E. Koleva, D. Trushnikov: *Application of dynamic beam positioning for creating specified structures and properties of welded joints in electron-beam welding*, Materials, Vol. 13, 2233, 2020. https://doi.org/10.3390/ma13102233.
[173] S. Böhm: *The electron beam as a tool for joining technology*, DVS Media GmbH, Düsseldorf, pp. 1–100, 2014.
[174] O.K. Nazarenko: *Technological procedures of electron beam welding and repair*, *Materials and Manufacturing Processes*, Vol. 7, pp. 285–303, 1992. https://doi.org/10.1080/10426919208947416.
[175] J. Lukács: *Fatigue crack propagation limit curves for high strength steels based on two-stage relationship*, Engineering Failure Analysis, Vol. 103, pp. 431–442, 2019. https://doi.org/10.1016/j.engfailanal.2019.05.012.
[176] M. Sahul, M. Sahul, M. Haršáni, M. Dománková: *On the microstructure and mechanical properties of AW2099 aluminium lithium alloy joints produced with electron beam welding*, Materials Letters, Vol. 276, 128276, pp. 1-5, 2020. https://doi.org/10.1016/j.matlet.2020.128276.

DOI: 10.14750/ME.2021.051

[177] W. Maurer, W. Ernst, R. Rauch, S. Kapl, A. Pohl, T. Krüssel, R. Vallant, N. Enzinger: *Electron beam welding of a TMCP steel with 700 MPa yield strength*, Welding in the World, Vol. 56, pp. 85–94, 2012. https://doi.org/https://doi.org/10.1007/BF03321384.
[178] C.R. Das, A.K. Bhaduri, S. Raju, R. Balakrishnan, S. Mahadevan, S.K. Albert, P. Mastanaiah: *Influence of electron beam welding parameters on microstructure and Charpy impact properties of boron-added modified 9Cr-1Mo steel weld*, Welding in the World, Vol. 60, pp. 1141–1146, 2016. https://doi.org/10.1007/s40194-016-0369-x.
[179] L. Prém, Z. Bézi, A. Balogh, Development of Resistant Spot Welding Technology for Automotive Ferrite-Martensitic Dual-Phase Steels with Joint Application of Finite Element Modelling and Experimental Research, Advanced Materials Research. 1138 (2016) 43–48. https://doi.org/10.4028/www.scientific.net/amr.1138.43.
[180] Z. Wan, W. Guo, Q. Jia, L. Xu, P. Peng: *Hardness Evolution and High Temperature Mechanical Properties of Laser Welded DP980 Steel Joints*, High Temperature Materials and Processes. Vol. 37, pp. 587–595, 2018. https://doi.org/10.1515/htmp-2017-0007.
[181] G. Zhang, X. Yang, X. He, J. Li, H. Hu: *Enhancement of mechanical properties and failure mechanism of electron beam welded 300M ultrahigh strength steel joints*, Materials and Design, Vol. 45, pp. 56–66, 2013. https://doi.org/10.1016/j.matdes.2012.09.004.
[182] J. Górka, S. Błacha, D. Zagrobelny: *Electron Beam Welding of TMCP steel S700MC*, Biuletyn Instytutu Spawalnictwa, pp. 17–23, 2020. https://doi.org/10.17729/ebis.2020.4/1.
[183] L. Gyura, M. Gáspár, A. Balogh, The effect of flame straightening on the microstructure and mechanical properties of different strength steels, Welding in the World. 65 (2021) 543–560. https://doi.org/10.1007/s40194-020-01055-2.
[184] R. Laitinen: *Improvement of weld HAZ toughness at low heat input by controlling the distribution of MA constituents*, PhD Dissertation, University of Oulo, Oulu, Finland, 2006.
[185] A. Unt, A. Salminen: *Effect of welding parameters and the heat input on weld bead profile of laser welded T-joint in structural steel*, Journal of Laser Applications, Vol. 27, S29002, 2015. https://doi.org/10.2351/1.4906378.
[186] J. Górka: *Analysis of simulated welding thermal cycles S700MC using thermal imaging camera*, Advanced Materials Research. Vol. 837, pp. 375–380, 2014. https://doi.org/10.4028/www.scientific.net/AMR.837.375.
[187] A. Lisiecki: *Welding of thermomechanically rolled fine-grain steel by different types of lasers*, Archives of Metallurgy and Materials. Vol. 59, pp. 1625–1631, 2014. https://doi.org/10.2478/amm-2014-0276.
[188] E. Stanciu, G. Dumitru: *Laser welding parameters influence on the geometrical aspect of the melted zone in stainless steel*, U.P.B. Sci. Bull., Series D. 74, 2012.
[189] D. Schuöcker: *Handbook of the EuroLaser Academy*, Chapman & Hall, London, 1998.
[190] S. Kou: *Welding Metallurgy*, 2nd ed., A John Wiley & sons, Inc., 2002.
[191] D. Das, D. K. Pratihar, G. G. Roy: *Cooling rate predictions and its correlation with grain characteristics during electron beam welding of stainless steel*, International Journal of Advanced Manufacturing Technology. Vol. 97, pp. 2241–2254, 2018. https://doi.org/10.1007/s00170-018-2095-6.
[192] M. Sepsi, M. Salata, D. Cseh, V. Mertinger, M. Benke: *Significance of the residual stress monitoring in the automotive industry*, Springer International Publishing, 2018. https://doi.org/10.1007/978-3-319-75677-6_24.
[193] M.P. Berezhnyts'ka: *Methods for determining residual welding stresses and their relief (A review)*, Materials Science, Vol. 37, pp. 933–939, 2001. https://doi.org/10.1023/A:1015601525897.
[194] B. D. Cullity: *Elements of X-ray diffraction*, 2nd ed., Addison-Wesley, New York, 1978.

DOI: 10.14750/ME.2021.051

[195] B.K.H. Chan: *Software for welding engineers*, Thesis, Carleton University, Canada, 1990.
[196] W. Maurer, W. Ernst, R. Rauch, S. Kapl, A. Pohl, T. Krüssel, R. Vallant, N. Enzinger: *Electron beam welding of a TMCP steel with 700 MPa yield strength*, Welding in the World. Vol. 56, pp. 85–94, 2012. https://doi.org/10.1007/BF03321384.
[197] A. Ferro, P. Tiziani, Metallurgical and mechanical characterization of electron beam welded DP600 steel joints, J. Mater. Sci. 47 (2012) 199–207.
[198] M. Jiang, Y. B. Chen, X. Chen, W. Tao, T. Debroy: *Enhanced Penetration Depth during Reduced Pressure Keyhole-Mode Laser Welding*, Welding Journal. Vol. 90, pp. 110–123, 2020. https://doi.org/10.29391/2020.99.011.
[199] C. Wiednig, N. Enzinger: *Toughness evaluation of EB welds*, Welding in the World, Vol. 61, pp. 463–471, 2017. https://doi.org/10.1007/s40194-017-0422-4.
[200] T. Schaupp, W. Ernst, H. Spindler, T. Kannengiesser: *Hydrogen-assisted cracking of GMA welded 960 MPa grade high-strength steels*, International Journal of Hydrogen Energy, Vol. 45, pp. 20080–20093, 2020. https://doi.org/10.1016/j.ijhydene.2020.05.077.
[201] L. C. William: *Understanding Charpy V-Notch testing*, Welding Journal. Vol. 97, pp. 46–50, 2018.
[202] ASTM E647-11e1: *Standard Test Method for Measurement of Fatigue Crack Growth Rate*, ASTM International 2011.

DOI: 10.14750/ME.2021.051

LIST OF PUBLICATIONS RELATED TO THE TOPIC OF THE RESEARCH FIELD

IN ENGLISH

(1) R.P.S. Sisodia, M. Gáspár: *Experimental assessment of microstructure and mechanical properties of electron beam welded S960M high strength structural steel*, Manufacturing Letters, https://doi.org/10.1016/j.mfglet.2021.05.004, Q1, IF=3.53

(2) R.P.S. Sisodia, M. Gáspár, M. Sepsi, V. Mertinger*: Comparative evaluation of residual stresses in vacuum electron beam welded high strength steel S960QL and S960M butt joints*, Vacuum, Vol. 184, 109931, 2021. https://doi.org/10.1016/j.vacuum.2020.109931, Q1, IF=2.906

(3) R.P.S. Sisodia, M. Gáspár, L. Draskóczi: *Effect of post-weld heat treatment on microstructure and mechanical properties of DP800 and DP1200 high-strength steel butt-welded joints using diode laser beam welding*, Welding in the World,Vol. 64, pp. 671–681, 2020. https://doi.org/10.1007/s40194-020-00867-6, Q1, IF=1.589

(4) R.P.S. Sisodia, M. Gáspár: *Investigation of Metallurgical and Mechanical Properties of Laser Beam Welded and Post-weld Heat Treated DP1400 Steel*, Journal of Materials Engineering and Performance, Vol. 30, pp. 1703–1710, 2021. https://doi.org/10.1007/s11665-021-05469-x, Q2, IF=1.652

(5) R.P.S. Sisodia, M. Gáspár: *Physical Simulation-Based Characterization of HAZ Properties in Steels. Part 1. High-Strength Steels and Their Hardness Profiling*, Strength of Materials, Vol. 51, pp. 490–499, 2019. https://doi.org/10.1007/s11223-019-00094-5, Q3, IF=0.592

(6) M. Gáspár, R.P.S. Sisodia, Á. Dobosy: *Physical Simulation-Based Characterization of HAZ Properties in Steels. Part 2. Dual-Phase Steels*, Strength of Materials, Vol. 51, pp. 805–815. https://doi.org/10.1007/s11223-019-00128-y, Q3, IF=0.592

(7) M. Gáspár, R. Sisodia*: Improving the HAZ toughness of Q+T high strength steels by post weld heat treatment*, IOP Conference Series: Materials Science and Engineering,Vol. 426, 012012, 2018. https://doi.org/10.1088/1757-899X/426/1/012012

(8) R.P.S. Sisodia, M. Gáspár, B. Fodor, L. Draskóczi: *Simulation and Experimental Based Analysis of the Laser Beam Welding of DP Steels*, Advanced Materials Research, Vol. 1157, pp. 73–82, 2020. https://doi.org/10.4028/www.scientific.net/amr.1157.73., Q4

(9) R.P.S. Sisodia, M. Gáspár: *Electron beam welding of S960QL high strength steel - Microstructural evolution & Mechanical properties*, Doc.IV-1460-20, IIW Annual assembly online meeting, C-IV Commission "Power Beam Processes", 15th July 2020.

DOI: 10.14750/ME.2021.051

(10) R.P.S. Sisodia, M. Gáspár, N. Guellouh: *HAZ Characterization of Automotive DP Steels by Physical Simulation*, International Journal of Engineering and Management Sciences, Vol. 4, pp. 478–487 2019. https://doi.org/10.21791/ijems.2019.1.59.

(11) R.P.S. Sisodia, M. Gáspár: *Investigation of electron beam welding of AHSS by physical and numerical simulation*, in: MultiScience-XXXIII. MicroCAD International Multidisciplinary Scientific Conference, University of Miskolc, Miskolc, pp. 23–24, 2019. https://doi.org/10.26649/musci.2019.051.

(12) R.P.S. Sisodia, N. Berrah: *Analysing HAZ softening of quenched and tempered steel by physical simulation*, 7-8 April 2016, Inter Talent UNIDEB Conference, University of Debrecen, Hungary.

(13) M. Gáspár, R. P. S. Sisodia: *Weldability analysis of Q+T and TMCP high strength steels by physical simulation*, Proceedings of the 70th IIW Annual Assembly and International Conference, Pages B166-B170, Shanghai, China, June 29-30, 2017.

(14) N. Guellouh, R.P.S. Sisodia, Z. Szamosi: *The weldability of high strength steels*, MultiScience-XXXII. microCAD International Multidisciplinary Scientific Conference, Miskolc, Hungary 5-6 September 2018, ISBN: 978-963-358-162-9.

(15) R. P. S. Sisodia, M. Gáspár*: Innovative and efficient production of welded body parts from 6082-T6 aluminium alloy*, Proceedings of the 1st International Conference on Engineering Solutions for Sustainable Development (ICESSD), 3-4 October 2019, Miskolc, Hungary. © 2020 Taylor & Francis Group, London, ISBN 978-0-367-42425-1, https://doi.org/10.1201/9780367824037-41.

(16) R.P.S. Sisodia, Judit Kovács: *Comparative HAZ softening analysis of three different automotive aluminium alloys by physical simulation*, IIW Conference, 7-12 July 2019, Bratislava, Slovakia.

(17) M. Gáspár, R.P.S. Sisodia, J. Kovács, G. Németh: *New possibilities for compensating the HAZ softening of the 7075-T6 aluminium alloy*, IIW Conference, 7-12 July 2019, Bratislava, Slovakia.

(18) R.P.S. Sisodia, M. Gáspár, W. Gacem: *Investigation of HAZ softening of AA6082-T6 automotive aluminium alloy by physical simulation*, MultiScience-XXXII. microCAD International Multidisciplinary Scientific Conference, Miskolc, Hungary 5-6 September 2018, ISBN: 978-963-358-162-9.

IN HUNGARIAN

(19) J. Kovács, R.P.S. Sisodia, M. Gáspár: *Hőhatásövezeti zónák fizikai szimulációja nagyszilárdságú szerkezeti acélok esetén/Physical simulation of heat affected zones in the case of high-strength structural steels*, Multidiszciplináris tudományok, Vol. 9 (4), pp. 152-166, 2019. https://doi.org/10.35925/j.multi.2019.4.13.

(20) M. Gáspár, R.P.S. Sisodia, Á. Dobosy, A. Németh: *Csőtávvezetékekben alkalmazott acélminőségek hegesztésekor kialakuló hőhatásövezet tulajdonságainak elemzése fizikai szimulációval/Analysis of heat affected zone properties during welding of steel grades used in pipelines by physical simulation*, Hegesztéstechnika, Tudományos Publikációk, Vol. 31 (1), pp. 83-91. 2020.

DOI: 10.14750/ME.2021.051

(21) J. Kovács, G. Németh, R. Sisodia, M. Gáspár, P. Jámbor: *Hőhatásövezeti tulajdonságok fizikai szimulációra alapozott vizsgálata 7075-T6 autóipari alumíniumötvözet esetén/ Investigation of heat affected zone properties based on physical simulation for 7075-t6 automotive aluminum alloy*, Hegesztéstechnika, Vol. 30 (1), pp. 47-52, 2019.

(22) G. Németh, J. Kovács, R. Sisodia, M. Gáspár, P. Jámbor: *Hőhatásövezeti tulajdonságok fizikai szimulációra alapozott vizsgálata különböző szilárdságú autóipari alumínium ötvözetek esetén/Physical simulation-based investigation of the HAZ characteristics of different strength automotive aluminium alloys*, Hegesztéstechnika, Vol. 30 (2), pp. 41-48. 2019.

(23) M. Gáspár, A. Balogh, G. Bodorkós, Á. Dobosy, A. Németh, R.P.S. Sisodia, I. Török: *Kutatási eredmények a nagyszilárdságú acélok és alumíniumötvözetek hegesztése területén/Research results in the welding of high strength steels and aluminium alloys*, GÉP, Vol. 71 (5-6), pp. 59-66, 2020.

(24) V. Gál, M. Gáspár, J. Kovács, Z. Lukács, R. Sisodia: *Anyagtechnológiai kutatások az Innovatív Anyagtechnológiák Tudományos Műhelyben/Research on materials technologies within the Innovative Materials Technologies Scientific Workshop,* Multidiszciplináris tudományok, Vol. 11. (2), pp. 80-86. 2021. https://doi.org/10.35925/j.multi.2021.2.11

(25) M. Gáspár, R.P.S. Sisodia, I. Timcsák: *Összehasonlító elemzés az elektronsugaras és a huzalelektródás védőgázos ívhegesztés alkalmazásáról nemesített nagyszilárdságú acéloknál/Comparative study about the electron beam and gas metal arc welding of quenched and tempered high strength steels, Proceedings of the XXX. Jubilee International Welding Conference,* pp. 53-58, 2021. ISBN 9786156260000

(26) R.P.S. Sisodia, M. Gáspár, J. Lukács: *Nagyszilárdságú acélok elektronsugaras hegesztett kötéseinek fáradásos repedés terjedéssel szembeni ellenállása*/*Fatigue crack growth resistance of electron beam welded joints from high strength steels*, Multidiszciplináris tudományok, Vol. 11 (4), pp. 318-325, 2021. https://doi.org/10.35925/j.multi.2021.4.36.

Posters

(27) Á. Dobosy, M. Gáspár, R.P.S. Sisodia: *Hegesztési folyamatok végeselemes modellezése/Finite element modelling of welding processes,* 70 éves a Miskolci Egyetem Gépészmérnöki és Informatikai Kara - Kari Jubileumi Emlékülés, Anyagszerkezettani és Anyagtechnológiai Szekció, Poszter előadás, 2019.10.18.

(28) R.P.S. Sisodia, M. Gáspár: *HAZ characterization of high strength steel welded joints by physical simulation*, 70 éves a Miskolci Egyetem Gépészmérnöki és Informatikai Kara - Kari Jubileumi Emlékülés, Anyagszerkezettani és Anyagtechnológiai Szekció, Poszter előadás,2019.10.18.

DOI: 10.14750/ME.2021.051

APPENDICES

DOI: 10.14750/ME.2021.051

[A1]
DP steels without filler material; LBW & PWHT; Tensile test results

LBW and PWHT, Tensile tests						
Specimen No	**Process**	**Laser Power**	**Speed**	**Force**	**Tensile strength**	**Fracture location**
		W	**mm/s**	**N**	**MPa**	
DP800						
5F1	LBW	1000	8	10133	780	weld
5F2	LBW	1000	8	10386	793	weld
5FP1	PWHT	275	4	8774	768	weld
5FP2	PWHT	275	4	9011	788	weld
DP1000						
1F1	LBW	1000	8	9963	820	HAZ
1F2	LBW	1000	8	9730	825	HAZ
1FP1	PWHT	275	4	8817	705	weld
1FP2	PWHT	275	4	8677	714	weld
DP1200						
3F1	LBW	1000	8	8525	772	weld
3F2	LBW	1000	8	8885	812	weld
3FP1	PWHT	275	4	8622	796	weld
3FP2	PWHT	275	4	8472	785	weld
DP1400						
2F1	LBW	1000	8	8784	725	weld
2F2	LBW	1000	8	8839	729	weld
2FP1	PWHT	275	4	8399	675	weld
2FP2	PWHT	275	4	8234	679	weld

DP1000; LBW; PWHT with filler material; Tensile test result

LBW and PWHT with filler material, Tensile tests							
Specimen No	**Process**	**Laser power**	**Welding speed**	**Wire feed rate**	**Force**	**Tensile strength**	**Fracture location**
	-	**W**	**mm/s**	**mm/s**	**N**	**MPa**	**-**
DP1000							
5L3	LBW	2500	20	13	9338	1324	HAZ
5L4	LBW	2500	20	13	9604	1592	HAZ
5P1	PWHT	2500	20	13	8477	1125	HAZ
5P2	PWHT	2500	20	13	8438	1183	HAZ

DOI: 10.14750/ME.2021.051

[A2]
Fractographs; Macrophoto & SEM
Base Material: S960QL; (a) BM (zone I, zone II & zone III), (b) FZ & (c) HAZ
Equipment: Zeiss Evo MA10 Scanning Electron Microscope

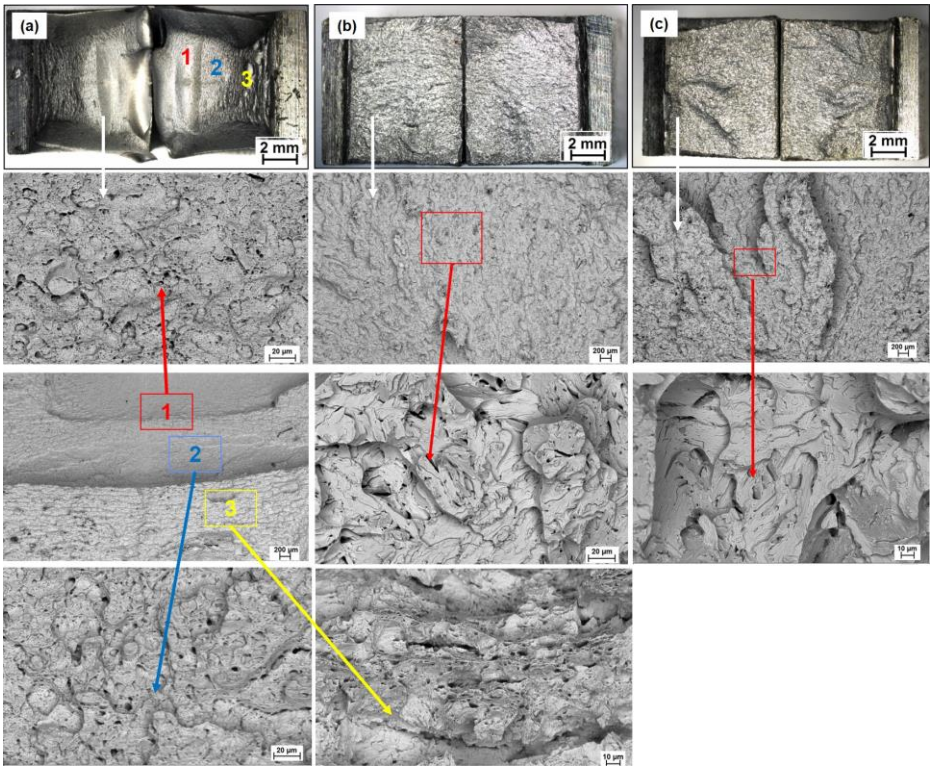

Base Material: S960M; (a) BM, (b) FZ & (c) HAZ (zone I, zone II & zone III)

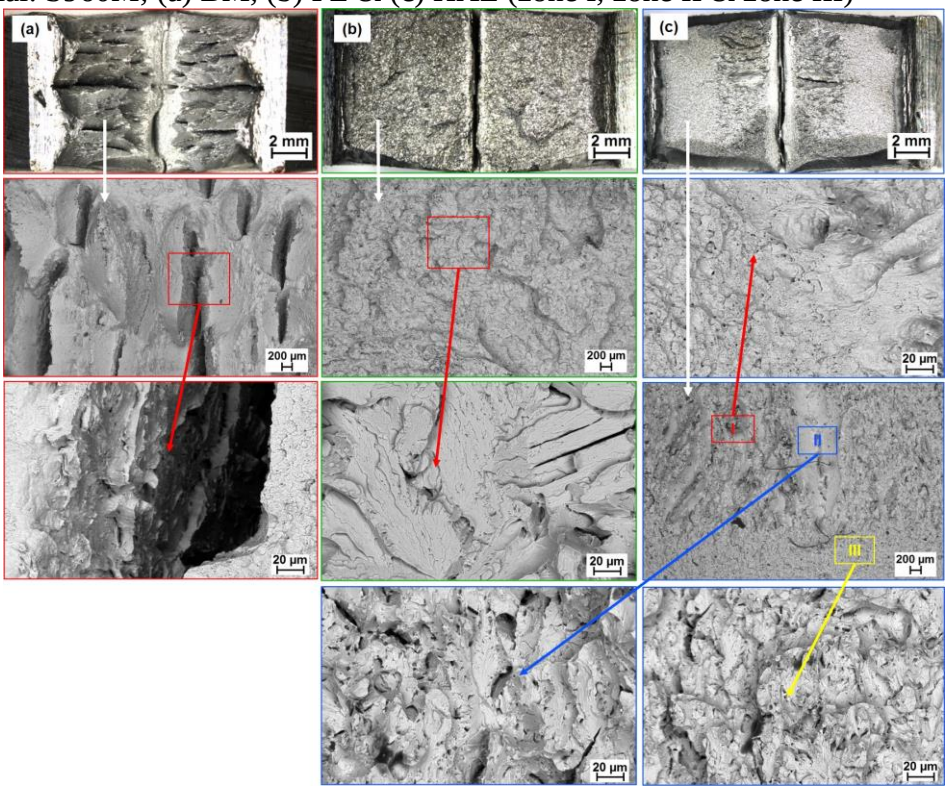

DOI: 10.14750/ME.2021.051

[A3]
EBW; Instrumented Charpy V-notch Table; S960QL: BM, HAZ, FZ

Zone	Measured Charpy V-notch impact test values of EB welded S960QL joints							
	S. No.	F_{max}, kN	CVN, J	CVN_{avg} (J)	CVN_{SD} (J)	W_i; J, (%)	W_p; J, (%)	e (mm)
BM	1	29	206	162	46	41 (20)	165 (80)	2.01
	2	29	135			36 (27)	99 (73)	1.33
	3	28	85			17 (20)	68 (80)	0.83
	4	32	184			39 (21)	145 (79)	0.84
	5	30	199			38 (19)	161 (81)	1.29
HAZ	1	34	43	45	11	35 (82)	8 (18)	0.11
	2	31	39			34 (88)	5 (12)	0.31
	3	29	27			25 (94)	2 (6)	0.3
	4	33	57			50 (88)	7 (12)	0.39
	5	33	57			48 (85)	9 (15)	0.45
FZ	1	34	64	44	20	61 (96)	3 (4)	0.55
	2	31	20			17 (87)	3 (13)	0.07
	3	34	55			41 (74)	14 (26)	0.32
	4	32	62			37 (59)	25 (41)	0.43
	5	28	20			17 (83)	3 (17)	0.18

GMAW; Charpy V-notch impact test results Table; S960QL: HAZ, FZ

Zone	Charpy V-notch impact test results on GMAW joints and simulated HAZ					
	$t_{8/5}$, s	F_{max}, kN	CVN, J	W_i; J, (%)	W_p; J, (%)	Source
CGHAZ	5	31	31	28 (90)	3 (10)	[14]
	30	32	45	39 (87)	6 (13)	[14]
ICHAZ	5	28	29	24 (84)	5 (16)	[14]
	30	28	23	18 (79)	5 (21)	[14]
HAZ	5-10	-	44	-	-	[62]
HAZ	20-30	-	26	-	-	[62]
FZ	5-10	-	43	-	-	[62]
FZ	5-10	30	53	38 (72)	15 (28)	[14]
FZ	20-30	-	38	-	-	[62]

DOI: 10.14750/ME.2021.051

EBW; Instrumented Charpy V-notch Table; S960M: BM, HAZ, FZ

Zone	Measured Charpy V-notch impact test values of EB welded S960M joints							
	S. No.	**F_{max}, kN**	**CVN, J**	**CVN_{avg} (J)**	**CVN_{SD} (J)**	**W_i; J, (%)**	**W_p; J, (%)**	**e (mm)**
BM	**1**	27	139	142	22	36 (26)	103 (74)	1.28
	2	30	183			46 (25)	137 (75)	1.63
	3	28	132			37 (28)	95 (72)	1.20
	4	28	141			42 (30)	99 (70)	1.47
	5	29	117			35 (30)	82 (70)	1.15
HAZ	**1**	34	199	125	64	90 (45)	109 (55)	1.65
	2	31	76			46 (60)	30 (40)	0.67
	3	33	207			64 (31)	143 (69)	1.79
	4	34	91			78 (86)	13 (14)	0.76
	5	31	54			44 (82)	10 (18)	0.60
FZ	**1**	31	92	78	21	46 (50)	46 (50)	0.74
	2	34	98			69 (70)	29 (30)	0.66
	3	34	91			68 (75)	23 (25)	0.79
	4	31	63			54 (85)	9 (15)	0.47
	5	34	44			36 (82)	8 (18)	0.30

DOI: 10.14750/ME.2021.051

[A4]
Fatigue crack growth test: Fractured samples
Base material: S960QL (Top left and Top right) & S960M (Bottom left and right)
Type: Autogenous EB welded joint